Nonlinear Shell Finite Elements for Ultimate Strength and Collapse Analysis of Ship Structures

A thesis submitted in partial fulfillment of the
requirements for the degree of Doktor Ingeniør
by

Abuu Khalifa Mohammed

Trondheim, September 2001

Department of Marine Structures
Faculty of Marine Technology
Norwegian University of Science and Technology

URN:NBN:no-1282

Abstract

The present thesis deals with ultimate strength and collapse analysis of ship structures. Within this area, the attention is directed towards simple and efficient nonlinear finite element models for stiffened plate panels in ship structures. Several types of Morley elements are investigated and two are selected for further development. These triangular elements assume constant stress distribution over the element area.

The first element considered is a nonlinear facet shell element which is valid within moderate rotations. Its elastic formulation has been proposed earlier. In this work, the element matrices are extended to account for material plasticity. The second element, is a displacement–based curved element which undergoes arbitrary large displacements and rotations. The discrete equilibrium equations for this element are re–derived so as to make them more efficient with standard Newton–Raphson solution procedures.

Material plasticity formulation using through–the thickness integration as well as resultants plasticity is presented. The evolution laws are derived from the natural laws of thermodynamics, and a return mapping algorithm with a backward Euler difference scheme is used for the solution of the evolution equations. The plasticity computations involve a solution of a single scalar yield surface for the plasticity multiplier. By performing the matrix algebra analytically, simple and explicit expressions are derived. These equations reduce the computational costs remarkably.

Numerical examples, mostly selected from well–known benchmark problems, are presented to demonstrate the performance of the proposed formulations. Very good agreement is obtained when compared with published results. In addition, typical problems for ultimate strength and collapse analysis of ship hull–girder are analyzed. These include plate girders, stiffened plate panels, as well as a cruciform element. The results show good agreement not only with those obtained from commercial finite element programs, but also from the experimental observations. For stiffened plate panels, comparison is made with DNV design rules, which is found to give non–conservative estimates for some loading conditions.

Finally, a study on multi–span stiffened panels is performed so as to compare the estimates provided by the conventional single span model. It is observed that the conventional model provides conservative estimates, and the effect of transverse frames is especially significant in the finite element model of stiffened panels.

URN:NBN:no-1282

URN:NBN:no-1282

Acknowledgements

This study has been made possible by support from the Norwegian Research Council. The work has been performed under the main supervision of Professor Jørgen Amdahl to whom I would like to express my deepest gratitude. His timely guidance and discussions have been so much inspiring. My sincere thanks goes also to Professor Bjørn Skallerud from the Department of Applied Mechanics as being my co–supervisor. His continuous support and discussions in the field of computational mechanics have been very helpful and encouraging.

Professor L.S.D. Morley, from Brunel University, has been helpful to answer my questions and introducing me to Dr. E.D. Providas, of the University of Thessaly, from whom I got very good help during the elastic implementation of their element. In the same way, I was provided with very helpful information by Professor M.A. Crisfield from the Imperial College, London. I would like to thank them all.

I would also like to thank Dr. Øyvind Hellan of MARINTEK for being an initial co–supervisor of the present work. He was, indeed, involved in establishing the scope of this thesis. I am also grateful to Dr. Tore Holmås of MARINTEK and Dr. Bjørn Haugen of FEDEM for their support during finite element implementation as well as providing me with library tools.

My heartfelt gratitude goes also to colleagues and entire staff at the departments of Marine Structures, Marine Hydrodynamics, and MARINTEK for their friendship. They have provided a very good working atmosphere, and made my research time look so short. My special thanks to Dr. Koci Kotoh who was such a helpful person during his time at the department of Marine Structures. I thank Eiric Byklum for reading the manuscript, and Chunhua Ge for proof reading some of my papers. The computer administrators have done a great job and responded quickly whenever they were needed. My salutes to them.

Last but not least, I would like to extend my thanks to my family. I start with my wife Aysha who has been so kind and understanding to take good care of our sons Adbulsamad, Luqman and Nouman. Her support during my research work had no limits. Caring, love and support from my mother, Dhahira (may her soul rest in eternal peace) will always be remembered. I thank my father, brothers and sisters for their love during all the time that I have been away from them.

URN:NBN:no-1282

URN:NBN:no-1282

Nomenclature

All symbols are defined when they first appear in the text. If deemed necessary, the following list of the most common used notations can be considered as a guide.

Constants and Variables

a_i	constants defined by x–coordinates of the triangle vertexes
$a_{\alpha\beta}$	first fundamental tensor
b_i	constants defined by y–coordinates of the triangle vertexes
c	constant (0.5 or 2)
f	yield function (for Chapter 6 it is a scaling factor)
$h^{\alpha}_{\alpha'}$	transformation terms for practical components
l_i	length of element side i
l_{jk}	dependent quantities of l_i
n^i	Cartesian components of the unit normal $\bar{\boldsymbol{k}}$
n_d	number of free degrees of freedom
t	thickness
u	membrane displacement function
u_i	membrane displacement u at vertex i
v	membrane displacement function
v_i	membrane displacement v at vertex i
w	out–of–plane displacement function
w_i	out–of–plane displacement at vertex i
x	variable along the x–axis in Cartesian coordinates
x_i	x–coordinate at vertex i (Except for Section 2.6)
y	variable along the y–axis in Cartesian coordinates
y_i	y–coordinate at vertex i (Except for Section 2.6)
z	variable along the z–axis in Cartesian coordinates
z_i	z–coordinate at vertex i (Except for Section 2.6)

A	area
A_i	area of sub triangle i
C_0	initial element configuration

URN:NBN:no-1282

C_n	current element configuration
E	Young's modulus
E_{ij}	components of the Green–Lagrange strain tensor
F_{ij}	components in the matrix of material deformation gradient
H	isotropic hardening modulus
J	Jacobian
$M^{\alpha\beta}$	covariant components of $\boldsymbol{M}$
$M_{\alpha\beta}$	components of $\boldsymbol{M}$
$N^{\alpha\beta}$	covariant components of $\boldsymbol{N}$
$N_{\alpha\beta}$	components of $\boldsymbol{N}$
R_{ij}	components of the rotation tensor $\boldsymbol{R}$
S_{kl}	components of the second Piola–Kirchhoff stress tensor
$\bar{T}_{ij}$	components of matrix $\bar{\boldsymbol{T}}$
W^i	internal work
α	material plasticity constant
$\bar{\alpha}$	material plasticity constant
β	material plasticity constant
$\bar{\beta}$	material plasticity constant
$\chi_{\alpha\beta}$	components of $\boldsymbol{\chi}$
δ_{ij}	Kronecker delta
δ_{mech}	mechanical (material) dissipation
$\gamma_{\alpha\beta}$	components of $\boldsymbol{\gamma}$
$\bar{\gamma}_i$	normal membrane strain corresponding to side i
$\kappa_{\alpha\beta}$	components of covariant curvature tensor
λ	plasticity multiplier (or consistency parameter)
ν	Poisson's ratio
ω_k	constants
Ω	Helmholtz's free energy function
ψ_{i+3}	measure of deflections of the mid–side nodes
ρ	mass density
σ	subsequent yield stress
$\sigma_\circ$	yield stress
σ_u	ultimate stress
σ_{kl}	components of the stress tensor $\boldsymbol{\sigma}$
θ_i	mid–side rotation at node number $i+3$
ε^p	scalar variable representing isotropic hardening
$\varepsilon^{\alpha\beta}$	contravariant permutation tensor
$\varepsilon_{\alpha\beta}$	components of covariant membrane strain tensor
ξ^i	area or triangular coordinates
ζ	intensity of external loads
$\delta\zeta$	the current correction of applied loads intensity
$\Delta\zeta$	the current increment of applied loads intensity
$\square_{,\alpha}$	partial derivative with respect to the area coordinate ξ^α

URN:NBN:no-1282

Vectors and Matrices

$\boldsymbol{a}$	displacement vector without rotational DOF
$\boldsymbol{b}$	body forces
$\boldsymbol{c}_i$	matrices defined by Equation (4.28)
$\boldsymbol{d}_i$	vectors of triangular constants defined in Equation (4.27)
$\boldsymbol{e}$	strain (resultants) vector
$\boldsymbol{e}_i$	unit vector along the Cartesian axis
$\boldsymbol{f}$	internal force vector
$\boldsymbol{g}_\alpha$	natural base vectors
$\bar{\boldsymbol{k}}$	unit normal to the undeformed surface
$\boldsymbol{n}$	vector of n^i
$\hat{\boldsymbol{n}}$	plastic flow direction
$\bar{\hat{\boldsymbol{n}}}_i$	scalar components of vector $\bar{\hat{\boldsymbol{n}}}$ in Equation (5.98)
$\boldsymbol{p}$	the current accumulation of applied loads
$\bar{\boldsymbol{p}}$	constant vector of the actual applied loads
$\hat{\boldsymbol{p}}$	position vector
$\boldsymbol{r}$	element displacement vector (DOF)
$\boldsymbol{s}$	stress resultants vector
$\boldsymbol{s}_i$	vector in the direction of side i
$\boldsymbol{t}_i$	initial unit vectors to the element flat surface
$\boldsymbol{t}_i^n$	current unit vectors to the element flat surface
$\boldsymbol{u}$	membrane displacement vector
$\boldsymbol{v}$	membrane displacement vector
$\boldsymbol{w}$	out–of–plane displacement vector
$\bar{\boldsymbol{w}}$	incremental velocity vector
$\bar{\boldsymbol{w}}_\circ$	initial incremental velocity vector of step $n+1$
$\bar{\boldsymbol{w}}_p$	current incremental velocity vector due to applied loads
$\bar{\boldsymbol{w}}_r$	current incremental velocity vector due to unbalanced forces
$\delta\boldsymbol{r}$	the current correction of displacement vector
$\Delta\boldsymbol{r}$	the current increment of displacement vector

$\boldsymbol{A}$	6×6 constant matrix
$\boldsymbol{B}$	the complete 12×12 nonlinear strain–displacement matrix
$\boldsymbol{B}_\psi$	strain–deflection matrix
$\boldsymbol{B}_a$	the sum of $\boldsymbol{B}_{a1}$ and $\boldsymbol{B}_{a2}$
$\boldsymbol{B}_k$	strain–curvature matrix
$\boldsymbol{B}_u$	strain–displacement matrix
$\boldsymbol{B}_w$	strain–deflection matrix
$\boldsymbol{B}_{G\psi}$	geometric stiffness from $\boldsymbol{\psi}$
$\boldsymbol{B}_{Ga}$	geometric stiffness from $\boldsymbol{a}$
$\boldsymbol{B}_{Gk}$	geometric stiffness from $\boldsymbol{\kappa}$
$\boldsymbol{B}_{Gw}$	geometric stiffness from $\boldsymbol{w}$

URN:NBN:no-1282

$\boldsymbol{B}_{\bar{\psi}}$	the sum of $\boldsymbol{B}_{\psi_\circ}$ and $\boldsymbol{B}_{\psi_d}$
$\boldsymbol{B}_{\bar{w}}$	rotated $\boldsymbol{B}_w$ matrix with respect to R_{3i}
$\boldsymbol{B}_{\psi_\circ}$	strain–initial curvature matrix
$\boldsymbol{B}_{\psi_d}$	strain–deformational curvature matrix
$\boldsymbol{B}_{a1}$	linear strain–displacement matrix
$\boldsymbol{B}_{a2}$	nonlinear strain–displacement matrix
$\boldsymbol{C}$	membrane rigidity matrix
$\boldsymbol{D}$	bending rigidity matrix
$\boldsymbol{E}_{\varphi}$	deflection–rotation matrix
$\boldsymbol{E}_{w}$	deflection–displacement matrix
$\boldsymbol{E}_{\bar{w}}$	rotated $\boldsymbol{E}_w$ matrix with respect to R_{3i}
$\boldsymbol{H}$	material transformation matrix
$\boldsymbol{K}$	secant stiffness matrix
$\boldsymbol{K}_t$	tangent stiffness matrix
$\boldsymbol{M}$	moments
$\boldsymbol{N}$	membrane forces
$\boldsymbol{P}$	3×3 constant matrix
$\boldsymbol{T}$	element transformation matrix
$\bar{\boldsymbol{T}}$	strain transformation matrix
$\boldsymbol{X}$	membrane–bending coupling rigidity matrix

$\mathbb{A}_{ij}$	scalar components of matrix $\mathbb{A}$ in Equations (5.79) and (5.81–5.82)
$\hat{\mathbb{A}}_{ij}$	scalar components of matrix $\hat{\mathbb{A}}$ in Equations (5.86–5.88)
$\mathbb{C}$	elasticity modular matrix
$\mathbb{C}'$	elasticity modular matrix
$\mathbb{C}_t$	consistent elasto–plastic tangent modular matrix
$\bar{\mathbb{C}}$	elasticity resultant modular matrix
$\bar{\mathbb{C}}_{ij}$	scalar components of matrix $\bar{\mathbb{C}}$ in Equation (5.69)
$\mathbb{H}$	material compliance matrix
$\bar{\mathbb{H}}_{ij}$	scalar components of matrix $\bar{\mathbb{H}}$ similar to Equation (5.38) but for resultants plasticity
$\mathbb{P}_{ij}$	scalar components of matrix $\mathbb{P}$ in Equation (5.51)
$\hat{\mathbb{P}}_{ij}$	scalar components of matrix $\hat{\mathbb{P}}$ in Equation (5.54)
$\mathbb{Q}$	matrix of eigenvectors of the product matrix $\mathbb{C}\boldsymbol{P}$
$\bar{\mathbb{Q}}$	matrix of eigenvectors of the product matrix $\bar{\mathbb{C}}\boldsymbol{A}$
$\mathbb{R}_i$	scalar components of vector $\mathbb{R}$ defined in Equations (5.96–5.96)
$\mathbb{V}$	matrix relating the correct stresses to the trial elastic stresses
$\bar{\mathbb{V}}_{ij}$	scalar components of matrix $\bar{\mathbb{V}}$ in Equations (5.79–5.80)
$\dot{\square}$	time or time–like derivative
$\square^{(xy)}$	vector in the local xy–coordinates

$\boldsymbol{\chi}$	flexural strain tensor (curvature changes)
$\boldsymbol{\epsilon}$	strain tensor
$\boldsymbol{\epsilon}^e$	elastic strains
$\boldsymbol{\epsilon}^p$	plastic strains

URN:NBN:no-1282

$\bar{\boldsymbol{\epsilon}}$	strain resultant tensor
$\dot{\boldsymbol{\epsilon}}$	strain rate
$\boldsymbol{\gamma}$	membrane strain tensor
$\bar{\boldsymbol{\gamma}}^{av}$	average membrane strains along element sides
$\boldsymbol{\kappa}$	covariant curvature tensor
$\boldsymbol{\psi}$	vector of ψ_{i+3}
$\boldsymbol{\rho}$	residual force vector
$\boldsymbol{\sigma}$	stress tensor
$\bar{\boldsymbol{\sigma}}$	stress resultant tensor
$\boldsymbol{\varepsilon}$	covariant membrane strain tensor
$\boldsymbol{\varphi}$	mid–side rotation vector
$\boldsymbol{\Lambda}$	diagonal matrix of eigenvalues of the product matrix $\mathbb{C}\boldsymbol{P}$
$\bar{\boldsymbol{\Lambda}}$	diagonal matrix of eigenvalues of the product matrix $\bar{\mathbb{C}}\boldsymbol{A}$

Abbreviations

ABAQUS	computer program as elaborated in the reference list
CR	co–rotational description
DOF	degree of freedom
DNV	Det Norske Veritas
NINT	number of integration points through–the thickness
NSHEL	computer program as elaborated in the reference list
TL	total Lagrangian description
UL	updated Lagrangian description
VCCL	very large crude oil carrier

URN:NBN:no-1282

URN:NBN:no-1282

Contents

URN:NBN:no-1282

URN:NBN:no-1282

URN:NBN:no-1282

URN:NBN:no-1282

List of Figures

URN:NBN:no-1282

URN:NBN:no-1282

URN:NBN:no-1282

URN:NBN:no-1282

List of Tables

URN:NBN:no-1282

Chapter 1

Introduction

In structural design of ships and offshore structures, the ultimate capacity of the individual components of the system is usually not to be exceeded under normal conditions. However, an overload on a single or a group of components does not necessarily mean a complete structural failure. Due to static indeterminacy, there exists strength reserves by which the structure can sustain more load before a complete failure.

The maximum load at which the structure can not sustain any more loading is called the *ultimate strength*. If the load effects are beyond this margin, the structure is considered not fit for service. The most important situation where the reserve strength needs to be evaluated is during accidental conditions — such as ship grounding and collision, explosions and fire — and extreme environmental loads.

In conjunction with accidental loads, analysis is carried out beyond the ultimate strength by considering progressive collapse of the structure. In this range, load redistribution between the system components and the behaviour in the post–collapse range can be studied. Of particular importance in the post–collapse range is the *energy dissipation* capability of the system and its components. This is given by the area under the load–displacement curve.

The present thesis deals with ultimate strength and collapse analysis of ship structures. Within this area, the attention is mainly directed towards simple and efficient finite element methods for stiffened plate panels in ship structures. Though the discussions are made with reference to ship structures, the ideas are applicable to other (offshore and civil engineering) structures composed of similar components as well.

Generally, the overall dimensions of the ship structure make a boxed shape. This box is commonly known as the ship hull–girder and it is composed of various stiffened panels as illustrated in Figure 1.1. The individual panels consist of main plating, longitudinal stiffeners, and transverse frames. The main function of the transverse frames is to resist the loads induced by the hydrostatic and dynamic forces on the bottom and side shells.

URN:NBN:no-1282

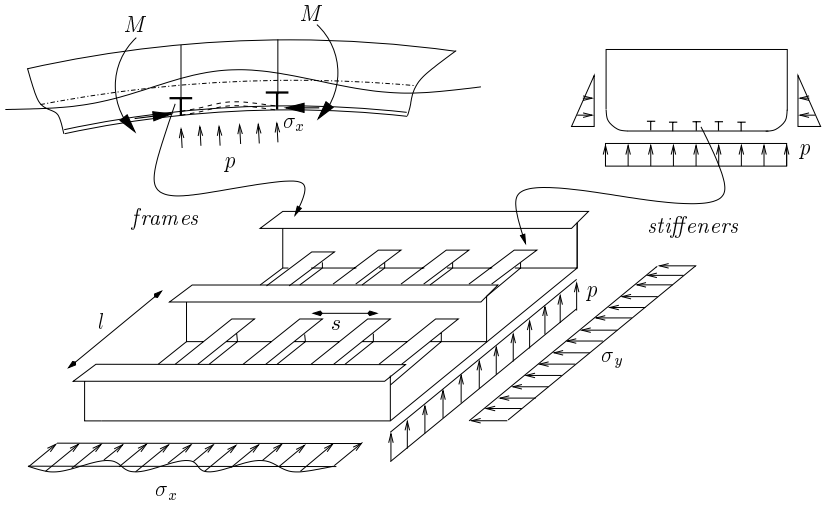

Figure 1.1 The ship hull girder.

The transverse frames of the hull–girder are normally heavier and possess higher stiffness than the longitudinal stiffeners. They provide extra longitudinal rigidity by stimulating interframe collapse of the stiffened panels as opposed to an overall collapse. Consequently, the stiffened panels are usually assumed to be well supported by the transverse frames.

The longitudinal strength of the ship hull–girder is one of the fundamental strength of the ship structure. This strength is characterized by the ultimate strength of the stiffened panels. The major loading that utilizes this strength is the longitudinal bending moment produced by distributed hull weight, cargo, and environmental loads.

Stiffened panels are not only the resisting elements in ships and offshore structures, but also are the main components of a wide range of other structures such as bridges and dock gates. Therefore, it is essential to predict accurately the behaviour of these panels in order to produce rational design. Understanding the behaviour of individual panels can be considered as the first step towards understanding the overall behaviour.

1.1 Background and Motivation

Recent and historical events have demonstrated significant hazards due to ship collision and grounding. The consequences of these events are loss of human lives, financial losses, and environmental hazards. The most typical consequence of the latter is the oil spill in the sea. This leads to extended and involving problems related to sea pollution.

URN:NBN:no-1282

Examples of these events include the grounding of the crude oil tanker *Sea Empress* in 1996. This resulted in the discharge of approximately 72000 tons of oil into the seas around the coast of South–West Wales. It is one of the most serious oil pollution incidents in the European history. In 1997, the Russian tanker Nakhodka discharged about 6000 tons of heavy fuel oil into the sea of Japan when it failed to resist a severe storm.

As a result of catastrophic ship accidents owing to collision and grounding, ships with high strength are being demanded. As a first step any oil tanker larger than 5000DWT is required to have a double hull structure. The treaty of MARPOL (1992) established by International Maritime Organization (IMO) requires the double hull space of Very Large Crude oil Carrier (VLCC) to be more than 2 meters. This is mandatory for all new tankers and for all existing tankers beyond the year 2015. Until then, single hull ships will continue to transport oil.

Although the double hull concept is not a perfect solution, it is an effective way of preventing oil spills during grounding and collision. As long as the inner plating remains intact, oil spill will not occur immediately after the accident even though the outer shell plating has been torn or ruptured. This is only true when the ultimate strength capacity is not exceeded.

Under bad maintenance and gross human error, the ultimate strength reduction is very common even under normal conditions. This may also be the case in a damaged condition due to accidental loads. In these situations, the ship hull–girder is more prone and may, at any time, collapse in the form of breakage and be lost completely. This incident is associated with more severe oil spill as compared to oil leaking in a damaged condition. Examples of ship failures in breakage is the *VLCC Energy concentration*, and the tankers *Ryoyo–Maru* and *Nakhodka* (Yao 1999). It is reported by Ohtsubo *et al.* (1999) that the main causes of *Nakhodka* failure were serious corrosion and the separation of main plating from the longitudinal stiffeners.

Classification rules such as DNV (1995) and ABS (1995) require that the damaged ship hull–girder retain a minimum hull–girder residual strength. This should prevent or substantially reduce the risk of losing the damaged ship completely due to post–accidental collapse or disintegration of the hull structure during tow or rescue operation.

1.2 Ship Strength Analysis

Prior the mid–fifties, full scale tests were usually employed to study the ultimate longitudinal strength of the hull girder (Yao 1999). Since then, only parts of ship components have been studied. With the advent computer technology, most of these tests have been replaced by numerical simulations. Generally, the simulations are much cheaper to perform than the complete tests. Indeed, it has been clarified by Lenselink and Thung (1992) that the behaviour in collision could be simulated with sufficient accuracy owing to the great progress in numerical simulation technology.

URN:NBN:no-1282

Generally, research in ship collision and grounding seems to be generic in the sense that assumptions are made for a number of parameters that enter the analysis. Most of the procedures developed for analysis and design employ simple analytical or semi–analytical expressions. Although most of these methods can be used directly, some require computer implementation for efficient evaluation. The most advanced methods are based on nonlinear finite element analysis. Therefore, it is usually considered that simplified methods are those which do not employ finite elements.

Conventional design of stiffened panels is usually based on simple analytical methods. Several Classification societies use the beam–column concept. This approach is illustrated in Figure 1.2 for DNV (1992) design code.

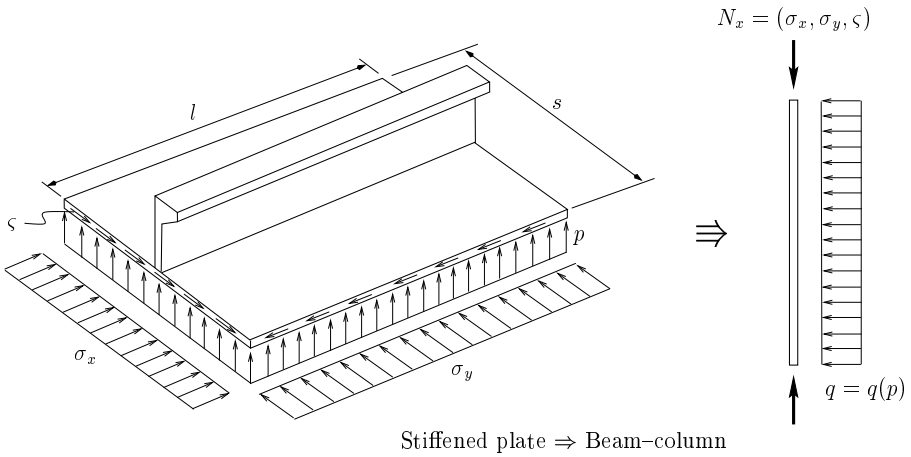

Figure 1.2 Beam–column approach.

Contrary to conventional ultimate strength analysis, system effects should be taken into account during accidental conditions. In other words, local collapse is accepted provided that global integrity is not put into jeopardy. If such effects are to be considered in a nonlinear finite element analysis, *efficient computational algorithms* are required. This is the central part of the present thesis.

The most common failure type of the hull–girder is buckling and plastic collapse of the deck and bottom stiffened plates. This may progress into physical effects such as folding and fracture. The initial buckling is especially important in the sense that it may determine the geometry of subsequent deformations.

Another important phenomenon is plate tearing which is usually associated with ship grounding. It signifies the process whereby sharp objects force a crack to develop and move in a plate with little plastic deformation except in the vicinity of the crack tip. Bending and folding of adjacent material often accompanies this process.

URN:NBN:no-1282

1.3 Scope and Objectives

The objective of the present thesis is to develop efficient nonlinear finite elements formulations for ultimate strength and collapse analysis of stiffened panels. The overall scope may be summarized as follows,

— Investigation and development of a simple nonlinear shell finite element formulation considering arbitrary large displacements and rotations.

— Investigation and development of a simple material plasticity formulation assuming small strains.

— Implementation of the element and material plasticity formulations in a nonlinear finite element computer program.

— Test the formulations using benchmark problems, as well as practical problems which are typical in ultimate strength and crashworthiness.

— Parametric studies on single and multi–span stiffened plate panels subjected to combined compression and lateral pressure.

The intended destination of the proposed formulations is in the nonlinear computer program USFOS (1998). This program was originally developed for progressive collapse analysis of offshore structures based on space–frame representation. With the implementation of nonlinear shell finite elements, refined modelling in areas with large inelastic deformations is made possible, while the rest of the structure can remain as beam elements. In USFOS, the present formulations will provide another alternative to the implementation of Skallerud and Haugen (1999) which is already in place for three and four node facet elements.

Due to technical issues, the task of direct implementation of the present formulations into USFOS (1998) is not tied with the present thesis. One of the main reasons is the difference in the number of degrees of freedom per node between USFOS's beam element and the elements in this thesis.

1.4 Thesis Organization and Contributions

Having introduced the problem in the present chapter, the thesis continues to give a brief overview on the basics of shell finite elements in Chapter 2. Thereafter, two elasto–plastic shell finite elements of Morley type are presented in the following chapters. The first element, which appears in Chapter 3, is based on the von Kàrmàn nonlinear theory. The elastic formulation of this element was derived by Providas (1990) and Morley (1991) and is valid for moderate rotations.

URN:NBN:no-1282

The present investigation finds considerable computational advantage for the element presented in Chapter 3. In this thesis, the element matrices are extended to include material plasticity based on stress resultants. To the authors knowledge, combining resultants plasticity with Morley element is the second attempt after Crisfield and Peng (1992) who reported numerical problems. Here it is shown that the elasto–plastic formulation performs well within the element range of validity. Most of the material in this chapter has appeared in a journal paper by Mohammed *et al.* (2001). A short presentation is also made by Mohammed *et al.* (2000b).

An element which is valid for arbitrary large displacements and rotations is presented in Chapter 4. It constitutes the basics of the displacement–based element proposed by Bout (1993), which resulted in a constant tangent stiffness matrix within an increment. In this chapter, the discrete equilibrium equations are re–derived and a variable tangent stiffness matrix is obtained for an arbitrary increment. The new equilibrium equations converge faster with standard Newton–Raphson solution procedures, and they have been presented by Mohammed *et al.* (2001b).

The material plasticity formulation is presented in Chapter 5. Both, through–the thickness integration and resultant plasticity procedures are described. All formulations involve a solution of a single scalar yield function for the plasticity multiplier. A very comprehensive description of associated plasticity with Huber–von Mises types of yield surfaces is given. The computational time required in matrix operations is reduced by performing them analytically. As a result, very simplified expressions and explicit yield functions are obtained for efficient computations.

In Chapter 6, a nonlinear solution procedure of the equilibrium equations is presented. It is followed by numerical examples to demonstrate the performance of element and material formulations, as well as the implementation. The numerical examples are typical benchmark problems and the results are compared with those from other publications. Difficult benchmark problems are analyzed with very good results. Some of these examples are very complicated and many existing finite elements have not been able to trace their response completely.

Next to benchmark problems, the efficiency of resultants plasticity versus through–the thickness integration is studied. The same is done for the various element formulations in the family of Morley shell elements. The results, in terms of CPU time, are tabulated for different cases of general examples. It is demonstrated that a complete double surface resultants plasticity does not seem to offer significant computational advantages. However, its modified version presented in Chapter 5 shows a computational advantage of about 30–50 percent over through–the thickness integration using 3–5 points.

Examples which are of more practical interest and related directly to ship structures are presented in Chapter 7. They include stiffened panels, plate girders, and a cruciform element. The results compare very well with other finite elements and experimental observations. For stiffened plate panels, it is observed that the beam–column approach used by DNV (1992) gives non–conservative estimates for some loading conditions. Most of the material in this chapter has been presented by Mohammed *et al.* (2001a).

URN:NBN:no-1282

Chapter 8 studies the ultimate strength analysis of multi–span stiffened panels. The aim is to investigate the influence of practical boundary conditions and the rigidity of transverse frames on single span model. It is found that the single span model produces conservative estimates of ultimate strength. The rigidity of transverse frames is found to be significant since it reduces the effective buckling length. The straight edge boundary condition in the longitudinal edges is studied and found to give an upper bound solution. The lower bound is associated with transversely free boundary condition. Chapter 9 summarizes the concluding remarks and recommendation for further work.

URN:NBN:no-1282

URN:NBN:no-1282

Chapter 2

Basics of Shell Finite Elements

2.1 Introduction

The concepts of *finite element method* were developed about fifty years ago with the pioneering works of Argyris (1960) and Turner *et al.* (1956), and the term appears to have first been used by Clough (1960). The ideas were originally developed for use in structural mechanics but they are now applied in other fields as well.

The finite element procedure involves an approximate division or discretization of a structure into several fictitious elements of finite magnitude that represent the physical model. These elements are known as *finite elements* and they exist in several shapes ranging from one to three dimensions with plane or curved edges.

Each finite element is given a name associated with its behaviour. The choice of a finite element model for a specific structure depends on the geometry and the physical behaviour that it is supposed to represent or reproduce. For a detailed discussion on the subject, the reader is referred to the various standard textbooks including Zienkiewicz and Taylor (2000a) and Crisfield (1991).

Shells form a curved surface in space and are in fact three–dimensional solids. However, their dimension in one direction is much smaller than in the other two directions, i.e. they are thin as compared to their spans. Therefore, a shell is geometrically described by its thickness and the shape of its mid–surface. Shells are load carrying structures and display bending stresses and membrane stresses with no possibility on the separation between the two.

The bending stresses in a shell correspond to the bending stresses in a *plate* and produce bending and twisting moments. The *membrane* stresses correspond to the stresses in a plane stress problem and they act tangent to the mid–surface. Plate elements differ from shell elements by having flat surface with no membrane forces.

URN:NBN:no-1282

A complete three–dimensional analysis of shells is not only demanding but often leads to numerical ill–conditioning problems (Zienkiewicz and Taylor 2000b). To simplify the solution, several assumptions regarding shell behaviour have been introduced in the past. The outcome of these assumptions were the mathematical models or approximate theories. Their classical treatments are discussed extensively in the standard texts such as Timoshenko and Woianowsky-Krieger (1959) and Flügge (1960).

The governing differential equations resulting from shell theories are complicated and have not been solved analytically except for cases with simple geometry and boundary conditions. Instead, numerical methods were deviced but since the advent of powerful computer technology, the finite element method have replaced most of these techniques.

In the context of finite element methods, there are mainly three options for modelling shell structures. These can be classified as,

— Curved elements designed from shallow or deep shell theory.

— Curved elements designed from isoparametric concept.

— Flat or facet elements from an assembly of plate and membrane elements.

In the present work, the element formulations are based on the third option. The next (or better) and effective but still simple way of modelling the curved shell element is the shallow shell approach of Marguerre (1938). Even with a facet formulation, however, it will appear in Chapter 3 that the initial curvature can be introduced in the stiffness matrix so as to represent a curved surface.

Under the assumption that the shell is *thin*, it is possible to reduce the shell problem from a three to a two–dimensional one. This procedure follows from the so–called thin or Kirchhoff plate theory. The early version of this theory was presented about 200 years ago by Sophie Germain (Bucciarelli and Dworsky 1980), but the final version is based on assumptions formalized by Kirchhoff (1850). In a slightly different way, Reissner (1945) and Mindlin (1951) introduced the effect of transverse shearing deformations. This modification extended the thin plate theory to the application on *thick* plates. It is commonly known as the Reissner–Mindlin plate theory.

The so–called *Love's first approximation* says that "the strain energy is the sum of extensional and flexural energies" (Koiter 1960). For thin shells, this approximation is usually used along with the Kirchhoff plate theory. The result is the so–called Kirchhoff–Love hypothesis for thin shells. In this thesis, it is assumed that the shell is thin and the formulations are based on the Kirchhoff–Love theory. Therefore, the following two postulates in the order of their importance are respected. Namely,

— Sections normal to the mid–surface of the shell surface remain plane and normal to the mid–surface during deformation and do not change their lengths.

— Direct stresses in the normal direction to the shell mid–surface are small and therefore direct strains in that direction can be neglected.

URN:NBN:no-1282

2.2 Finite Element Approximations

In the design of finite elements, researchers have pursued many ways and there is no universal or unique approach that is commonly accepted. Among the diversities is the choice of the so–called shape functions which is the first and important step in the finite element approximation. Generally, there are four alternatives on which the finite element approximation may be based. Namely,

— Displacement formulation.

— Two–field mixed formulation.

— Three–field mixed formulation.

— Three–field enhanced strain mixed formulation.

The last three options are collectively known as the *mixed* or reducible formulations. The first option is irreducible in the sense that none of the components in the assumed dependent variables can be eliminated while still leaving a well defined problem.

In mixed formulations, the discrete equations may be derived from the variational principles by requiring the stationary of the resulting energy potential. However, direct procedures can also be applied (see e.g. Zienkiewicz and Taylor (2000a)). Within a mixed formulation either the stresses, the strains, or both are approximated independently. For a two–field approximation, the outcome is usually the so–called Hellinger–Reissner variational principle with the stress tensor as a primary variable. On the other hand, the three–field approximation includes also the strain approximations leading to the so–called Hu–Washizu variational principle (Washizu 1982).

An alternative to the three–field approximation, is the *enhanced strain* model. The key idea in this method is the splitting of the strains into the usual displacement gradient term and the added enhanced strain term. More precisely, it is a parameterization of the deformation gradient in terms of the mixed and enhanced deformation gradient from which a consistent formulation is derived.

The formulations in this thesis are based on assumed displacements. In the assumed displacement formulations, only the displacements are used for finite element approximation. Though, all the approaches have their own advantages and disadvantages, the displacement based finite elements appear to be most popular. In some cases, however, like the incompressible elasticity, it may be essential to use the mixed formulation. For rectangular or quadratic elements, the displacement shapes can be conveniently chosen as polynomials defined in Cartesian coordinates. In triangular elements, however, the polynomials in area coordinates are usually the natural choice.

The shape functions play a paramount role in ensuring convergence to the exact solution. The selection of these functions requires several conditions to be satisfied (see e.g. Zienkiewicz and Taylor (2000a)). If the displacement function has discontinuity between elements, it leads to the so–called non–conforming elements. When a non–conforming

URN:NBN:no-1282

finite element has been designed from a suitable choice of shape functions, its condition for convergence can only be sufficiently verified by the so–called patch test. This procedure was proposed by Irons in 1965 (see e.g. Irons and Razzaque (1972), Strang (1972), and Strang and Fix (1973)). The test requires that, for any mesh orientation the element is able to produce the constant strain condition and rigid body motions without self straining.

The patch test is not dealt with in this thesis, simply because the elements to be presented are the assembly of well defined plate and membrane elements for which the patch test has been already verified. See for example the work of Providas (1990).

2.3 Equilibrium Equations

Assuming that the shape function is selected using only the displacements $\bar{\boldsymbol{u}}$ as primary variables, the equilibrium conditions may be established by means of the virtual work principle, such that

$$\int_A \delta\boldsymbol{\epsilon}^T\boldsymbol{\sigma}\ dA = \int_A \delta\bar{\boldsymbol{u}}^T\boldsymbol{b}\ dA + \int_S \delta\bar{\boldsymbol{u}}^T\bar{\boldsymbol{t}}\ dS \tag{2.1}$$

where A is the area, $\boldsymbol{\epsilon}$ are the strains, $\boldsymbol{\sigma}$ are the stresses, $\boldsymbol{b}$ are the body forces, and $\bar{\boldsymbol{t}}$ are the tractions prescribed on the surface S. In this equation, it is assumed that the structure is loaded from a stress free condition. If residual stresses are present, they can added directly to the equilibrium condition. Equation (2.1) simply says that the internal virtual work must balance the corresponding external virtual work.

For each element, the displacements are approximated by,

$$\bar{\boldsymbol{u}} = \sum_i \bar{\boldsymbol{N}}_i\boldsymbol{r}_i = \bar{\boldsymbol{N}}\boldsymbol{r} \tag{2.2}$$

where $\bar{\boldsymbol{N}}_i$ contains the shape functions defined in terms of the independent primary variables, and $\boldsymbol{r}$ is the element displacement (degrees of freedom) vector. The strains are related to the displacements through the matrix operator $\mathcal{L}$ as,

$$\boldsymbol{\epsilon} = \mathcal{L}\bar{\boldsymbol{u}} \tag{2.3}$$

When Equations (2.2) and (2.3) are submitted to (2.1), they provide the residual force as a function of the virtual displacements $\delta\boldsymbol{r}$. Assigning arbitrary values for these displacements, leads to an element equilibrium equation. This can generally be expressed as,

$$\boldsymbol{\rho}(\boldsymbol{r},\zeta) = \boldsymbol{K}\boldsymbol{r} - \boldsymbol{p} = \boldsymbol{f}_{int} - \boldsymbol{f}_{ext} = \boldsymbol{0} \tag{2.4}$$

where $\boldsymbol{K}$ is the secant stiffness matrix, $\boldsymbol{p}$ is the external load vector, and $\boldsymbol{\rho}$ is the residual force vector. The product $\boldsymbol{K}\boldsymbol{r}$ represents the internal force vector. The displacement vector $\boldsymbol{r}$ and the intensity of the applied loads ζ, are denoted as the control parameters.

URN:NBN:no-1282

For linear problems, the secant stiffness matrix is constant and usually symmetric and positive definite. Accordingly, the solution can be achieved by a single load step involving numerical technique such as Gauss elimination or Cholesky decomposition. In nonlinear problems, however, $\boldsymbol{K}$ is a function of the displacements and is in general not symmetric. Consequently, the solution is obtained through a numerical incremental–iterative technique where the so–called *tangent stiffness* is required.

The tangent stiffness matrix is obtained by linearizing the residual or equilibrium Equation (2.4) with respect to the displacements $\boldsymbol{r}$. This matrix is also a function of the displacements but it is usually symmetric. The external load vector $\boldsymbol{p}$ is independent of displacements, only when conservative systems are considered. For non–conservative systems, for example follower loads such as hydrostatic pressure, it is also a function of the displacements. For these cases, the equilibrium equations do not follow from the total potential energy.

2.4 Nonlinearities

For solids, the source of nonlinear behaviour may exist in the form of *material* nonlinearity and *geometric* nonlinearity. The simplest case of nonlinear material behaviour is that of elasticity where the strains are not linearly related to the stresses through the Hooke's law. The more general form is that where the loading and unloading response of the material is different. Material plasticity falls into this category and we shall devote Chapter 5 for its discussion.

When structural displacements become large, it is necessary to include the geometric changes in the equilibrium equations. This phenomenon is known as geometric nonlinearity. It is achieved by introducing the nonlinear terms of the deformation gradients into the strain–displacement relations. Usually, these terms introduce considerable changes in the structural response.

For many applications, geometric nonlinearity goes concurrently with material plasticity. For instance, in offshore plate panels large displacements and buckling may render the typical behavior of the constitutive equations to be nonlinear. This will require the treatment of material nonlinearity. However, in aerospace structures and marine risers, similar states can be reached with the constitutive equations remaining essentially linear.

2.4.1 Geometric Nonlinearity

There are generally three finite element approaches of treating large displacements. These procedures are distinguished by their ways of defining the reference and base configurations from which the strains are measured. A comprehensive review of these methods can be obtained from the work of Mattiasson (1983). The procedures can be grouped as,

URN:NBN:no-1282

— Total Lagrangian description (TL),

— Updated Lagrangian description (UL),

— Co–rotational description (CR).

In the *Total Lagrangian description*, the reference configuration is seldom or never changed. It is often kept equal to the base configuration throughout the analysis, and the strains and stresses are measured with respect to this configuration.

For the *Updated Lagrangian description*, once the last target configuration has been reached, it becomes the next reference configuration. The strains and stresses are redefined as soon as the reference configuration is updated.

In the *Co–rotational description*, which is sometimes confused with the Updated Lagrangian description, the reference configuration is split into two. Strains and stresses are measured from the co–rotated configuration while the base configuration is maintained as a reference for measuring the rigid body motions. More precisely, the idea behind the CR formulation is the splitting of the displacements into the pure deformations and rigid body motions.

In this thesis, we shall use the Total Lagrangian description for the element to be presented in Chapter 3. The same method will be used along with a special kind of Co–rotational description for the bending behavior in Chapter 4. Before proceeding, the concept of CR description is introduced in a little more detail.

The co–rotational formulation

The description of finite rotations in thin shell analysis is especially challenging. The decomposition of element motion into a deformational and rigid body motion has recently become a common practice whereby arbitrary large rotations can be described. This approach, referred to as the co–rotational (CR) method, was initially introduced by Wempner (1969), Belytschko and Hseih (1973), and Belytschko and Schwer (1977). The method has much in common with the natural approach of Argyris *et al.* (1979).

The key concept in the CR description is the splitting or decomposition of the reference configuration into two, the initial or base configuration and the co–rotated configuration. The initial configuration is kept fixed throughout the analysis, and serves as the immovable reference configuration, while the co–rotated configuration of the individual element is the rigid body motion of the element's base configuration. The element deformations are measured with respect to the co–rotated configuration as the associated coordinate system moves with the element like a shadow.

In the history of co–rotational formulation, more effort has been placed on deriving *consistent* discrete equations. By consistent it is meant that the tangent stiffness matrix is derived from a consistent differentiation of the relationships that are used for the updating. Though consistent co–rotational formulation can sometimes be quite involving in terms of the underlying variational calculus, it has the advantage that the rate of convergence is

URN:NBN:no-1282

not impaired by the size of incremental steps. In addition, it is often element independent for elements of the same geometry and connectors as demonstrated by Haugen (1994). On the contrary, inconsistent formulations may require more incremental steps and be *increment–dependent*, however, their underlying mathematics are generally simpler.

In the context of nonlinear analysis, however, a more informative load–displacement history to an engineer is the one that captures as many important points as possible. In addition, the size of incremental steps may well be limited or controlled by the degree of material nonlinearities in the structure. Consequently, a nonlinear analysis does in general require a number of incremental steps. With this in mind, the benefit of attempting to derive a consistent formulation in the present work does not justify its mathematical complexity.

As an alternative, a co–rotational formulation is invoked for the bending behavior only. The method is restricted to moderate rotational increments. In that way, only the changes of curvatures are extended to the regime of arbitrary large rotations with CR description while the membrane strains are measured in the Total Lagrangian approach. The main theme in this procedure is that the outward unit normal is rotated at the end of each increment and the incremental curvature changes are evaluated and added to the total values for updating.

A method which uses co–rotational technique only partly was proposed by Besseling (1980) and Ernst (1981), and has been applied with success by Bout (1993) and van Keulen (1993). This *inconsistent* formulation is dependent on incremental steps. A consistent and refined CR formulation of the same kind has been given by van Keulen and Booij (1996), however, the resulting equations appear to be complicated in terms of finite element implementation, and improvements in terms of accuracy appear to be very minor.

Peng and Crisfield (1992) and Zhong and Crisfield (1998) have presented alternative consistent formulation that can be applied directly to a linear version of the Morley shell element in Cartesian coordinates. It is unfortunate that a complete implementation of these formulations has not been fully successful in the present work.

2.5 Description of Geometry

The majority of the formulations in this thesis use the rectangular or Cartesian coordinate system. An exception is the geometrically nonlinear element to be presented in Chapter 3 where non–orthogonal coordinate system is used. While the Cartesian coordinate description is quite straight forward, the non–orthogonal system is somewhat more involving.

In non–orthogonal coordinates, there is a need to distinguish between various tensor components as covariant, contravariant, and physical components. In this section, a brief description of this coordinate system is given. To start, we consider the triangular element shown in Figure 2.1 where the so–called area coordinates are introduced. The non–orthogonal axes are defined by (ξ^1, ξ^2).

URN:NBN:no-1282

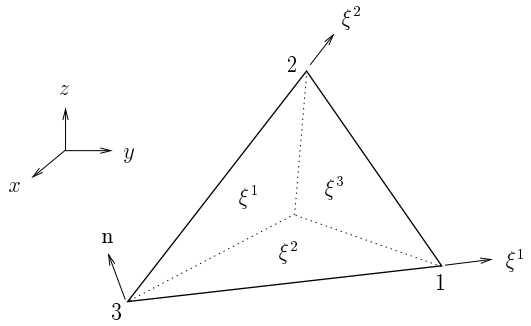

Figure 2.1 Non–orthogonal coordinates.

The position vector of a point on the undeformed mid–surface is defined with respect to the fixed rectangular or Cartesian coordinate system (x, y, z) as,

$$\hat{\boldsymbol{p}} = x\boldsymbol{e}_1 + y\boldsymbol{e}_2 + z\boldsymbol{e}_3 \tag{2.5}$$

where $\boldsymbol{e}_1$, $\boldsymbol{e}_2$ and $\boldsymbol{e}_3$ are the corresponding unit vectors for x, y and z–axes, respectively. These axes are related to non–orthogonal coordinates such that,

$$x = x_1\xi^1 + x_2\xi^2 + x_3\xi^3 \tag{2.6}$$
$$y = y_1\xi^1 + y_2\xi^2 + y_3\xi^3 \tag{2.7}$$
$$z = z_1\xi^1 + z_2\xi^2 + z_3\xi^3 \tag{2.8}$$

where x_i, y_i and z_i are respectively the magnitude of x, y and z at vertex i. The area coordinates ξ^i, which are natural for a triangular element, are defined by,

$$\xi^1 + \xi^2 + \xi^3 = 1 \qquad\qquad 0 \le \xi^i = \frac{A_i}{A} \le 1 \tag{2.9}$$

where A is the total area of the triangle and A_i is the area of one of the three sub–triangles as depicted in Figure 2.1.

Differentiation with respect to the in–plane Cartesian coordinates can be expressed in terms of the *area coordinates* such that,

$$\square_{,x} = \frac{\partial \square}{\partial x} = \frac{b_i}{2A}\frac{\partial \square}{\partial \xi^i} \qquad\qquad \square_{,y} = \frac{\partial \square}{\partial y} = \frac{a_i}{2A}\frac{\partial \square}{\partial \xi^i} \tag{2.10}$$

where $\square$ represents any variable to be differentiated, and

$$a_i = -x_j + x_k \qquad\qquad b_i = +y_j - y_k \tag{2.11}$$

in which i, j, and k take a cyclic value of 1, 2, and 3, respectively.

In non–orthogonal coordinate system, the natural base vectors are defined as,

$$\boldsymbol{g}_\alpha = \hat{\boldsymbol{p}}_{,\alpha} = x_{,\alpha}\,\boldsymbol{e}_1 + y_{,\alpha}\,\boldsymbol{e}_2 + z_{,\alpha}\,\boldsymbol{e}_3 \tag{2.12}$$

URN:NBN:no-1282

where the Greek indices take values between 1 and 2 with no sum. The subscript comma indicates the partial derivative with respect to the area coordinates ξ^α. For Equations (2.6)–(2.8), these are given by

$$x_{,1} = x_1 - x_3 \qquad x_{,2} = x_2 - x_3 \tag{2.13}$$

plus similar expressions for y and z.

The covariant components of the metric or *first fundamental tensor* of the mid–surface are defined by the scalar products of the natural base vectors as,

$$a_{\alpha\beta} = \boldsymbol{g}_\alpha \cdot \boldsymbol{g}_\beta \tag{2.14}$$

When the necessary vector products have been carried out, the result is,

$$a_{11} = l_2^2 \qquad a_{22} = l_1^2 \qquad a_{12} = a_{21} = \frac{1}{2} l_{12} \tag{2.15}$$

where l_i is the length of side i (which is defined to be opposite to vertex i) and,

$$l_{12} = l_1^2 + l_2^2 - l_3^2 \tag{2.16}$$
$$l_{23} = l_2^2 + l_3^2 - l_1^2 \tag{2.17}$$
$$l_{31} = l_3^2 + l_1^2 - l_2^2 \tag{2.18}$$

The contravariant components $a^{\alpha\beta}$ of the first fundamental tensor are obtained through the transformation,

$$a_{\alpha\beta} a^{\beta\lambda} = \delta_\alpha^\lambda \tag{2.19}$$

where δ_α^λ is the Kronecker delta. Noting that the determinant of the metric tensor provides the area of the triangle A as,

$$a = det(a_{\alpha\beta}) = 4A^2 \qquad A = \frac{1}{4}\sqrt{l_{12}l_{23} + l_{23}l_{31} + l_{31}l_{12}} \tag{2.20}$$

the contravariant components can be expressed as,

$$a^{11} = \frac{l_1^2}{4A^2} \qquad a^{22} = \frac{l_2^2}{4A^2} \qquad a^{12} = a^{21} = -\frac{l_{12}}{8A^2} \tag{2.21}$$

The unit normal vector to the undeformed middle surface of the triangle is given by,

$$\bar{\boldsymbol{k}} = \frac{1}{2}\varepsilon^{\alpha\beta}[\boldsymbol{g}_\alpha \cdot \boldsymbol{g}_\beta] = n^1 \boldsymbol{e}_1 + n^2 \boldsymbol{e}_2 + n^3 \boldsymbol{e}_3 \tag{2.22}$$
$$\varepsilon^{11} = \varepsilon^{22} = 0 \qquad \varepsilon^{12} = -\varepsilon^{21} = 1/\sqrt{a}$$

where $\varepsilon^{\alpha\beta}$ is the contravariant permutation tensor, and n^i are the Cartesian components of the unit normal,

$$\boldsymbol{n} = \begin{bmatrix} n^1 \\ n^2 \\ n^3 \end{bmatrix} = \frac{1}{2A} \begin{bmatrix} y_{,1}z_{,2} - z_{,1}y_{,2} \\ z_{,1}x_{,2} - x_{,1}z_{,2} \\ x_{,1}y_{,2} - y_{,1}x_{,2} \end{bmatrix} \tag{2.23}$$

URN:NBN:no-1282

2.6 Description of Motion

When considering arbitrary large displacements, it is necessary to distinguish between the *initial* undeformed state of the structure and the *current* deformed state. These configurations are illustrated in Figure 2.2 for a particle of a body or structure. Note that for the present section, and only in this section, we have selected to denote the three axes in terms of components X_i and x_i for convenient tensorial presentation.

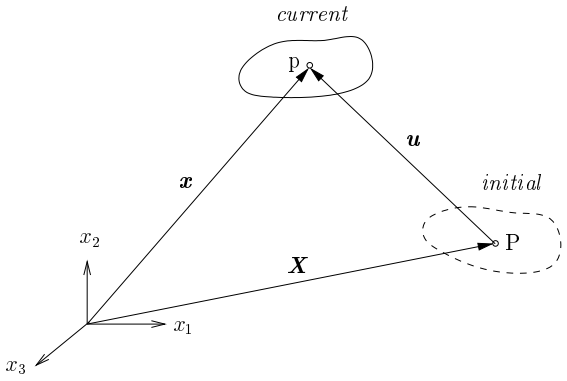

Figure 2.2 The reference and current configurations.

In the undeformed initial configuration, the position vector of a particle is described by the coordinates X_i of a fixed coordinate system. When the structure moves to the current configuration, the position vector is defined by the coordinates x_i. The X_i coordinates are usually known as the *material* coordinates, whereas x_i are known as the *spatial* coordinates.

In the so–called Lagrangian description, the current configuration is defined with reference to the initial configuration. In other words, the material coordinates are the independent variables. This implies,

$$dx_i = \frac{\partial x_i}{\partial X_j} dX_j = F_{ij} dX_j \tag{2.24}$$

where F_{ij} are components of the so–called matrix of deformation gradients. The determinant of this matrix is known as Jacobian,

$$J = det(F_{ij}) > 0 \tag{2.25}$$

2.6.1 Strain and Stress Measures

The strains are the measure of deformations in the material and they are independent of the rigid body motions. A strain tensor is defined as a change in distance of two particles

URN:NBN:no-1282

when the structure moves from the initial to the current configuration. There are different strain measures with their corresponding stress measures. In the present section, however, only the so–called Green–Lagrange strain tensor is focused.

In Lagrangian description, the change in distance can be obtained from,

$$\Delta l = dl^2 - dL^2 = dx_i dx_i - dX_i dX_i = 2dX_i E_{ij} dX_j \tag{2.26}$$

where E_{ij} is the components of the Green–Lagrange strain tensor which was introduced by Green in 1841 and St. Venant in 1844. These components are given by,

$$E_{ij} = \frac{1}{2}\left(F_{ki}F_{kj} - \delta_{ij}\right) \tag{2.27}$$

where δ_{ij} is the Kronecker delta. With reference to Figure 2.2, the position vector of a particle in the current configuration is given by,

$$x_i = X_i + u_i \tag{2.28}$$

where u_i is the displacement vector. As a result of Equation (2.28), the deformation gradient (2.24) becomes,

$$F_{ij} = \frac{\partial u_i}{\partial X_j} + \delta_{ij} \tag{2.29}$$

When this gradient is inserted into Equation (2.27), the components of the Green–Lagrange strain tensor become,

$$E_{ij} = \frac{1}{2}\left(\frac{\partial u_i}{\partial X_j} + \frac{\partial u_j}{\partial X_i} + \frac{\partial u_k}{\partial X_i}\frac{\partial u_k}{\partial X_j}\right) \tag{2.30}$$

The stress tensor which is energy conjugate to the Green–Lagrange strain tensor, is the so–called second Piola–Kirchhoff stress tensor. It was introduced by Piola in 1833 and by Kirchhoff in 1852. The components of this stress tensor are given by,

$$S_{kl} = J\frac{\partial X_k}{\partial x_i}\sigma_{ij}\frac{\partial X_l}{\partial x_j} \tag{2.31}$$

where σ_{ij} are the components of the Cauchy or true stress tensor. Detailed derivation of Equation (2.31) can be found in several publications such as Malvern (1969).

Assuming small strains and rotations, the Jacobian is approximately equal to unity and the various stress measures are approximately equal. This will be the basic assumption for the material plasticity formulation to be presented in Chapter 5. As a consequence, the Cauchy stress tensor will substitute the second Piola–Kirchhoff stress tensor.

URN:NBN:no-1282

2.7 Shell Forces

Before discussing the resultant forces acting within the shell element, it is important to introduce the concept of *material sampling points*. These are the points where the plasticity flow equations are integrated to obtain stresses and material modular matrix. In this respect, two types of stress distributions are considered within the element — the distribution along the element plane and the distribution over the shell thickness.

Since the element formulations in this thesis assume constant stress distribution over the area, the area integration is not required. However, through–the thickness integration need to be performed. If resultants plasticity is used, this is performed analytically. Numerically, this integration is performed along with the plasticity computations. In this procedure, the shell is usually divided into several layers and the stresses and modular matrices are evaluated in these layers. In the present work, the overall contribution from individual layers is achieved through the Gaussian integration technique.

2.7.1 Stress Resultants

Consider Figure 2.3 which shows a general shell with thickness t perpendicular to the mid–surface. The x and y–axes represent the orthogonal rectilinear coordinates on the middle surface and z is the distance along the normal to that surface. Corresponding to these axes, are the respective triplet of mutually orthogonal unit vectors $\boldsymbol{e}_1$, $\boldsymbol{e}_2$, and $\boldsymbol{e}_3$. They represent a point or particle on the middle surface and are oriented such that $\boldsymbol{e}_1$ and $\boldsymbol{e}_2$ are tangent to x and y–axes, respectively, and $\boldsymbol{e}_3$ is normal to the mid–surface.

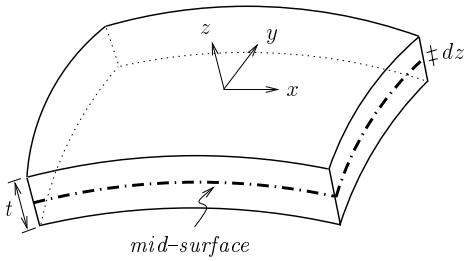

Figure 2.3 General shell geometry.

Assuming Kirchhoff–Love theory, that plane sections remain plane, the kinematics of the middle surface of the shell determines the deformation of the entire shell. Therefore, the problem is reduced from three to two dimensions with two independent variables being x and y. Based on this assumption the strains at any point of the shell can be expressed as,

$$\boldsymbol{\epsilon} = \boldsymbol{\gamma} + z\boldsymbol{\chi} \tag{2.32}$$

where the first and second terms represent the symmetric extensional and the flexural strains, respectively. These strains define the entire deformation.

URN:NBN:no-1282

The generalized forces to be considered are stress resultants $\boldsymbol{N}$ and stress couples $\boldsymbol{M}$. The stress resultants are associated with membrane forces whereas the stress couples are the results of bending moments. The generalized forces are obtained by integrating the stress distribution through the thickness of the shell such that,

$$\boldsymbol{N} = \int_t \boldsymbol{\sigma}\, dz, \qquad \boldsymbol{M} = \int_t \boldsymbol{\sigma} z\, dz, \tag{2.33}$$

where $\boldsymbol{\sigma}$ is the stress tensor conjugate to $\boldsymbol{\epsilon}$. In what follows, both $\boldsymbol{N}$ and $\boldsymbol{M}$ will be referred to as *stress resultants* for simplicity. With resultant plasticity, Equation (2.33) is pre–integrated analytically by neglecting any partial yielding within the shell cross–section.

2.7.2 Constitutive Equations

The constitutive laws or constitutive equations define the relationship between the stresses and strains within the material. For elements to be presented in Chapters 3 and 4, the constitutive equations need to be formulated in terms of stress resultants. This is irrespective of whether stress resultants or through–the thickness integration is used.

For elasto–plastic material formulation, it is necessary to express the constitutive laws in incremental form. Starting from Equation (2.32), the incremental strains can be expressed by means of variational calculus as,

$$\delta\boldsymbol{\epsilon} = \delta\boldsymbol{\gamma} + z\delta\boldsymbol{\chi} \tag{2.34}$$

where $\boldsymbol{\gamma}$ are the membrane strains, $\boldsymbol{\chi}$ are the changes of curvature, and z is the distance along the shell thickness.

At a given integration point, the incremental stresses are related to the incremental strains through the tangent modular matrix $\mathbb{C}_t$ as,

$$\delta\boldsymbol{\sigma} = \mathbb{C}_t\, \delta\boldsymbol{\epsilon} \tag{2.35}$$

In stress resultants representation, Equation (2.35) need to be expressed in terms of generalized variables.

The relation between the generalized stresses and strains can be achieved by substituting Equation (2.32) and (2.35) into (2.33). This leads to,

$$\begin{bmatrix}\delta\boldsymbol{N}\\ \delta\boldsymbol{M}\end{bmatrix} = \int_t \mathbb{C}_t \begin{bmatrix}\delta\boldsymbol{\gamma} + z\delta\boldsymbol{\chi}\\ z\delta\boldsymbol{\gamma} + z^2\delta\boldsymbol{\chi}\end{bmatrix} dz = \begin{bmatrix}\boldsymbol{C} & \boldsymbol{X}\\ \boldsymbol{X}^T & \boldsymbol{D}\end{bmatrix}\begin{bmatrix}\delta\boldsymbol{\gamma}\\ \delta\boldsymbol{\chi}\end{bmatrix} \tag{2.36}$$

where the sub–matrices are defined by,

$$\boldsymbol{C} = \int_t \mathbb{C}_t\, dz \qquad \boldsymbol{X} = \int_t \mathbb{C}_t z\, dz \qquad \boldsymbol{D} = \int_t \mathbb{C}_t z^2\, dz \tag{2.37}$$

URN:NBN:no-1282

Analogous to Equation (2.36), the corresponding tensors and tangent modular matrix in terms of generalized variables are given by,

$$\bar{\boldsymbol{\sigma}} = \begin{bmatrix} \boldsymbol{N} \\ \boldsymbol{M} \end{bmatrix} \qquad \bar{\boldsymbol{\epsilon}} = \begin{bmatrix} \boldsymbol{\gamma} \\ \boldsymbol{\chi} \end{bmatrix} \qquad \bar{\mathbb{C}}_t = \begin{bmatrix} \boldsymbol{C} & \boldsymbol{X} \\ \boldsymbol{X}^T & \boldsymbol{D} \end{bmatrix} \tag{2.38}$$

For elastic material, the sub–matrices are obtained directly by analytical integration of Equation (2.36). In that case, the elastic resultant modular matrix becomes,

$$\bar{\mathbb{C}} = \begin{bmatrix} t\mathbb{C} & \mathbf{0} \\ \mathbf{0} & \frac{t^3}{12}\mathbb{C} \end{bmatrix} \tag{2.39}$$

where $\mathbb{C}$ is the symmetric 3×3 elastic modular matrix for plane stress condition.

2.8 The Constant Stress Shell Element

Since shells are often curved, one may think that only curved elements can be used. However, flat elements involving an assembly of plate and membrane elements have been frequently used to approximate the curved shell surface. Some of the earliest work on linear finite element involved facet formulation, and the concept appears to have first been extended to nonlinear analysis by Horrigmoe and Bergan (1978) using the co–rotational approach.

There exists a number of flat (or facet) shell elements for nonlinear analysis. Every formulation is not always superior for all problems and its degree in computational efficiency is an important factor. More precisely, there are computationally expensive and cheap elements as well as mathematically complex and simple elements. In the choice of finite element modelling, a particular geometrically nonlinear shell element can be preferred based on the range of problems it can solve. One of the simplest and most efficient finite elements is the constant stress resultants shell element, which is commonly known as the Morley element. This element type is the primary focus in this thesis.

The linear version of the Morley shell involves a combination of the constant–strain membrane triangle of Turner *et al.* (1956) and a constant–moment bending triangle. The former appears to be the first finite element ever designed. The latter was originally derived by Hellan (1967) and Herrmann (1967) who used the Hellinger–Reissner variation principle. Later, Morley (1971) derived an equivalent displacement–based element through the principle of minimum potential energy.

Many researchers have applied the Morley shell element in problems involving large displacements and rotations. Examples are the works of Herrmann and Campbell (1968), Dawe (1972), and Peric and Owen (1991). Similar works have been reported by Bäcklund (1973) and Chen (1979), who used an updated Lagrangian technique, and by Peng and Crisfield (1992) using a co–rotational formulation. Bout (1993) and van Keulen (1993) have also presented a similar formulation that is capable of handling initial curvature.

URN:NBN:no-1282

Another type of a simple shell finite element combines the constant–strain membrane triangle of Turner *et al.* (1956) with a Discrete Kirchhoff plate bending element. The latter can be found in the works of Stricklin *et al.* (1969), Batoz *et al.* (1980), Batoz (1982), and Jeyachandrabose *et al.* (1985), (see also Cook *et al.* (1989), and Talbot and Dhatt (1986)). This 18–degrees–of–freedom linear facet shell element is also extended to include geometric nonlinearity through the CR or UL formulations. Yet, the resulting element is not as simple as the Morley type shell element, and the drilling degrees of freedom need to be treated carefully.

Based on von Kàrmàn nonlinear theory, Providas (1990) and Morley (1991) described a geometrically nonlinear Morley shell element that passes the nonlinear patch test and is valid for moderate rotations. They assumed quadratic polynomials for both in–plane and out–of–plane displacements and derived the local equations in the non–orthogonal coordinate system.

Using linear and quadratic polynomials for in–plane and out–of–plane displacements, respectively, Providas (1990) and Providas and Kattis (1999) described a simpler version of the Morley nonlinear triangle that performs equally well. In this version, the influence of the changes of curvature on the membrane strains was neglected as a search for further simplicity.

URN:NBN:no-1282

URN:NBN:no-1282

Chapter 3

Facet Element with Moderate Rotations

3.1 Introduction

As mentioned in Chapter 2, the Morley shell element has been widely used in nonlinear finite elements through either the co–rotational or updated Lagrangian descriptions. The element involves a combination of the constant–strain membrane triangle of Turner *et al.* (1956) and a constant–moment bending triangle of Morley (1971).

A complete nonlinear shell finite element which passes the nonlinear von Kármán patch test was re–derived by Morley (1991) under Kirchhoff theory from Hu–Washizu functional. As a consequence of the nonlinear von Kármán theory, the element is only valid under moderate rotations. The elastic formulation has been studied by Providas (1990) and has shown good performance within its range of validity.

During the preparation of this thesis, numerical investigations have shown that the new element developed by Morley (1991) is much simpler and about 2.5–5 times faster than many of its predecessors in co–rotational formulation. Despite its simplicity and efficient applicability in problems involving moderate rotations, this element has not received much attention in the literature.

In fact, there exists a large number of practical problems or applications in which the structure undergoes plastic deformations with rotations remaining essentially moderate. It has also been pointed out by Koiter (1966) that it is hardly necessary to allow for significant large displacements as for most practical purposes many shell structures would become quite unserviceable.

By realizing these facts and the simplicity and efficiency of the Morley (1991) element, it is interesting to extend it for material plasticity before modifying for large rotations.

URN:NBN:no-1282

During the preparation of this thesis, it has been established that any attempt to include large rotations would introduce a degree of complexity and increase the computational time as far as five times.

In the present chapter, the element matrices are extended to include material nonlinearities. The resulting formulation will be assessed in subsequent chapters for its performance in the buckling and collapse analysis. An alternative to this element is discussed in Chapter 4 where another Morley element capable of handling large rotations is presented.

3.2 Element Kinematics and Basic Equations

Before proceeding with elasto–plastic element matrices, it is important to start with an outline of the necessary definitions and kinematics of the element for completeness. For detailed derivations, reference is made to Morley (1991) and Providas (1990). In addition, the element makes full use of the concept of *practical components* especially for transformations, and for that part the reader is also referred to the work of Morley (1987).

The local element system, including all the derivations, are defined in non–orthogonal coordinate system. Within the plasticity formulation, however, the local system will be referred to the xy–coordinates (see Figure 3.1). The global coordinates are described as Cartesian (X, Y, Z).

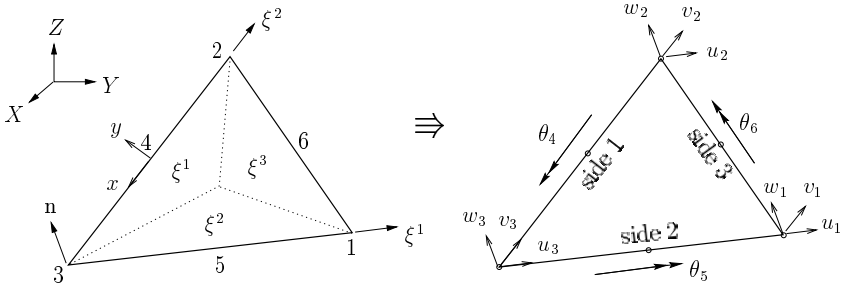

Figure 3.1 Element geometry and degrees of freedom.

The element has six nodes and twelve degrees of freedom. Namely, the three displacements at each of the corner nodes, and one rotation at each of the mid–side nodes (Figure 3.1). At the local level, the curvature tensor replaces the rotations so that the resulting expressions are simplified. As a result, the vector with element degrees of freedom in the local non–orthogonal ξ^α–coordinate system takes the following form,

$$\boldsymbol{r}^T = \begin{pmatrix} \boldsymbol{u}^T & \boldsymbol{w}^T & \boldsymbol{\kappa}^T \end{pmatrix} \tag{3.1}$$

where $\boldsymbol{u}$, $\boldsymbol{w}$, and $\boldsymbol{\kappa}$, are the in–plane displacement vector, out–of–plane displacement vec-

URN:NBN:no-1282

tor, and curvature tensor, respectively. These are given as,

$$\boldsymbol{u}^T = (u_1 \quad v_1 \quad u_2 \quad v_2 \quad u_3 \quad v_3) \tag{3.2}$$

$$\boldsymbol{w}^T = (w_1 \quad w_2 \quad w_3) \tag{3.3}$$

$$\boldsymbol{\kappa}^T = (\kappa_{11} \quad \kappa_{22} \quad \kappa_{12}) \tag{3.4}$$

in which u_j, v_j, and w_j are the respective displacements at vertex j, and κ_{ij} are the components of the curvature tensor, all in ξ^α–coordinates.

3.2.1 Strain–displacement Equations

The strain tensor is described by the von Kármán (1910) nonlinear theory. It is similar to the Green–Lagrange strain tensor (2.30) when the in–plane quadratic terms of displacements are neglected. In the von Kármán (1910) nonlinear theory, the middle surface strain and curvature tensors are expressed as,

$$\varepsilon_{\alpha\beta} = \frac{1}{2}\left(u_{\alpha,\beta} + u_{\beta,\alpha} + w_{,\alpha} w_{,\beta}\right) \tag{3.5}$$

$$\kappa_{\alpha\beta} = w_{,\alpha\beta} \tag{3.6}$$

where u_α ($u_1 = u$, $u_2 = v$) and w are the in–plane and out–of–plane displacement components, respectively.

The displacement field is defined by quadratic functions of the triangular coordinates for both in–plane and out–of–plane displacements (u_i, v_i, w_i) such that,

$$u = u_1\xi^1 + u_2\xi^2 + u_3\xi^3 + \omega_1\xi^2\xi^3 + \omega_2\xi^3\xi^1 + \omega_3\xi^1\xi^2 \tag{3.7}$$

$$v = v_1\xi^1 + v_2\xi^2 + v_3\xi^3 + \omega_4\xi^2\xi^3 + \omega_5\xi^3\xi^1 + \omega_6\xi^1\xi^2 \tag{3.8}$$

$$w = w_1\xi^1 + w_2\xi^2 + w_3\xi^3 + \psi_4\xi^2\xi^3 + \psi_5\xi^3\xi^1 + \psi_6\xi^1\xi^2 \tag{3.9}$$

where ω_i and ω_{i+3} are constants. These constants are determined in terms of w_i and ψ_{i+3} by requiring satisfaction of continuity conditions at each mid–side nodes (see Morley (1991)). The coefficients ψ_{i+3} can be regarded as a measure of deflections of the mid–sides and are illustrated in Figure 3.2.

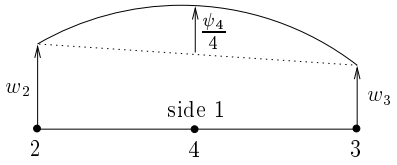

Figure 3.2 The components ψ_{i+3} as a measure of deflection.

Making the necessary substitution of the displacement fields into Equation (3.5), and following the procedures as in Morley (1991) and Providas (1990), the membrane strain

URN:NBN:no-1282

tensor in the local non–orthogonal system is obtained as,

$$\boldsymbol{\varepsilon} = \boldsymbol{B}_u \boldsymbol{u} + \frac{1}{2}\boldsymbol{B}_w \boldsymbol{w} + \frac{1}{2}\boldsymbol{B}_k \boldsymbol{\kappa} \tag{3.10}$$

where $\boldsymbol{B}_u$, $\boldsymbol{B}_w$, and $\boldsymbol{B}_k$, are the strain–displacement matrices which are defined as,

$$\boldsymbol{B}_u = \frac{1}{2}\begin{bmatrix} 2 & 0 & 0 & 0 & -2 & 0 \\ 0 & 0 & 0 & 2 & 0 & -2 \\ 0 & 1 & 1 & 0 & -1 & -1 \end{bmatrix} \tag{3.11}$$

$$\boldsymbol{B}_w = \frac{1}{2}\begin{bmatrix} 2(w_1 - w_3) & 0 & -2(w_1 - w_3) \\ 0 & 2(w_2 - w_3) & -2(w_2 - w_3) \\ w_2 - w_3 & w_1 - w_3 & -w_1 - w_2 + 2w_3 \end{bmatrix} \tag{3.12}$$

$$\boldsymbol{B}_k = \frac{1}{12}\begin{bmatrix} \kappa_{11} + \kappa_{22} & \kappa_{11} & -2\kappa_{12} \\ \kappa_{22} & \kappa_{11} + \kappa_{22} & -2\kappa_{12} \\ \kappa_{12} & \kappa_{12} & \kappa_{11} + \kappa_{22} - 3\kappa_{12} \end{bmatrix} \tag{3.13}$$

Providas and Kattis (1999) have proposed a rather simpler but similar element. They used linearly varying membrane shape functions while retaining the quadratic functions for out–of–plane displacements. In their resulting strain tensor, which is similar to Equation (3.10), they have neglected the term involving curvature. This formulation is also implemented along with the present element. For a number of problems, the simpler element appears to perform equally well with the detailed Morley (1991) element.

3.2.2 Transformation Matrices

Due to different local systems referred for the element and material formulations, two different transformation matrices are required. The first is a 12×12 matrix relating the local element matrices and vectors in non–orthogonal ξ^α–coordinates to the corresponding values in global Cartesian coordinates (X, Y, Z). This will be referred to as the element transformation matrix.

The second is a 3×3 matrix needed in the plasticity calculations to relate the material modular matrix, strain and curvature tensors in the local ξ^α–coordinate system to the same values given in the local xy–coordinate system. This will be called the material transformation matrix.

Element transformation matrix

All element movements are related to the initial configuration of the facet surface. Therefore, the element transformation matrix $\boldsymbol{T}$ can be build–up using the initial global coordinates of the element. At the current configuration, the local vectors and matrices are

URN:NBN:no-1282

related to their corresponding global ones by the following expressions,

$$\boldsymbol{r} = \boldsymbol{T}\boldsymbol{r}_g \qquad \boldsymbol{f}_g = \boldsymbol{T}^T\boldsymbol{f} \qquad \boldsymbol{K}_g = \boldsymbol{T}^T\boldsymbol{K}\boldsymbol{T} \tag{3.14}$$

where $\boldsymbol{r}$, $\boldsymbol{f}$, and $\boldsymbol{K}$ are respectively the element displacement vector, internal force vector, and element stiffness matrix in the local ξ^α–coordinate system. The subscript g represents the same vectors and matrix in the global XYZ–coordinate system.

As opposed to Equation (3.1), the element global displacement vector is re–arranged such that,

$$\boldsymbol{r}_g = (U_1 \;\; V_1 \;\; W_1 \;\; U_2 \;\; V_2 \;\; W_2 \;\; U_3 \;\; V_3 \;\; W_3 \;\; \theta_4 \;\; \theta_5 \;\; \theta_6)^T \tag{3.15}$$

Then, following the procedures as in Morley (1991) and Providas (1990), with the local displacement vectors in the local system arranged as in Equations (3.1)–(3.4), the constant transformation matrix $\boldsymbol{T}$ can be obtained as,

$$\boldsymbol{T} = \begin{bmatrix} \boldsymbol{T}_a & \boldsymbol{0}_{2\times3} & \boldsymbol{0}_{2\times3} & \boldsymbol{0}_{2\times3} \\ \boldsymbol{0}_{2\times3} & \boldsymbol{T}_a & \boldsymbol{0}_{2\times3} & \boldsymbol{0}_{2\times3} \\ \boldsymbol{0}_{2\times3} & \boldsymbol{0}_{2\times3} & \boldsymbol{T}_a & \boldsymbol{0}_{2\times3} \\ \boldsymbol{T}_{n1} & \boldsymbol{T}_{n2} & \boldsymbol{T}_{n3} & \boldsymbol{0}_{3\times3} \\ \boldsymbol{T}_{c1}\boldsymbol{n}^T & \boldsymbol{T}_{c2}\boldsymbol{n}^T & \boldsymbol{T}_{c3}\boldsymbol{n}^T & \boldsymbol{T}_\theta \end{bmatrix} \tag{3.16}$$

where $\boldsymbol{T}_{ci}$ is a column matrix with elements given by column i of matrix $\bar{\boldsymbol{c}}$ defined below, $\boldsymbol{T}_{ni}$ is a 3×3 partial–null matrix in which row i is defined by the transpose of vector $\boldsymbol{n}$ in Equation (2.23), and

$$\bar{\boldsymbol{c}} = \begin{bmatrix} -\frac{l_{23}}{l_3^2} & \frac{l_{12}}{l_1^2} + \frac{l_{23}}{l_3^2} & -\frac{l_{12}}{l_1^2} \\ \frac{l_{12}}{l_2^2} + \frac{l_{31}}{l_3^2} & -\frac{l_{31}}{l_3^2} & -\frac{l_{12}}{l_2^2} \\ \frac{l_{31}}{l_3^2} & \frac{l_{23}}{l_3^2} & -2 \end{bmatrix} \tag{3.17}$$

$$\boldsymbol{T}_\theta = \begin{bmatrix} \frac{4A}{l_1} & 0 & \frac{4A}{l_3} \\ 0 & \frac{4A}{l_2} & \frac{4A}{l_3} \\ 0 & 0 & \frac{4A}{l_3} \end{bmatrix} \qquad \boldsymbol{T}_a = \begin{bmatrix} x_{,1} & y_{,1} & z_{,1} \\ x_{,2} & y_{,2} & z_{,2} \end{bmatrix} \tag{3.18}$$

in which the partial derivatives of x, y and z are given as in Equation (2.13).

It is important to note that a proper sign convention should be defined for the element rotations to obtain continuity at the common side of the two adjacent elements. This sign is to be applied to the element rotations prior to the system assembly. For convenience, one may decide to apply this effect only in the transformation matrix $\boldsymbol{T}$ by multiplying the corresponding three columns, each with its respective sign.

Material transformation matrix

The plasticity formulation that will be presented in Chapter 5 is based on Cartesian coordinate system. The present element, however, is defined in non–orthogonal coordinate

URN:NBN:no-1282

system. Therefore, for this element to be able to use the present plasticity formulation, a material transformation matrix is required.

The transformation should provide the components of the strain and curvature tensors in the local xy–coordinates $(\boldsymbol{\varepsilon}^{(xy)}, \boldsymbol{\kappa}^{(xy)})$, or the corresponding components of the conjugate stress resultants in the local ξ^α–coordinates $(\boldsymbol{N}, \boldsymbol{M})$. This can be achieved by applying the transformation matrix $\boldsymbol{H}$ so that,

$$\begin{aligned} \boldsymbol{\varepsilon}^{(xy)} &= \boldsymbol{H}\boldsymbol{\varepsilon} & \boldsymbol{N} &= \boldsymbol{H}^T\boldsymbol{N}^{(xy)} \\ \boldsymbol{\kappa}^{(xy)} &= \boldsymbol{H}\boldsymbol{\kappa} & \boldsymbol{M} &= \boldsymbol{H}^T\boldsymbol{M}^{(xy)} \end{aligned} \tag{3.19}$$

where,

$$\boldsymbol{H} = \begin{bmatrix} h^1_{1'}h^1_{1'} & h^2_{1'}h^2_{1'} & 2h^1_{1'}h^2_{1'} \\ h^1_{2'}h^1_{2'} & h^2_{2'}h^2_{2'} & 2h^1_{2'}h^2_{2'} \\ h^1_{1'}h^1_{2'} & h^2_{1'}h^2_{2'} & h^1_{1'}h^2_{2'} + h^2_{1'}h^1_{2'} \end{bmatrix} \tag{3.20}$$

The terms $h^\alpha_{\alpha'}$ in Equation (3.20) are helpful in deriving expressions for the so–called practical components of surface vectors and tensors resolved from the ξ^α–coordinate system to the xy–coordinate system (see Morley (1987)). These terms are different for each element side, and the resulting xy–coordinates will be oriented as tangential and normal to the side concerned.

In the case of isotropic material, it is enough to select one specific side. Accordingly, matrix $\boldsymbol{H}$ is constructed for side number 1 for which the following terms apply,

$$h^1_{1'} = -\frac{l_1}{2A} \qquad h^2_{1'} = \frac{l_{12}}{4Al_1} \qquad h^1_{2'} = 0 \qquad h^2_{2'} = -\frac{1}{l_1}$$

The coordinate orientation for this side is illustrated in Figure 3.1.

3.3 The Elasticity Modular Matrix

Another difficulty in implementing material plasticity with the present element, is the unconventional way of representing the elasticity matrix. Perhaps for seeking the symmetry of the element matrices, Morley (1991) expressed this matrix for isotropic material as,

$$\mathbb{C}' = \frac{E}{1-\nu^2}\begin{bmatrix} 1 & \nu & 0 \\ \nu & 1 & 0 \\ 0 & 0 & c(1-\nu) \end{bmatrix} \tag{3.21}$$

where E is the Young's modulus, ν is the Poisson's ratio, and the constant $c = 2$.

As a result of this definition, the components of the strain tensor, forces, and moments in the local ξ^α–system appear as,

$$\boldsymbol{\varepsilon}^T = [\varepsilon_{11} \quad \varepsilon_{22} \quad \epsilon_{12}] \tag{3.22}$$

$$\boldsymbol{N}^T = \begin{bmatrix} N^{11} & N^{22} & 2N^{12} \end{bmatrix} \tag{3.23}$$

$$\boldsymbol{M}^T = \begin{bmatrix} M^{11} & M^{22} & 2M^{12} \end{bmatrix} \tag{3.24}$$

URN:NBN:no-1282

Since we will encounter a conventional representation of the elasticity matrix with $c = 1/2$ in the next chapter, it is convenient to let c carry its parametric value. This will be especially advantageous in Chapter 5 where simplified and explicit plasticity equations are derived.

Equation (3.21) is defined in the local xy–coordinate system. In the local ξ^α–coordinates, the transformation matrix $\boldsymbol{H}$ can be used such that,

$$\mathbb{C} = \boldsymbol{H}^T \mathbb{C}' \boldsymbol{H} \tag{3.25}$$

plus a similar transformation for $\boldsymbol{C}$, $\boldsymbol{X}$ and $\boldsymbol{D}$ defined in Equation (2.36).

All the aspects pointed out in this section, need to be treated carefully in order to use the plasticity formulation discussed in Chapter 5. These include the material transformations as well as the factor of 2 in the shear terms of the stress resultant tensor.

3.4 Elasto–Plastic Element Matrices

The element matrices can be derived from the internal virtual work term in the balance Equation (2.1). In addition, the resultants expression of the constitutive Equation (2.36) are used. Since the stresses are constant over the element, we can drop the integral over the area and multiply the expression directly by the initial area A of the triangle. Accordingly, we can write,

$$\delta W^i = A \delta \boldsymbol{e}^T \boldsymbol{s} = A \begin{bmatrix} \delta \boldsymbol{\varepsilon}^T & \delta \boldsymbol{\kappa}^T \end{bmatrix} \begin{bmatrix} \boldsymbol{N} \\ \boldsymbol{M} \end{bmatrix} \tag{3.26}$$

where $\boldsymbol{s}$ is the stress resultant tensor, and $\boldsymbol{e}$ is the conjugate strain and curvature tensor. Note that we have purposely used the notations $\boldsymbol{s}$ and $\boldsymbol{e}$ for the present chapter only.

The element *internal force vector* in terms of nodal forces is obtained directly by working out the internal virtual work. Substitution of Equation (3.10) into (3.26) yields,

$$\begin{aligned} \delta W^i &= A \begin{bmatrix} \delta \boldsymbol{u}^T \boldsymbol{B}_u^T + \delta \boldsymbol{w}^T \boldsymbol{B}_w^T + \delta \boldsymbol{\kappa}^T \boldsymbol{B}_k^T & \delta \boldsymbol{\kappa}^T \end{bmatrix} \begin{bmatrix} \boldsymbol{N} \\ \boldsymbol{M} \end{bmatrix} \\ &= A \begin{bmatrix} \delta \boldsymbol{u}^T \boldsymbol{B}_u^T \boldsymbol{N} + \delta \boldsymbol{w}^T \boldsymbol{B}_w^T \boldsymbol{N} + \delta \boldsymbol{\kappa}^T \boldsymbol{B}_k^T \boldsymbol{N} + \delta \boldsymbol{\kappa}^T \boldsymbol{M} \end{bmatrix} \\ &= \begin{bmatrix} \delta \boldsymbol{u}^T & \delta \boldsymbol{w}^T & \delta \boldsymbol{\kappa}^T \end{bmatrix} \boldsymbol{f} \end{aligned} \tag{3.27}$$

where the element internal force vector comes out as,

$$\boldsymbol{f} = A \begin{bmatrix} \boldsymbol{B}_u^T \boldsymbol{N} \\ \boldsymbol{B}_w^T \boldsymbol{N} \\ \boldsymbol{B}_k^T \boldsymbol{N} + \boldsymbol{M} \end{bmatrix} \tag{3.28}$$

The *tangent stiffness matrix* may be obtained through the variation of Equation (3.26), which can be expressed as

$$\delta^2 W^i = A(\delta \boldsymbol{e}^T \delta \boldsymbol{s} + \delta^2 \boldsymbol{e}^T \boldsymbol{s}) \tag{3.29}$$

URN:NBN:no-1282

In working out Equation (3.29), it is convenient to re–write the following products that appear in the geometric part of the tangent stiffness,

$$\delta \boldsymbol{B}_w^T \boldsymbol{N} = \boldsymbol{B}_{Gw} \delta \boldsymbol{w} \qquad \delta \boldsymbol{B}_k^T \boldsymbol{N} = \boldsymbol{B}_{Gk} \delta \boldsymbol{\kappa} \tag{3.30}$$

where,

$$\boldsymbol{B}_{Gw} = \begin{bmatrix} N^{11} & N^{12} & -(N^{11}+N^{12}) \\ & N^{22} & -(N^{22}+N^{12}) \\ sym & & N^{11}+N^{22}+2N^{12} \end{bmatrix} \tag{3.31}$$

$$\boldsymbol{B}_{Gk} = \begin{bmatrix} N^{11} & N^{11}+N^{22} & 2N^{12} \\ & N^{22} & 2N^{12} \\ sym & & -2(N^{11}+N^{22}-3N^{12}) \end{bmatrix} \tag{3.32}$$

Then, by making use of Equations (3.10), (2.36), and (3.30), Equation (3.29) may be worked out as,

$$\begin{aligned} \delta^2 W^i &= A \left(\begin{bmatrix} \delta \boldsymbol{u}^T \boldsymbol{B}_u^T + \delta \boldsymbol{w}^T \boldsymbol{B}_w^T + \delta \boldsymbol{\kappa}^T \boldsymbol{B}_k^T & \delta \boldsymbol{\kappa}^T \end{bmatrix} \begin{bmatrix} \boldsymbol{C} & \boldsymbol{X} \\ \boldsymbol{X}^T & \boldsymbol{D} \end{bmatrix} \begin{bmatrix} \delta \boldsymbol{\epsilon} \\ \delta \boldsymbol{\kappa} \end{bmatrix} \right. \\ &\quad \left. + \begin{bmatrix} \delta \boldsymbol{w}^T \delta \boldsymbol{B}_w^T + \delta \boldsymbol{\kappa}^T \delta \boldsymbol{B}_k^T & \boldsymbol{0} \end{bmatrix} \begin{bmatrix} \boldsymbol{N} \\ \boldsymbol{M} \end{bmatrix} \right) \\ &= A \begin{bmatrix} \delta \boldsymbol{u}^T & \delta \boldsymbol{w}^T & \delta \boldsymbol{\kappa}^T \end{bmatrix} \left(\begin{bmatrix} \boldsymbol{B}_u^T & \boldsymbol{0} \\ \boldsymbol{B}_w^T & \boldsymbol{0} \\ \boldsymbol{B}_k^T & \boldsymbol{I} \end{bmatrix} \begin{bmatrix} \boldsymbol{C} & \boldsymbol{X} \\ \boldsymbol{X}^T & \boldsymbol{D} \end{bmatrix} \begin{bmatrix} \boldsymbol{B}_u & \boldsymbol{B}_w & \boldsymbol{B}_k \\ \boldsymbol{0} & \boldsymbol{0} & \boldsymbol{I} \end{bmatrix} \right. \\ &\quad \left. + \begin{bmatrix} \boldsymbol{0} & \boldsymbol{0} & \boldsymbol{0} \\ \boldsymbol{0} & \boldsymbol{B}_{Gw} & \boldsymbol{0} \\ \boldsymbol{0} & \boldsymbol{0} & \boldsymbol{B}_{Gk} \end{bmatrix} \right) \begin{bmatrix} \delta \boldsymbol{u} \\ \delta \boldsymbol{w} \\ \delta \boldsymbol{\kappa} \end{bmatrix} \\ &= \delta \boldsymbol{r}^T \boldsymbol{K}_t \delta \boldsymbol{r} \end{aligned} \tag{3.33}$$

where $\boldsymbol{K}_t$ is the symmetric tangent stiffness matrix given by,

$$\boldsymbol{K}_t = A \begin{bmatrix} \boldsymbol{B}_u^T \boldsymbol{C} \boldsymbol{B}_u & \boldsymbol{B}_u^T \boldsymbol{C} \boldsymbol{B}_w & \boldsymbol{B}_u^T \boldsymbol{C} \boldsymbol{B}_k + \boldsymbol{B}_u^T \boldsymbol{X} \\ sym & \boldsymbol{B}_w^T \boldsymbol{C} \boldsymbol{B}_w + \boldsymbol{B}_{Gw} & \boldsymbol{B}_w^T \boldsymbol{C} \boldsymbol{B}_k + \boldsymbol{B}_w^T \boldsymbol{X} \\ sym & sym & \boldsymbol{B}_k^T \boldsymbol{C} \boldsymbol{B}_k + \boldsymbol{X}^T \boldsymbol{B}_k + \boldsymbol{B}_k^T \boldsymbol{X} + \boldsymbol{D} + \boldsymbol{B}_{Gk} \end{bmatrix} \tag{3.34}$$

in which $\boldsymbol{B}_{Gw}$ and $\boldsymbol{B}_{Gk}$ represent the geometric part of the stiffness matrix. It can be observed that when $\boldsymbol{X}$ is equal to a null matrix, the matrices and vectors derived from Equation (3.26) are similar to the elastic ones derived by Providas (1990) and Morley (1991).

URN:NBN:no-1282

Chapter 4

Curved Element with Large Rotations

4.1 Introduction

In Chapter 3, elasto–plastic formulation of the constant stress shell element which is valid for moderate rotations has been presented. The element is based on quadratic polynomials for both in–plane and out–of–plane displacements, and it was derived using non–orthogonal coordinate system. The aim of the present chapter is to obtain an element of a similar type that can perform well in problems undergoing arbitrary large displacements and rotations. Indeed, Bout (1993) has already described a similar displacement–based geometrically nonlinear element by using Cartesian coordinates.

For the membrane displacements, the element by Bout (1993) assumes linear shape functions for displacements. The nonlinear strain and changes of curvatures are based on Green–Lagrange equations. To accommodate arbitrary large rotations, a co–rotational formulation is invoked for the bending behavior only. The method was proposed by Besseling (1980) and Ernst (1981), and it is restricted to moderate rotational increments (Section 2.4.1). The main idea is that the outward unit–normal to the element flat surface is rotated at the end of each increment. A mixed formulation resulting in a similar element has been given by van Keulen (1993).

The discrete equations derived by Bout (1993) provide constant tangent stiffness throughout an increment. In other words, a solution by standard Newton–Raphson procedure, by using these equations, would not have any advantage since it would be similar to using its modified version. The derivations involve the splitting of displacements and curvature changes. The split is between the next unknown incremental quantities and the current known total quantities. In the final equations, the incremental quantities are neglected leading to constant tangent stiffness. The consequence of constant tangent stiffness is a slower convergence.

URN:NBN:no-1282

In the present chapter the discrete equations are re–derived. The resulting equations lead to a variable tangent stiffness matrix within an increment. The equations are not only neater but the residual converges faster with standard Newton–Raphson solution procedures. A similar approach has been used by van Keulen (1993) for an element based on mixed formulation. Before the present derivation, the starting point is to revisit the work of Bout (1993) and apply the fundamental ideas of his displacement–based geometrically nonlinear element.

4.2 Basic Equations and Definitions

The geometry and degrees of freedom of the facet triangular shell element are shown in Figure 4.1. The spatial quantities are described in Cartesian coordinate system, while the displacement functions are described by triangular area coordinates. In addition, a local in–plane Cartesian coordinate system (x', y'), with its origin at the mid-side, is defined for each element side. The element has twelve degrees of freedom, namely three displacements at each vertex, and one rotation at each mid–side.

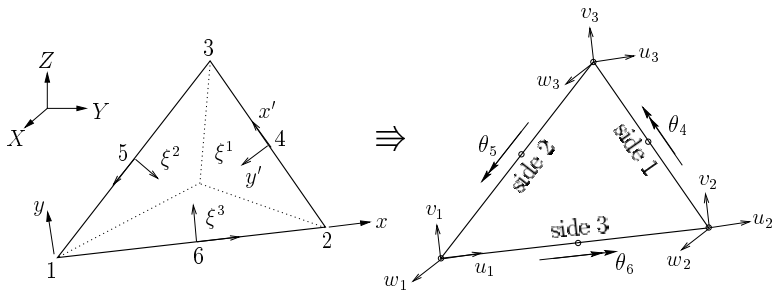

Figure 4.1 Element geometry and degrees of freedom.

In the undeformed configuration, the flat surface is described by a position vector in terms of its Cartesian coordinates p_i with respect to the base vectors $\boldsymbol{e}_i$ (see Figure 4.2). This surface may differ slightly from the shell surface defined by a small curvature.

For the coming sections, a representation of the strain tensor $\boldsymbol{\gamma}$ by its components with respect to the element side directions is needed. It is convenient to establish a relation between these components and the conventional Cartesian components at this point. Similar to van Keulen (1993), first the side directions are defined by vectors such that,

$$\boldsymbol{s}_i = a_i \boldsymbol{e}_1 - b_i \boldsymbol{e}_2 \tag{4.1}$$

where a_i and b_i are given by vertex coordinates as defined in Equation (2.11). Then, the membrane strain corresponding to direction $\boldsymbol{s}_i$ is given by,

$$\bar{\gamma}_i = \frac{1}{l_i^2} \left(\boldsymbol{s}_i^T \boldsymbol{\gamma} \boldsymbol{s}_i \right) \tag{4.2}$$

URN:NBN:no-1282

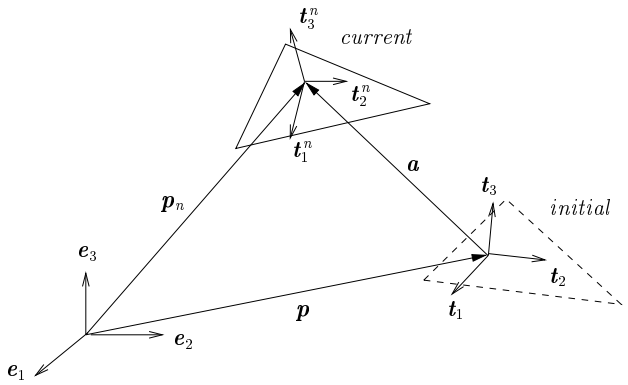

Figure 4.2 Element kinematics and unit base vectors.

where l_i is the length of side i, and $\boldsymbol{\gamma}$ is the strain tensor with respect to the conventional Cartesian coordinates. The latter is defined as,

$$\boldsymbol{\gamma}^T = [\gamma_{11} \quad \gamma_{22} \quad 2\gamma_{12}] = [\gamma_1 \quad \gamma_2 \quad \gamma_3] \tag{4.3}$$

Finally, in virtue of Equations (4.1), (4.2), and (4.3), the relation between the two representations of the strain tensor may be written as,

$$\gamma_i = \bar{T}_{ij}\bar{\gamma}_j \tag{4.4}$$

where the elements of the transformation matrix are obtained as,

$$\bar{\boldsymbol{T}} = -\frac{1}{4A^2}\begin{bmatrix} l_1^2 b_2 b_3 & l_2^2 b_3 b_1 & l_3^2 b_1 b_2 \\ l_1^2 a_2 a_3 & l_2^2 a_3 a_1 & l_3^2 a_1 a_2 \\ l_1^2(b_2 a_3 + a_2 b_3) & l_2^2(b_3 a_1 + a_3 b_1) & l_3^2(b_1 a_2 + a_1 b_2) \end{bmatrix} \tag{4.5}$$

4.2.1 Local—Global Transformation Matrix

With reference to Figure 4.2, the transformation matrix $\boldsymbol{T}$ between the element local degrees of freedom $\boldsymbol{r}$ and the corresponding global ones $\boldsymbol{r}_g$ may be expressed as,

$$\boldsymbol{r} = \boldsymbol{T}\boldsymbol{r}_g \quad \Longleftrightarrow \quad \boldsymbol{r}_g = \boldsymbol{T}^T\boldsymbol{r} \tag{4.6}$$

where,

$$\boldsymbol{T} = diag[\boldsymbol{E} \quad \boldsymbol{E} \quad \boldsymbol{E} \quad \boldsymbol{I}_3] \qquad \boldsymbol{E}^T = \begin{bmatrix} \boldsymbol{e}_1^T & \boldsymbol{e}_2^T & \boldsymbol{e}_3^T \end{bmatrix} \tag{4.7}$$

The order of the degrees of freedom for the transformation matrix is as referred in Figure 4.1 starting from node number 1 to 6, consecutively.

It is important to note that, the elements of the identity matrix $\boldsymbol{I}_3$ are to be multiplied with appropriate sign convention for side rotations, so as to obtain a smooth formulation. For the remaining sections, the base vectors $\boldsymbol{e}_i$ will be selected such that $\boldsymbol{e}_1$ coincides with the element side 3, with the head at element node 2 and the tail at node 1.

URN:NBN:no-1282

4.2.2 Governing Equations

Nonlinear deformation quantities for thin plates are reviewed in this section. A restriction is imposed to cases in which the Kirchhoff–Love assumptions are admissible. Therefore, the entire strain state can be described by the middle surface strain tensor and the tensor of curvature changes.

Displacement field

The in–plane displacements are assumed to vary linearly over the element, while the transverse displacement varies quadratically such that,

$$u = u_1\xi^1 + u_2\xi^2 + u_3\xi^3 \tag{4.8}$$
$$v = v_1\xi^1 + v_2\xi^2 + v_3\xi^3 \tag{4.9}$$
$$w = w_1\xi^1 + w_2\xi^2 + w_3\xi^3 + \psi_4\xi^2\xi^3 + \psi_5\xi^3\xi^1 + \psi_6\xi^1\xi^2 \tag{4.10}$$

in which the subscripts indicate the vertex number, and u, v, and w denote the in–plane displacements along the x and y–axes, and out–of–plane displacements, respectively.

The coefficients ψ_{i+3} can be regarded as a measure of deflections of the mid–sides. They were introduced in Section 3.2.1 and illustrated in Figure 3.2. The coefficients are associated with an incompatible mode. By incompatible mode, it is implied that along a common side of two planar adjacent elements, the out–of–plane displacement Equation (4.10) does not satisfy the slope continuity except only at the interconnection point in the middle of the side.

The initial deflection or curvature may be added directly to these incompatible mode components as will be shown in the coming sections. It is in this way that the present element can be considered curved. The incompatible coefficients are determined from three equations (one for each side of the triangle) for rotations along the sides as,

$$\theta_{i+3} = \phi_{y'(i+3)} = w_{,y'} \qquad (x' = y' = 0)|_{i+3} \tag{4.11}$$

To evaluate Equation (4.11), it is convenient to take the derivatives with respect to non–orthogonal coordinates and sum up the components in the local side coordinates. Accordingly, we can write

$$\begin{aligned}
\theta_4 = \phi_{y'4} &= +\frac{l_1}{2A}w_{,\xi^1} - \frac{l_{12}}{2Al_1}w_{,\xi^2} && (\xi^1 = 0,\ \xi^2 = \xi^3 = \frac{1}{2}) \\
\theta_5 = \phi_{y'5} &= -\frac{l_{12}}{2Al_2}w_{,\xi^1} + \frac{l_2}{2A}w_{,\xi^2} && (\xi^2 = 0,\ \xi^3 = \xi^1 = \frac{1}{2}) \\
\theta_6 = \phi_{y'6} &= -\frac{l_{31}}{4Al_3}w_{,\xi^1} - \frac{l_{23}}{4Al_3}w_{,\xi^2} && (\xi^2 = 0,\ \xi^3 = \xi^1 = \frac{1}{2})
\end{aligned} \tag{4.12}$$

Then, substituting the assumed displacement field Equation (4.10) into (4.12) and carrying

URN:NBN:no-1282

out the necessary derivatives yields,

$$\psi_4 = \frac{1}{2}\left\{\left(\frac{l_{12}}{l_2^2}+\frac{l_{31}}{l_3^2}\right)w_1 - \frac{l_{31}}{l_3^2}w_2 - \frac{l_{12}}{l_2^2}w_3 + \frac{4A}{l_2}\theta_5 + \frac{4A}{l_3}\theta_6\right\} \tag{4.13}$$

$$\psi_5 = \frac{1}{2}\left\{-\frac{l_{23}}{l_3^2}w_1 + \left(\frac{l_{12}}{l_1^2}+\frac{l_{23}}{l_3^2}\right)w_2 - \frac{l_{12}}{l_1^2}w_3 + \frac{4A}{l_1}\theta_4 + \frac{4A}{l_3}\theta_6\right\} \tag{4.14}$$

$$\psi_6 = \frac{1}{2}\left\{-\frac{l_{23}}{l_2^2}w_1 - \frac{l_{31}}{l_1^2}w_2 + \left(\frac{l_{31}}{l_1^2}+\frac{l_{23}}{l_2^2}\right)w_3 + \frac{4A}{l_1}\theta_4 + \frac{4A}{l_2}\theta_5\right\} \tag{4.15}$$

where l_{12}, l_{23}, and l_{31} are constant quantities defined in Equations (2.16)–(2.18).

Strain—displacement relations

The middle surface strain tensor and the tensor of curvature changes is expressed in terms of displacement components as,

$$\gamma_{\alpha\beta} = \frac{1}{2}\left(u_{\alpha,\beta} + u_{\beta,\alpha} + u_{\lambda,\alpha}u_{\lambda,\beta} + w_{,\alpha}w_{,\beta}\right) \tag{4.16}$$

$$\chi_{\alpha\beta} = w_{,\alpha\beta} \tag{4.17}$$

where u_α ($u_1 = u$, $u_2 = v$) and w are the in–plane and out–of–plane displacement components, respectively. Note that, when the third term is equal to zero Equation (4.16) becomes identical to the von Kármán Equation (3.5).

While Equation (4.16) is valid for arbitrary rotations, Equation (4.17) remains valid only when the rotations remain moderate. The curvature changes are modified in the coming sections so that the expressions are extended to accommodate arbitrary large rotations.

4.2.3 Elasticity Modular Matrix

Contrary to Equation (3.21), the isotropic elastic modular matrix for the present element is the conventional one which is given by,

$$\mathbb{C} = \frac{E}{1-\nu^2}\begin{bmatrix} 1 & \nu & 0 \\ \nu & 1 & 0 \\ 0 & 0 & \frac{1}{2}(1-\nu) \end{bmatrix} \tag{4.18}$$

where E is the Young's modulus, ν is the Poisson's ratio, and t is the plate thickness.

In virtue of Equation (4.18), the stress resultants tensor (forces $\boldsymbol{N}$ and moments $\boldsymbol{M}$), the membrane strain tensor $\boldsymbol{\gamma}$, and the tensor of curvature changes $\boldsymbol{\chi}$, are given by,

$$\begin{array}{ll} \boldsymbol{N}^T = [N_{11} \quad N_{22} \quad N_{12}] & \boldsymbol{M}^T = [M_{11} \quad M_{22} \quad M_{12}] \\ \boldsymbol{\gamma}^T = [\gamma_{11} \quad \gamma_{22} \quad 2\gamma_{12}] & \boldsymbol{\chi}^T = [\chi_{11} \quad \chi_{22} \quad 2\chi_{12}] \end{array} \tag{4.19}$$

URN:NBN:no-1282

4.3 Finite Element Formulation

Let the local element displacement vector $\boldsymbol{r}$, be represented as,

$$\boldsymbol{r}^T = \begin{bmatrix} \boldsymbol{a}^T & \boldsymbol{\varphi}^T \end{bmatrix} = \begin{bmatrix} \boldsymbol{u}^T & \boldsymbol{v}^T & \boldsymbol{w}^T & \boldsymbol{\varphi}^T \end{bmatrix} \tag{4.20}$$

where $\boldsymbol{u}$, $\boldsymbol{v}$, $\boldsymbol{w}$, and $\boldsymbol{\varphi}$ denote the membrane displacements along the x and y–axes, out–of–plane displacements, and mid–side rotations, respectively

$$\begin{aligned} \boldsymbol{u}^T &= [u_1 \quad u_2 \quad u_3] & \boldsymbol{v}^T &= [v_1 \quad v_2 \quad v_3] \\ \boldsymbol{w}^T &= [w_1 \quad w_2 \quad w_3] & \boldsymbol{\varphi}^T &= [\theta_4 \quad \theta_5 \quad \theta_6] \end{aligned} \tag{4.21}$$

Note the difference between this arrangement of the degrees of freedom and the one for $\boldsymbol{T}$ in Equation (4.7). With the present definitions, Equations (4.13)–(4.15) may be expressed in matrix form as,

$$\boldsymbol{\psi} = \boldsymbol{E}_w \boldsymbol{w} + \boldsymbol{E}_\varphi \boldsymbol{\varphi} \tag{4.22}$$

where,

$$\boldsymbol{E}_w = \frac{1}{2} \begin{bmatrix} l_{12}/l_2^2 + l_{31}/l_3^2 & -l_{31}/l_3^2 & -l_{12}/l_2^2 \\ -l_{23}/l_3^2 & l_{12}/l_1^2 + l_{23}/l_3^2 & -l_{12}/l_1^2 \\ -l_{23}/l_2^2 & -l_{31}/l_1^2 & l_{31}/l_1^2 + l_{23}/l_2^2 \end{bmatrix} \tag{4.23}$$

$$\boldsymbol{E}_\varphi = \begin{bmatrix} 0 & 2A/l_2 & 2A/l_3 \\ 2A/l_1 & 0 & 2A/l_3 \\ 2A/l_1 & 2A/l_2 & 0 \end{bmatrix} \tag{4.24}$$

4.3.1 Large Displacements with Moderate Rotations

It has been demonstrated by Bout (1993) that as long as the membrane strain components remain constant over the triangle, it does not make any difference whether they are determined by a straightforward evaluation of Equation (4.16) or by transforming the strains of the sides to the Cartesian components by Equation (4.5). The quadratic terms in Equation (4.10), however, result in non–constant membrane strains. To obtain constant membrane strain components in this case, average values resulting from these terms will be calculated as by Bout (1993). In that publication, it was shown that the additional strain of a particular side due to the quadratic terms is determined only by ψ_{i+3}.

Based on the above discussion, it is convenient to suppress the quadratic terms initially and determine the membrane strains in a straightforward manner. As a result, substitution of Equations (4.8)–(4.10) into (4.16), when the quadratic terms are suppressed, yields

$$\boldsymbol{\gamma} = \left(\boldsymbol{B}_{a1} + \tfrac{1}{2} \boldsymbol{B}_{a2} \right) \boldsymbol{a} \tag{4.25}$$

URN:NBN:no-1282

where the strain–displacement matrices are given by,

$$\boldsymbol{B}_{a1} = \begin{bmatrix} \boldsymbol{d}_1^T & \boldsymbol{0} & \boldsymbol{0} \\ \boldsymbol{0} & \boldsymbol{d}_2^T & \boldsymbol{0} \\ \boldsymbol{d}_2^T & \boldsymbol{d}_1^T & \boldsymbol{0} \end{bmatrix} \qquad \boldsymbol{B}_{a2} = \begin{bmatrix} \boldsymbol{u}^T\boldsymbol{c}_1 & \boldsymbol{v}^T\boldsymbol{c}_1 & \boldsymbol{w}^T\boldsymbol{c}_1 \\ \boldsymbol{u}^T\boldsymbol{c}_2 & \boldsymbol{v}^T\boldsymbol{c}_2 & \boldsymbol{w}^T\boldsymbol{c}_2 \\ \boldsymbol{u}^T\boldsymbol{c}_3 & \boldsymbol{v}^T\boldsymbol{c}_3 & \boldsymbol{w}^T\boldsymbol{c}_3 \end{bmatrix} \tag{4.26}$$

in which the following definitions have been made,

$$\boldsymbol{d}_1^T = \frac{1}{2A}\,[b_1 \;\; b_2 \;\; b_3] \qquad \boldsymbol{d}_2^T = \frac{1}{2A}\,[a_1 \;\; a_2 \;\; a_3] \tag{4.27}$$

$$\boldsymbol{c}_1 = \boldsymbol{d}_1\boldsymbol{d}_1^T \qquad \boldsymbol{c}_2 = \boldsymbol{d}_2\boldsymbol{d}_2^T \qquad \boldsymbol{c}_3 = \boldsymbol{d}_1\boldsymbol{d}_2^T + \boldsymbol{d}_2\boldsymbol{d}_1^T \tag{4.28}$$

It is important to point out that the direct expression for $\boldsymbol{c}_3$ in Equation (4.25) is given by $2\,\boldsymbol{d}_1\boldsymbol{d}_2^T$. However, this expression presents difficulties and leads to asymmetry in the tangent stiffness matrix. In the present derivation, $\boldsymbol{c}_3$ is symmetrized to avoid this problem. This is the central part in order to achieve the required re–derivation. It is interesting that, though they are not numerically identical, the two expressions lead to identical strains. This has been checked analytically with Equation (4.25) by using the two alternatives.

The additional strains to Equation (4.25), which are due to the quadratic terms, are obtained as average values. These are first calculated along the side directions and then transformed to the conventional Cartesian components by using Equation (4.5). In the direction of side i, the average value of the membrane strain follows from,

$$\bar{\gamma}^{av}_{1'1'} = \frac{1}{l_i}\int_{-\frac{1}{2}l_i}^{\frac{1}{2}l_i} \bar{\gamma}_{1'1'}\,dx'|_i \tag{4.29}$$

where,

$$\bar{\gamma}_{1'1'}|_i = u_{,1'}|_i + \frac{1}{2}\left(u_{,1'}^2 + v_{,1'}^2 + w_{,1'}^2\right)|_i \tag{4.30}$$

Substitution of Equations (4.8)–(4.10) and (4.30) into (4.29) yields,

$$\bar{\boldsymbol{\gamma}}^{av} = \left(\boldsymbol{B}'_{a1} + \tfrac{1}{2}\boldsymbol{B}'_{a2}\right)\boldsymbol{a} + \tfrac{1}{2}\boldsymbol{B}'_{\psi}\boldsymbol{\psi} \tag{4.31}$$

where,

$$\boldsymbol{B}'_{\psi} = \frac{1}{3}\begin{bmatrix} \psi_4/l_1^2 & 0 & 0 \\ 0 & \psi_5/l_2^2 & 0 \\ 0 & 0 & \psi_6/l_3^2 \end{bmatrix} \tag{4.32}$$

$$\boldsymbol{B}'_{a1} = \bar{\boldsymbol{T}}^{-1}\boldsymbol{B}_{a1} \qquad \boldsymbol{B}'_{a2} = \bar{\boldsymbol{T}}^{-1}\boldsymbol{B}_{a2} \tag{4.33}$$

URN:NBN:no-1282

The additional term of the membrane strain is now obvious from Equation (4.31) as compared to Equation (4.25). This term can be transformed in line with Equations (4.4) and (4.5) to obtain the membrane strain in terms of Cartesian components as,

$$\boldsymbol{\gamma}^{add} = \tfrac{1}{2}\,\bar{\boldsymbol{T}}\boldsymbol{B}'_{\psi}\boldsymbol{\psi} = \tfrac{1}{2}\boldsymbol{B}_{\psi}\boldsymbol{\psi} \tag{4.34}$$

At this point, it is convenient to introduce the initial curvature into Equation (4.34) and then add the resulting expression into Equation (4.25). Accordingly, by noting that the initial curvature is a known quantity, the total constant membrane strain tensor may be expressed as,

$$\boldsymbol{\gamma} = \left(\boldsymbol{B}_{a1} + \tfrac{1}{2}\boldsymbol{B}_{a2}\right)\boldsymbol{a} + \left(\boldsymbol{B}_{\psi_\circ} + \tfrac{1}{2}\boldsymbol{B}_{\psi_d}\right)\boldsymbol{\psi} \tag{4.35}$$

in which the subscripts $\psi_\circ$ and ψ_d stand for the initial and deformational curvatures, respectively, for which

$$\boldsymbol{B}_{\psi_\circ} = \boldsymbol{B}(\psi_\circ) \qquad\qquad \boldsymbol{B}_{\psi_d} = \boldsymbol{B}(\psi_d) \tag{4.36}$$

where the strain–displacement matrix, holding for both $\psi_\circ$ and ψ_d, is given by

$$\boldsymbol{B}(\psi) = -\frac{1}{12A^2}\begin{bmatrix} b_2b_3\psi_4 & b_3b_1\psi_5 & b_1b_2\psi_6 \\ a_2a_3\psi_4 & a_3a_1\psi_5 & a_1a_2\psi_6 \\ (b_2a_3+a_2b_3)\psi_4 & (b_3a_1+a_3b_1)\psi_5 & (b_1a_2+a_1b_2)\psi_6 \end{bmatrix} \tag{4.37}$$

As for curvature changes, substitution of Equation (4.10) into (4.17) yields,

$$\boldsymbol{\chi} = \boldsymbol{B}_w\boldsymbol{w} + \boldsymbol{B}_\varphi\boldsymbol{\varphi} \tag{4.38}$$

where,

$$\boldsymbol{B}_w = \boldsymbol{J}\boldsymbol{E}_w \qquad\qquad \boldsymbol{B}_\varphi = \boldsymbol{J}\boldsymbol{E}_\varphi \tag{4.39}$$

$$\boldsymbol{J} = \frac{1}{2A^2}\begin{bmatrix} b_2b_3 & b_3b_1 & b_1b_2 \\ a_2a_3 & a_3a_1 & a_1a_2 \\ b_2a_3+a_2b_3 & b_3a_1+a_3b_1 & b_1a_2+a_1b_2 \end{bmatrix} \tag{4.40}$$

4.3.2 Arbitrary Large Displacements and Rotations

As mentioned in section 4.2.2, Equation (4.17) and hence (4.38) are only valid within moderate rotations. The membrane Equations (4.16) and (4.35), however, are applicable within large rotations. Therefore, to accommodate large rotations for bending, it may serve the purpose to employ an updating technique to curvature changes only.

Aiming for incremental curvature changes, the current unit–normal vector $\boldsymbol{t}_3^n$ in Figure 4.2 is rotated such that it coincides with the instantaneously fixed co–rotating reference configuration as in Bout (1993) and van Keulen (1993). This reference state is obtained by

URN:NBN:no-1282

submitting the initial geometry to the rigid body motions, governed by the displacements of the vertices, with a restriction that the element deformations (strains) remain small. In other words, the vertices of the instantaneously co–rotated configuration are assumed to coincide with the deformed configuration.

Considering only the facet geometry of the triangle, the reference vectors in the current configuration are related to the initial configuration by the expression,

$$[\boldsymbol{t}_1^n \quad \boldsymbol{t}_2^n \quad \boldsymbol{t}_3^n]^T = [\boldsymbol{R}]\,[\boldsymbol{t}_1 \quad \boldsymbol{t}_2 \quad \boldsymbol{t}_3]^T \tag{4.41}$$

where $\boldsymbol{R}$ is the rotation tensor. Since we need to update only the unit normal vector, the following transformation equation serves the purpose,

$$\boldsymbol{t}_3^n = [R_{31} \quad R_{32} \quad R_{33}]\,[\boldsymbol{t}_1 \quad \boldsymbol{t}_2 \quad \boldsymbol{t}_3]^T \tag{4.42}$$

where the components of the rotation tensor may be expressed as, (see Ernst (1981))

$$\begin{bmatrix} R_{31} \\ R_{32} \\ R_{33} \end{bmatrix} = \begin{bmatrix} -\boldsymbol{d}_1^T\boldsymbol{w} + \boldsymbol{d}_2^T\boldsymbol{w}\boldsymbol{d}_1^T\boldsymbol{v} - \boldsymbol{d}_1^T\boldsymbol{w}\boldsymbol{d}_2^T\boldsymbol{v} \\ -\boldsymbol{d}_2^T\boldsymbol{w} + \boldsymbol{d}_1^T\boldsymbol{w}\boldsymbol{d}_2^T\boldsymbol{v} - \boldsymbol{d}_2^T\boldsymbol{w}\boldsymbol{d}_1^T\boldsymbol{v} \\ 1 + \boldsymbol{d}_1^T\boldsymbol{u} + \boldsymbol{d}_2^T\boldsymbol{v} + \boldsymbol{d}_1^T\boldsymbol{u}\boldsymbol{d}_2^T\boldsymbol{v} - \boldsymbol{d}_1^T\boldsymbol{v}\boldsymbol{d}_2^T\boldsymbol{u} \end{bmatrix} \tag{4.43}$$

With respect to the instantaneously co–rotated configuration, relative displacements and rotations are introduced as a difference between the deformed and co–rotated reference states. As a result, an expression similar to Equation (4.38) can be found as,

$$\hat{\boldsymbol{\chi}} = \boldsymbol{B}_w\hat{\boldsymbol{w}} + \boldsymbol{B}_\varphi\hat{\boldsymbol{\varphi}} \tag{4.44}$$

where $\hat{\boldsymbol{w}}$ and $\hat{\boldsymbol{\varphi}}$ denote the relative transverse displacements and relative rotations. This expression may be extended into the regime of finite rotation while strains remain small. In this case, the rate equation for the discrete curvature changes may be expressed as, (see Bout (1993) van Keulen (1993))

$$\dot{\boldsymbol{\chi}} = \boldsymbol{B}_w\dot{\boldsymbol{w}}_v + \boldsymbol{B}_\varphi\dot{\boldsymbol{\varphi}} \tag{4.45}$$

where the superposed dot indicates the derivative with respect to a time–like parameter. The component vector $\dot{\boldsymbol{w}}_v$ contains the nodal velocities perpendicular to the instantaneously fixed co–rotating configuration. With reference to Equation (4.42), (4.45) may be expressed as,

$$\dot{\boldsymbol{\chi}} = \boldsymbol{B}_w\,(R_{31}\dot{\boldsymbol{u}} + R_{32}\dot{\boldsymbol{v}} + R_{33}\dot{\boldsymbol{w}}) + \boldsymbol{B}_\varphi\dot{\boldsymbol{\varphi}} \tag{4.46}$$

and similarly, for the out–of–plane coefficients, Equation (4.22) may be updated to,

$$\dot{\boldsymbol{\psi}} = \boldsymbol{E}_w\,(R_{31}\dot{\boldsymbol{u}} + R_{32}\dot{\boldsymbol{v}} + R_{33}\dot{\boldsymbol{w}}) + \boldsymbol{E}_\varphi\dot{\boldsymbol{\varphi}} \tag{4.47}$$

Because of the rate Equations (4.46) and (4.47), the actual changes of curvature need to be evaluated by a step–by–step integration. However, by realizing that the nonlinear equilibrium equations are solved incrementally, the above rate equations may be taken

URN:NBN:no-1282

for a *unit* time–like parameter so that for an *arbitrary incremental step*, the strains and curvature changes can be expressed as,

$$\boldsymbol{\gamma} = \left(\boldsymbol{B}_{a1} + \tfrac{1}{2}\boldsymbol{B}_{a2} + \left[\boldsymbol{B}_{\psi_\circ} + \tfrac{1}{2}\boldsymbol{B}_{\psi_d}\right]\boldsymbol{E}_{\bar{w}}\right)\boldsymbol{a} + \left[\boldsymbol{B}_{\psi_\circ} + \tfrac{1}{2}\boldsymbol{B}_{\psi_d}\right]\boldsymbol{E}_{\varphi}\boldsymbol{\varphi} \tag{4.48}$$

$$\boldsymbol{\chi} = \boldsymbol{B}_w\left(R_{31}\boldsymbol{u} + R_{32}\boldsymbol{v} + R_{33}\boldsymbol{w}\right) + \boldsymbol{B}_{\varphi}\boldsymbol{\varphi} = \boldsymbol{B}_{\bar{w}}\boldsymbol{a} + \boldsymbol{B}_{\varphi}\boldsymbol{\varphi} \tag{4.49}$$

where,

$$\boldsymbol{E}_{\bar{w}} = \begin{bmatrix} R_{31}\boldsymbol{E}_w & R_{32}\boldsymbol{E}_w & R_{33}\boldsymbol{E}_w \end{bmatrix} \tag{4.50}$$

$$\boldsymbol{B}_{\bar{w}} = \begin{bmatrix} R_{31}\boldsymbol{B}_w & R_{32}\boldsymbol{B}_w & R_{33}\boldsymbol{B}_w \end{bmatrix} \tag{4.51}$$

The discrete equations of equilibrium can now be derived using Equations (4.48) and (4.49) with a pre–condition. The requirement is that the total curvature changes are obtained in incremental–update manner. At the end of each increment $n+1$, the following expressions must be applied,

$$\boldsymbol{\psi}^{n+1} = \boldsymbol{\psi}^{n} + \boldsymbol{E}_w\left[R_{31}^n\Delta\boldsymbol{u}^{n+1} + R_{32}^n\Delta\boldsymbol{v}^{n+1} + R_{33}^n\Delta\boldsymbol{w}^{n+1}\right] + \boldsymbol{E}_{\varphi}\Delta\boldsymbol{\varphi}^{n+1} \tag{4.52}$$

$$\boldsymbol{\gamma}^{n+1} = \left(\boldsymbol{B}_{a1} + \tfrac{1}{2}\boldsymbol{B}_{a2}^{n+1}\right)\boldsymbol{a}^{n+1} + \left(\boldsymbol{B}_{\psi_\circ} + \tfrac{1}{2}\boldsymbol{B}_{\psi_d}^{n+1}\right)\boldsymbol{\psi}^{n+1} \tag{4.53}$$

$$\boldsymbol{\chi}^{n+1} = \boldsymbol{\chi}^{n} + \boldsymbol{B}_w\left[R_{31}^n\Delta\boldsymbol{u}^{n+1} + R_{32}^n\Delta\boldsymbol{v}^{n+1} + R_{33}^n\Delta\boldsymbol{w}^{n+1}\right] + \boldsymbol{B}_{\varphi}\Delta\boldsymbol{\varphi}^{n+1} \tag{4.54}$$

Then, for an arbitrary incremental step, the first variation of the strain tensor is given by,

$$\begin{aligned}\delta\boldsymbol{\gamma} &= \left(\boldsymbol{B}_{a1} + \boldsymbol{B}_{a2} + \left[\boldsymbol{B}_{\psi_\circ} + \boldsymbol{B}_{\psi_d}\right]\boldsymbol{E}_{\bar{w}}\right)\delta\boldsymbol{a} + \left[\boldsymbol{B}_{\psi_\circ} + \boldsymbol{B}_{\psi_d}\right]\boldsymbol{E}_{\varphi}\delta\boldsymbol{\varphi} \\ &= \left(\boldsymbol{B}_{a} + \boldsymbol{B}_{\bar{\psi}}\boldsymbol{E}_{\bar{w}}\right)\delta\boldsymbol{a} + \boldsymbol{B}_{\bar{\psi}}\boldsymbol{E}_{\varphi}\delta\boldsymbol{\varphi}\end{aligned} \tag{4.55}$$

$$\delta\boldsymbol{\chi} = \boldsymbol{B}_{\bar{w}}\delta\boldsymbol{a} + \boldsymbol{B}_{\varphi}\delta\boldsymbol{\varphi} \tag{4.56}$$

where,

$$\boldsymbol{B}_a = \boldsymbol{B}_{a1} + \boldsymbol{B}_{a2} \qquad\qquad \boldsymbol{B}_{\bar{\psi}} = \boldsymbol{B}_{\psi_\circ} + \boldsymbol{B}_{\psi_d} \tag{4.57}$$

Alternatively, we can write,

$$\delta\bar{\boldsymbol{\epsilon}} = \begin{Bmatrix}\delta\boldsymbol{\gamma} \\ \delta\boldsymbol{\chi}\end{Bmatrix} = \begin{bmatrix}\boldsymbol{B}_a + \boldsymbol{B}_{\bar{\psi}}\boldsymbol{E}_{\bar{w}} & \boldsymbol{B}_{\bar{\psi}}\boldsymbol{E}_{\varphi} \\ \boldsymbol{B}_{\bar{w}} & \boldsymbol{B}_{\varphi}\end{bmatrix}\begin{Bmatrix}\delta\boldsymbol{a} \\ \delta\boldsymbol{\varphi}\end{Bmatrix} = \boldsymbol{B}\delta\boldsymbol{r} \tag{4.58}$$

where $\boldsymbol{B}$ is the nonlinear strain–displacement matrix,

$$\boldsymbol{B} = \begin{bmatrix}\boldsymbol{B}_a + \boldsymbol{B}_{\bar{\psi}}\boldsymbol{E}_{\bar{w}} & \boldsymbol{B}_{\bar{\psi}}\boldsymbol{E}_{\varphi} \\ \boldsymbol{B}_{\bar{w}} & \boldsymbol{B}_{\varphi}\end{bmatrix} \tag{4.59}$$

The second variation of Equation (4.58) is given by,

$$\delta^2\bar{\boldsymbol{\epsilon}} = \begin{Bmatrix}\delta^2\boldsymbol{\gamma} \\ \delta^2\boldsymbol{\chi}\end{Bmatrix} = \begin{bmatrix}\delta\boldsymbol{B}_a + \delta\boldsymbol{B}_{\bar{\psi}}\boldsymbol{E}_{\bar{w}} & \delta\boldsymbol{B}_{\bar{\psi}}\boldsymbol{E}_{\varphi} \\ \boldsymbol{0} & \boldsymbol{0}\end{bmatrix}\begin{Bmatrix}\delta\boldsymbol{a} \\ \delta\boldsymbol{\varphi}\end{Bmatrix} \tag{4.60}$$

URN:NBN:no-1282

4.3.3 Discrete Equilibrium Equations

The equations of equilibrium are derived from the principle of virtual work. The element internal virtual work equation is given by the left hand side of Equation (2.1). For constant stresses and strain, it can be expressed as,

$$\delta W^i = A\ \delta\bar{\boldsymbol{\epsilon}}^T\bar{\boldsymbol{\sigma}} \tag{4.61}$$

where,

$$\bar{\boldsymbol{\epsilon}}^T = \begin{bmatrix}\boldsymbol{\gamma}^T & \boldsymbol{\chi}^T\end{bmatrix} \qquad \bar{\boldsymbol{\sigma}}^T = \begin{bmatrix}\boldsymbol{N}^T & \boldsymbol{M}^T\end{bmatrix} \tag{4.62}$$

Substituting Equation (4.58) into (4.61) yields,

$$\delta W^i = A\ \delta\boldsymbol{r}^T\boldsymbol{B}^T\bar{\boldsymbol{\sigma}} = \delta\boldsymbol{r}^T\boldsymbol{f} \tag{4.63}$$

from which the element *internal force vector* in terms of nodal forces follows as,

$$\boldsymbol{f} = A\ \boldsymbol{B}^T\bar{\boldsymbol{\sigma}} \tag{4.64}$$

The variation of the internal virtual work (Equation (4.61)) is given by,

$$\begin{aligned}\delta^2 W^i &= A\left(\delta\bar{\boldsymbol{\epsilon}}^T\delta\bar{\boldsymbol{\sigma}} + \delta^2\bar{\boldsymbol{\epsilon}}^T\bar{\boldsymbol{\sigma}}\right)\\ &= A\left(\delta\boldsymbol{r}^T\boldsymbol{B}^T\bar{\mathbb{C}}_t\,\boldsymbol{B}\delta\boldsymbol{r} + \begin{Bmatrix}\delta\boldsymbol{a}^T & \delta\boldsymbol{\varphi}^T\end{Bmatrix}\begin{bmatrix}\delta\boldsymbol{B}_a^T + \boldsymbol{E}_{\bar{w}}^T\delta\boldsymbol{B}_{\bar{\psi}}^T & \boldsymbol{0}\\ \boldsymbol{E}_{\varphi}^T\delta\boldsymbol{B}_{\bar{\psi}}^T & \boldsymbol{0}\end{bmatrix}\begin{Bmatrix}\boldsymbol{N}\\ \boldsymbol{M}\end{Bmatrix}\right)\end{aligned} \tag{4.65}$$

Before deriving the element *tangent stiffness matrix* from Equation (4.65), we recognize the following relations for the geometric versions of the strain–displacement matrices,

$$\delta\boldsymbol{B}_a^T\boldsymbol{N} = \boldsymbol{B}_{Ga}\delta\boldsymbol{a} \tag{4.66}$$

$$\delta\boldsymbol{B}_{\bar{\psi}}^T\boldsymbol{N} = \boldsymbol{B}_{G\psi}\delta\boldsymbol{\psi} = \begin{bmatrix}\boldsymbol{B}_{G\psi}\end{bmatrix}\begin{bmatrix}\boldsymbol{E}_{\bar{w}} & \boldsymbol{E}_{\varphi}\end{bmatrix}\begin{Bmatrix}\delta\boldsymbol{a}\\ \delta\boldsymbol{\varphi}\end{Bmatrix} \tag{4.67}$$

with,

$$\boldsymbol{B}_{Ga} = \begin{bmatrix}\boldsymbol{B}_G & \boldsymbol{0} & \boldsymbol{0}\\ \boldsymbol{0} & \boldsymbol{B}_G & \boldsymbol{0}\\ \boldsymbol{0} & \boldsymbol{0} & \boldsymbol{B}_G\end{bmatrix} \qquad \boldsymbol{B}_{G\psi} = -\frac{1}{6}\begin{bmatrix}B_{G1} & 0 & 0\\ 0 & B_{G2} & 0\\ 0 & 0 & B_{G3}\end{bmatrix} \tag{4.68}$$

where we have defined,

$$\begin{aligned}\boldsymbol{B}_G &= \boldsymbol{c}_1^T N_{11} + \boldsymbol{c}_2^T N_{22} + \boldsymbol{c}_3^T N_{12}\\ B_{G1} &= J_{11}N_{11} + J_{21}N_{22} + J_{31}N_{12}\\ B_{G2} &= J_{12}N_{11} + J_{22}N_{22} + J_{32}N_{12}\\ B_{G3} &= J_{13}N_{11} + J_{23}N_{22} + J_{33}N_{12}\end{aligned}$$

URN:NBN:no-1282

Then, substituting Equations (4.66) and (4.67) into (4.65) yields,

$$\begin{aligned}\delta^2 W^i &= A\,\delta \boldsymbol{r}^T \left(\boldsymbol{B}^T \bar{\mathbb{C}}_t \boldsymbol{B} + \begin{bmatrix} \boldsymbol{B}_{Ga} & \boldsymbol{0} \\ \boldsymbol{0} & \boldsymbol{0} \end{bmatrix} + \begin{bmatrix} \boldsymbol{E}_{\bar{w}}^T \\ \boldsymbol{E}_{\varphi}^T \end{bmatrix} [\boldsymbol{B}_{G\psi}] \, [\boldsymbol{E}_{\bar{w}} \quad \boldsymbol{E}_{\varphi}] \right) \delta \boldsymbol{r} \\ &= \delta \boldsymbol{r}^T \boldsymbol{K}_t \delta \boldsymbol{r} \end{aligned} \tag{4.69}$$

where the tangent stiffness matrix becomes,

$$\boldsymbol{K}_t = A \left[\boldsymbol{B}^T \bar{\mathbb{C}}_t \boldsymbol{B} + \begin{bmatrix} \boldsymbol{B}_{Ga} + \boldsymbol{E}_{\bar{w}}^T \boldsymbol{B}_{G\psi} \boldsymbol{E}_{\bar{w}} & \boldsymbol{E}_{\bar{w}}^T \boldsymbol{B}_{G\psi} \boldsymbol{E}_{\varphi} \\ \boldsymbol{E}_{\varphi}^T \boldsymbol{B}_{G\psi} \boldsymbol{E}_{\bar{w}} & \boldsymbol{E}_{\varphi}^T \boldsymbol{B}_{G\psi} \boldsymbol{E}_{\varphi} \end{bmatrix} \right] \tag{4.70}$$

The first and second terms represent the material and geometric parts, respectively.

URN:NBN:no-1282

Chapter 5

Material Plasticity

5.1 Introduction

The discussions and developments in the foregoing chapters have mainly been based on the concept of equilibrium or the balance equations of momentum. The consequence of these have led to the geometrically nonlinear formulation in Chapters 3–4. In this chapter, we shall extend our discussions to the kinematic description of elasto–plastic deformations. In that respect, the material plasticity formulation which is suitable for the present applications is presented.

Like the geometric nonlinearity, the material modelling due to plasticity is an important part in the field of nonlinear finite elements. For applications involving permanent deformations, plastic forming, plastic collapse and stability, the geometric nonlinearity provides no meaningful results without material modelling due to plasticity.

The theory of plasticity is the mathematical theory for the analysis of irreversible time–independent deformations. It is described in a number of standard textbooks, including Lubliner (1990), Lemaitre and Chaboche (1990), Maugin (1992), and Besseling and van der Giessen (1994). The theory treats the macroscopic behavior of materials in the plastic range, and for metals and alloys it involves mainly the movement of dislocations without the influence of viscous phenomena or the presence of de–cohesion which damages the material.

The damage of a material (which is opposed to the that of structural mechanics which we refer to as collapse) is treated by damage mechanics. On the other hand, when the irreversible deformations are time–dependent, viscoplasticity should be the choice. The validity of plasticity theory is, therefore, limited to relatively low temperatures (with respect to the melting point), quasi–static problems, and non–damaging loads.

From a material curve point of view, one may consider Figure 5.1 which illustrates the analogy between multi–dimensional stress space and the uniaxial stress–strain curve.

URN:NBN:no-1282

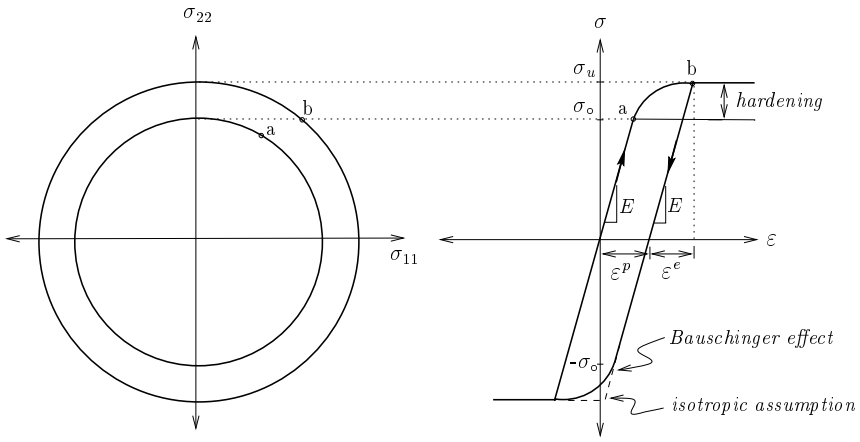

Figure 5.1 Stress space and uniaxial stress–strain curve.

The stress space denoted by a is referred to the initial yield condition and is controlled by the yield stress $\sigma_\circ$.

The existence of hardening takes the initial condition to the ultimate condition denoted by b which is controlled by the ultimate stress σ_u. In other words, hardening characterizes the subsequent yield conditions. Another important observation is that any loading beyond $\sigma_\circ$ is associated with plastic strains. These observations include the two basic assumptions which are made in the conventional theory of plasticity. Namely,

— There exists an initial yield condition which can be illustrated by an initial yield surface in the stress space.

— There exists a flow rule relating the plastic strain increment to the stress increment.

If subsequent yield conditions should be considered, a hardening rule or function is defined. It relates the expansion and/or translation of the yield surface to the amount of plastic deformation. While kinematic hardening translates the yield condition, isotropic hardening expands it and is not associated with the so–called Bauschinger's effect. By Bauschinger's effect it is meant that the material acquires a *strain anisotropy* after plastic strain developments. More precisely, a previous plastic strain with a certain sign diminishes the material resistance with respect to the next plastic strain of the opposite sign.

For *small strain* plasticity, a fundamental assumption is made such that the strain tensor is decomposed into the additive elastic and plastic components. This is expressed as,

$$\boldsymbol{\epsilon} = \boldsymbol{\epsilon}^e + \boldsymbol{\epsilon}^p \tag{5.1}$$

where the superscripts e and p indicate the elastic and plastic terms, respectively. The elastic strains are reversible and linearly related to the stresses by the generalized Hooke's

URN:NBN:no-1282

law. On the contrary, the plastic strains are irreversible and nonlinearly related to the stresses.

5.2 Thermodynamic–Based Plasticity

The classical small strain plasticity theory, as well as the Green and Naghdi (1965) and the *multiplicative split* (e.g. Kröner (1960), Lee and Liu (1967), and Lee (1969)) large strain plasticity theories, fit well in the framework of thermodynamic theory. In other words, all the ingredients of these plasticity formulations can be delivered (Ristinmaa and Ottosen 1996) from the natural laws of thermodynamics. In this section, the evolution equations are established from the final results of thermodynamics. For the description of thermodynamic theory itself, the reader is referred to the lectures of Truesdell (1969).

First, we mention that the interest of any body or *system* is characterized by its *state variables* from which the *state function* can be established. The first law of thermodynamics[1], which may be viewed as the principle of energy conservation, postulates the existence of internal energy as the state function. On the other hand, the second law[2], which was named by Truesdell (1969) as the Clausius–Duhem inequality, postulates the existence of entropy as the state function.

For the purpose of continuum mechanics or constitutive modelling, the second law is turned to the *dissipation inequality* by using the first law. This dissipation is the sum of mechanical (material) dissipation which is associated with Plank's inequality, and the thermal dissipation which is associated with Fourier's inequality. Any constitutive model that satisfies the dissipation inequality, fulfills all the formal conditions enforced by thermodynamics. Our mathematical presentation starts from the total dissipation inequality.

From the local form of the second law of thermodynamics, the *dissipation* inequality which is a special presentation of the Clausius–Duhem inequality can be expressed in terms of the Helmholtz's free energy function Ω. Following Truesdell (1969), (see also Ristinmaa and Ottosen (1996)), this inequality may be expressed as,

$$\delta = -\rho(\dot{\Omega} + \tau\dot{\theta}) + \boldsymbol{\sigma}^T\dot{\boldsymbol{\epsilon}} - \theta^{-1}\boldsymbol{F}^T\boldsymbol{\theta}' \geq 0 \tag{5.2}$$

where ρ is the mass density, τ is the specific entropy, θ is the temperature, $\boldsymbol{\sigma}$ is the stress tensor, $\boldsymbol{F}$ is the heat flux vector[3], $\boldsymbol{\theta}'$ is a vector of temperature gradients over the body, and the superposed dot denotes a time derivative. Assuming isothermal conditions, the influence of temperature disappears leading to the dissipation which is related to the material only. This leads to the so–called mechanical dissipation,

$$\delta_{mech} = -\rho\dot{\Omega} + \boldsymbol{\sigma}^T\dot{\boldsymbol{\epsilon}} \tag{5.3}$$

[1] The sum of the rates of kinetic energy and internal energy equals the sum of mechanical power input and rate of heat input.

[2] The rate of entropy is greater than or equal to the rate of heat input per absolute temperature.

[3] This vector has the direction of the heat flow and its length expresses the heat per unit time which passes through a unit surface area perpendicular to the direction of heat flow.

URN:NBN:no-1282

An important part in constitutive modelling is the choice of proper state variables which characterize the model. It is suitable for our purpose to assume that the plastic process is described by a single scalar variable representing the isotropic hardening. For a reason that will become apparent in the following presentation, we denote this variable as ε^p. In addition, we also assume that the elasto–plastic process can be represented by the elastic strains from Equation (5.1). Then, with isothermal conditions, the free energy function is simply expressed as,

$$\Omega(\boldsymbol{\epsilon}^e, \varepsilon^p) = \Omega^e(\boldsymbol{\epsilon}^e) + \Omega^p(\varepsilon^p) \tag{5.4}$$

which is equal to the deformation energy. When Equations (5.1) and (5.4) are submitted to (5.3) the result is the mechanical dissipation given by,

$$\delta_{mech} = \left(\boldsymbol{\sigma}^T - \rho\frac{\partial\Omega^e}{\partial\boldsymbol{\epsilon}^e}\right)\dot{\boldsymbol{\epsilon}}^e - \rho\frac{\partial\Omega^p}{\partial\varepsilon^p}\dot{\varepsilon}^p + \boldsymbol{\sigma}^T\dot{\boldsymbol{\epsilon}}^p \geq 0 \tag{5.5}$$

Equation (5.5) can be viewed as the total area enclosed by the loading–unloading circle in Figure 5.1. Since this mechanical dissipation remains valid for any elastic strains $\boldsymbol{\epsilon}^e$, it is possible to assign arbitrary values for $\dot{\boldsymbol{\epsilon}}^e$. Therefore, it follows immediately from Equation (5.5) that,

$$\boldsymbol{\sigma} = \rho\frac{\partial\Omega^e}{\partial\boldsymbol{\epsilon}^e} \tag{5.6}$$

where we have dropped the transpose in $\boldsymbol{\sigma}$ simply because the result of the two vectors is similar for a scalar or dot product.

If we define σ as a thermodynamic force conjugate to the hardening parameter $\dot{\varepsilon}^p$, just like $\boldsymbol{\sigma}$ is conjugate to $\dot{\boldsymbol{\epsilon}}^e$, we can write

$$\sigma = \rho\frac{\partial\Omega^p}{\partial\varepsilon^p} \tag{5.7}$$

and, the mechanical dissipation inequality (5.5) takes its suitable form as,

$$\delta_{mech} = \boldsymbol{\sigma}^T\dot{\boldsymbol{\epsilon}}^p - \sigma\dot{\varepsilon}^p \geq 0 \tag{5.8}$$

5.2.1 The Yield Function

The yield function is the central part of plasticity, and its enclosed boundary defines the yield surface. The stresses are considered to have fulfilled the yield function and be admissible only if they are located inside the yield surface or exactly on its boundary line. In that respect, it is convenient to let the yield function depend on the stresses. Furthermore, since the yield surface can be expanded or translated by the amount of hardening the material exhibits, it is evident that the thermodynamic force conjugate to the hardening parameter characterizes the yield surface as well. Accordingly we have,

$$f(\boldsymbol{\sigma}, \sigma) \leq 0 \tag{5.9}$$

URN:NBN:no-1282

This condition tells us that $f < 0$ defines an elastic state while $f = 0$ denotes a plastic state, and a closed surface $f = 0$ defines the yield surface. Therefore, Equation (5.9) plays the role of *plastic potential*.

For work hardening material, the so–called Drucker's postulate (Drucker 1951) has two implications, convexity and normality. The former means that the yield surface is convex, and the latter indicates that the plastic strain is in the direction of the outward normal to the yield surface. The convexity condition is used in the optimization problem that will be encountered in the following sections.

5.2.2 Evolution Laws

The evolution laws of plasticity can be obtained by fulfilling the dissipation inequality (5.8) and satisfying the yield function. The best approach of doing that is to adopt the so–called postulate of maximum dissipation, and maximize δ_{mech} for the constraint given by Equation (5.9). In this way, the problem becomes a nonlinear optimization one and may be turned into the corresponding minimization problem by minimizing the negative δ_{mech} for given values of $\dot{\boldsymbol{\epsilon}}^p$ and $\dot{\varepsilon}^p$.

Following the standard mathematical literature for optimization of functionals, for example Luenberger (1969), we obtain the evolution laws or flow rules for $\dot{\boldsymbol{\epsilon}}^p$ and $\dot{\varepsilon}^p$ exactly as those arising from the associated plasticity theory,

$$\dot{\boldsymbol{\epsilon}}^p = \dot{\lambda}\frac{\partial f}{\partial \boldsymbol{\sigma}} \qquad\qquad \dot{\varepsilon}^p = \dot{\lambda}\frac{\partial f}{\partial \sigma} \tag{5.10}$$

where the non–negative $\dot{\lambda}$ is the plasticity (Lagrangian) multiplier, which is commonly known as the consistency parameter. In solving the above optimization problem, the Kuhn–Tucker theorem (Luenberger 1969) of inequality constraints has been used. This provides the so–called Kuhn–Tucker conditions subject to $\dot{\lambda}$ and f as,

$$f \leq 0 \qquad\qquad \dot{\lambda} \geq 0 \qquad\qquad \dot{\lambda} f = 0 \tag{5.11}$$

The condition $\dot{\lambda} f = 0$ in Equation (5.11) merely says that when f is less than zero, then the corresponding Lagrangian multiplier is absent and there is no plasticity development, i.e. $\dot{\lambda}$ is equal to zero. On the other hand, plasticity development only occurs when f is equal to zero, and in that case $\dot{\lambda}$ must be greater than zero. Accordingly, should the plasticity routine returns a negative plasticity multiplier, the value must be replaced by zero.

5.2.3 Huber–von Mises Plasticity Model

The Huber–von Mises yield criterion, commonly known as the von Mises criterion, provides a simple and popular yield function for metals. This yield function was proposed by Huber

URN:NBN:no-1282

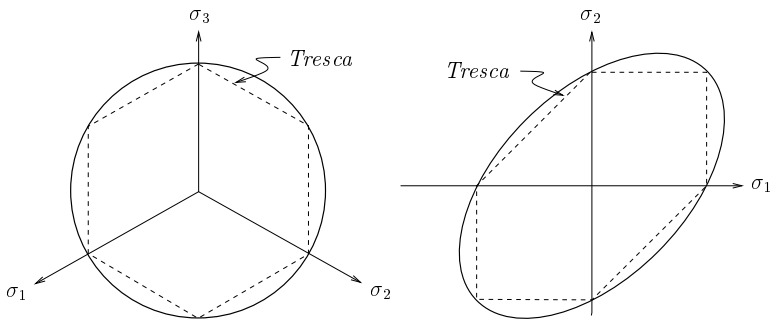

(a) Principal stress π–plane (b) Principal stress 2D–plane

Figure 5.2 Huber–von Mises yield surface.

(1904) and von Mises (1913). Figure 5.2 shows a corresponding characteristic of the Huber–von Mises criterion with the yield criterion of Tresca (1872).

Within the following presentation, the plasticity model is built by following the Huber–von Mises criterion. In addition, the generalized and modified forms of the surfaces resembling this criterion are discussed. The Huber–von Mises yield function is based on the deviatoric stresses, and is given by,

$$f(\boldsymbol{\sigma}, \sigma) = \sqrt{\frac{3}{2}\sigma'_{kl}\sigma'_{kl}} - \sigma(\varepsilon^p) \leq 0 \tag{5.12}$$

where σ'_{kl} are the components of the deviatoric stress tensor, and σ is the uniaxial subsequent yield stress. These are defined as,

$$\sigma'_{kl} = \sigma_{kl} - \frac{1}{3}\delta_{kl}\sigma_{ii} \qquad \sigma = \sigma_\circ + \breve{\sigma}(\varepsilon^p) \tag{5.13}$$

where δ_{kl} is the Kronecker delta, $\breve{\sigma}$ is the additional stress (beyond the yield stress) as a result of hardening, and the values of the indices i, k and l ranges between 1 and 3 with repeated sum. By inserting Equations (5.13) into the quadratic form of Equation (5.12), the yield function for plane stress condition can be expressed as,

$$f = \sigma_{11}^2 - \sigma_{11}\sigma_{22} + \sigma_{22}^2 + 3\sigma_{12}^2 - (\sigma_\circ + \breve{\sigma}(\varepsilon^p))^2 = 0 \tag{5.14}$$

So far, the presentation has assumed isotropic hardening function of a general shape. From now on, let the discussion be limited to the case of *linear isotropic hardening* for the purpose of simplifying the derivations. Accordingly, the additional stress due to hardening will be given by $\breve{\sigma} = H\varepsilon^p$, where H is the isotropic hardening modulus just like E is the elastic material modulus. Finally, the yield function can be expressed in its matrix form as,

$$f(\boldsymbol{\sigma}, \varepsilon^p) = \boldsymbol{\sigma}^T \boldsymbol{P} \boldsymbol{\sigma} - (\sigma_\circ + H\varepsilon^p)^2 = 0 \tag{5.15}$$

URN:NBN:no-1282

where $\boldsymbol{\sigma} = [\sigma_{11} \;\; \sigma_{22} \;\; \sigma_{12}]^T$ with its corresponding $\boldsymbol{\epsilon} = [\epsilon_{11} \;\; \epsilon_{22} \;\; 2\epsilon_{12}]^T$, and

$$\boldsymbol{P} = \frac{1}{2}\begin{bmatrix} 2 & -1 & 0 \\ -1 & 2 & 0 \\ 0 & 0 & 6 \end{bmatrix} \tag{5.16}$$

Submitting the yield function (5.15) to the plasticity evolution Equations (5.10), the associated flow rule and hardening rule for our model are obtained as,

$$\dot{\boldsymbol{\epsilon}}^p = 2\dot{\lambda}\boldsymbol{P}\boldsymbol{\sigma} \qquad\qquad \dot{\varepsilon}^p = 2\dot{\lambda}\sigma \tag{5.17}$$

where the equivalent stress σ follows from Equation (5.15) as,

$$\sigma = \sqrt{\boldsymbol{\sigma}^T\boldsymbol{P}\boldsymbol{\sigma}} \tag{5.18}$$

5.3 Integration Algorithm

From the discussions in Section 5.2.3, it follows that the plasticity problem is subject to the solution of the rate evolution Equations (5.17). Consequently, a numerical integration procedure must usually be employed in order to provide an approximate solution at discrete load increments. Within the load increment, the numerical procedure allows the elasto–plastic problem to be treated as an equivalent elastic problem. In the present work, the so–called *return mapping* algorithm, using the backward Euler difference scheme (Matthies 1989) is considered.

In advancing the solution incrementally to the current state $n+1$, the starting point is from the previous converged solution at state n. Initially, the whole increment is assumed to be elastic and the trial elastic stresses are calculated using the *converged* accumulated plastic strains and Hooke's law as,

$$\boldsymbol{\sigma}_{n+1}^{trial} = \mathbb{C}\,(\boldsymbol{\epsilon}_{n+1} - \boldsymbol{\epsilon}_n^p) \tag{5.19}$$

where $\mathbb{C}$ is the elastic modular matrix.

The yield function (5.15) is checked by using this trial stress and the equivalent converged plastic strain from the previous step n. If the yield surface is exceeded, plastic flow has occurred within the current increment and, accordingly, the correct stresses must be calculated as,

$$\boldsymbol{\sigma}_{n+1} = \mathbb{C}\left(\boldsymbol{\epsilon}_{n+1} - \left[\boldsymbol{\epsilon}_n^p + \Delta\boldsymbol{\epsilon}_{n+1}^p\right]\right) \tag{5.20}$$

where the incremental plastic strains at the current step are given by,

$$\Delta\boldsymbol{\epsilon}_{n+1}^p = \boldsymbol{\epsilon}_{n+1}^p - \boldsymbol{\epsilon}_n^p \tag{5.21}$$

URN:NBN:no-1282

By using Equation (5.19), the correct stresses (5.20) may be expressed as,

$$\boldsymbol{\sigma}_{n+1} = \boldsymbol{\sigma}^{trial}_{n+1} - \mathbb{C}\ \Delta\boldsymbol{\epsilon}^{p}_{n+1} \tag{5.22}$$

Application of an implicit backward Euler difference scheme to the flow rule Equations (5.17), leads to the following relations at step $n+1$,

$$\boldsymbol{\epsilon}^{p}_{n+1} = \boldsymbol{\epsilon}^{p}_{n} + 2\,(\lambda_{n+1} - \lambda_n)\,\boldsymbol{P}\boldsymbol{\sigma}_{n+1} = \boldsymbol{\epsilon}^{p}_{n} + 2\lambda\boldsymbol{P}\boldsymbol{\sigma}_{n+1} \tag{5.23}$$

$$\varepsilon^{p}_{n+1} = \varepsilon^{p}_{n} + 2\,(\lambda_{n+1} - \lambda_n)\,\sigma_{n+1} = \varepsilon^{p}_{n} + 2\lambda\sigma_{n+1} \tag{5.24}$$

where we have denoted the term in the parenthesis as λ, the plasticity multiplier or consistency parameter corresponding to the current step. By using Equation (5.23), we can express the plastic strain increment (5.21) as,

$$\Delta\boldsymbol{\epsilon}^{p}_{n+1} = 2\lambda\boldsymbol{P}\boldsymbol{\sigma}_{n+1} \tag{5.25}$$

and, for the correct stresses, Equation (5.22) becomes,

$$\boldsymbol{\sigma}_{n+1} = \left[\boldsymbol{I} + 2\lambda\mathbb{C}\boldsymbol{P}\right]^{-1}\boldsymbol{\sigma}^{trial}_{n+1} \tag{5.26}$$

with λ remaining as the sole unknown.

For the case of isotropic elastic response, the inverse of the matrix in Equation (5.26) takes a remarkably simple form because $\mathbb{C}$ and $\boldsymbol{P}$ have the same characteristic subspaces. To facilitate that simplification, the spectral decomposition theorem of the solution to the symmetric eigenvalue problem of Parlett (1997) is utilized such that,

$$[\mathbb{C}\boldsymbol{P}]\ \mathbb{Q} = \mathbb{Q}\boldsymbol{\Lambda} \quad \Longrightarrow \quad \mathbb{C}\boldsymbol{P} = \mathbb{Q}\boldsymbol{\Lambda}\mathbb{Q}^{-1} \tag{5.27}$$

where $\mathbb{Q}$ and $\boldsymbol{\Lambda} = \boldsymbol{\Lambda}_C\boldsymbol{\Lambda}_P$ are, respectively, the matrix of eigenvectors and the diagonal matrix of eigenvalues of the product matrix $\mathbb{C}\boldsymbol{P}$. Therefore, Equation (5.26) can be re–expressed as,

$$\boldsymbol{\sigma}_{n+1} = \left(\mathbb{Q}\left[\boldsymbol{I} + 2\lambda\boldsymbol{\Lambda}\right]^{-1}\mathbb{Q}^{-1}\right)\boldsymbol{\sigma}^{trial}_{n+1} = \mathbb{V}_{n+1}\boldsymbol{\sigma}^{trial}_{n+1} \tag{5.28}$$

where,

$$\mathbb{Q} = \frac{\sqrt{2}}{2}\begin{bmatrix} 1 & -1 & 0 \\ 1 & 1 & 0 \\ 0 & 0 & \sqrt{2} \end{bmatrix} \tag{5.29}$$

$$\boldsymbol{\Lambda}_A = diag\begin{bmatrix} \dfrac{1}{2} & \dfrac{3}{2} & 3 \end{bmatrix} \qquad \boldsymbol{\Lambda}_P = diag\begin{bmatrix} \dfrac{E}{1-\nu} & \dfrac{E}{1+\nu} & \dfrac{cE}{(1+\nu)} \end{bmatrix} \tag{5.30}$$

This decomposition method was proposed by Matthies (1989) for simplifying the plastic flow computations. Following this proposal, it has also been applied in resultants

URN:NBN:no-1282

plasticity by Ibrahimbegović and Frey (1992), and Simo and Kennedy (1992). In the coming sections, explicit components of matrix $\mathbb{V}_{n+1}$ are derived.

For a material described by $\mathbb{C}$ and $\boldsymbol{P}$, the solution of the eigenproblem given by Equation (5.27) is known after solving it only once. In addition, since the elastic trial stresses can be obtained from Hooke's law, it only remains to determine the plasticity multiplier λ which fulfills Equation (5.15). For that purpose, the Newton–Raphson iteration procedure for the solution a nonlinear function $f(\lambda)$ is employed so that,

$$\lambda^{i+1} = \lambda^i - f/f_{,\lambda} \qquad\qquad \lambda^0 = 0 \tag{5.31}$$

in which i is the local iteration number, and $f_{,\lambda}$ is the derivative with respect to λ.

5.3.1 Consistent tangent Modular Matrix

In the context of finite element method as discussed in Chapter 2, the solution of nonlinear equilibrium equations is usually accomplished by an iterative procedure based on Newton's method. The process involves a sequencial solution of linearized equations obtained from the balance equations of momentum.

To preserve the asymptotic quadratic convergence of the iterative scheme, the consistency between the element tangent stiffness and the integration algorithm of the rate equations plays a crucial role. In other words, the tangent modular matrix that appears in the linearized problem must be obtained by consistent linearization of the response function resulting from the integration algorithm of the rate equations. This concept appear to have first been applied by Simo and Taylor (1985).

To obtain the tangent modular matrix $\mathbb{C}_t$ which is *consistent* with the integration algorithm presented in Section 5.3, we need a consistent linearization of the discrete stress–strain relation (5.20),

$$\boldsymbol{\sigma}_{n+1} = \mathbb{C}\left(\boldsymbol{\epsilon}_{n+1} - \boldsymbol{\epsilon}^p_{n+1}\right) \tag{5.32}$$

such that we have the relation,

$$d\boldsymbol{\sigma}_{n+1} = \mathbb{C}_t\, d\boldsymbol{\epsilon}_{n+1} \tag{5.33}$$

Accordingly, the linearized Equation (5.32) can be expressed as,

$$d\boldsymbol{\sigma}_{n+1} = \mathbb{C}\left(d\boldsymbol{\epsilon}_{n+1} - d\boldsymbol{\epsilon}^p_{n+1}\right) \quad \Longrightarrow \quad d\boldsymbol{\epsilon}_{n+1} = \mathbb{C}^{-1} d\boldsymbol{\sigma}_{n+1} + d\boldsymbol{\epsilon}^p_{n+1} \tag{5.34}$$

in which $d\boldsymbol{\epsilon}^p_{n+1}$ is obtained by linearizing Equation (5.23) which gives,

$$d\boldsymbol{\epsilon}^p_{n+1} = 2\lambda \boldsymbol{P}\; d\boldsymbol{\sigma}_{n+1} + 2\boldsymbol{P}\boldsymbol{\sigma}_{n+1} d\lambda = 2\lambda \boldsymbol{P}\; d\boldsymbol{\sigma}_{n+1} + \hat{\boldsymbol{n}}_{n+1} d\lambda \tag{5.35}$$

where we have denoted the plastic flow direction as,

$$\hat{\boldsymbol{n}}_{n+1} = \frac{\partial f}{\partial \boldsymbol{\sigma}_{n+1}} = 2\boldsymbol{P}\boldsymbol{\sigma}_{n+1} \tag{5.36}$$

URN:NBN:no-1282

By combining the final versions of Equations (5.34) and (5.35), we obtain

$$d\boldsymbol{\epsilon}_{n+1} = \left[\mathbb{C}^{-1} + 2\lambda \boldsymbol{P}\right] d\boldsymbol{\sigma}_{n+1} + \hat{\boldsymbol{n}}_{n+1} d\lambda \tag{5.37}$$

where we shall denote the terms in the brackets as the algorithmic compliance $\mathbb{H}^{-1}_{n+1}$. Using the spectral decomposition theorem by doing similar to what was done in Equation (5.26), the compliance can be expressed as,

$$\mathbb{H}_{n+1} = \left[\mathbb{C}^{-1} + 2\lambda \boldsymbol{P}\right]^{-1} = \left(\mathbb{Q}\left[\boldsymbol{I} + 2\lambda \boldsymbol{\Lambda}\right]^{-1} \mathbb{Q}^{-1}\right) \mathbb{C} = \mathbb{V}_{n+1} \mathbb{C} \tag{5.38}$$

For the definition of $d\lambda$ which is required in Equation (5.37), we linearize the yield function (5.15), the equivalent plastic strain (5.24), and the equivalent uniaxial stress (5.18), by writing

$$df = \hat{\boldsymbol{n}}_{n+1}\ d\boldsymbol{\sigma}_{n+1} - 2H\left(\sigma_\circ + H\varepsilon^p_{n+1}\right)\ d\varepsilon^p_{n+1} = 0 \tag{5.39}$$

$$d\varepsilon^p_{n+1} = 2\lambda\ d\sigma_{n+1} + 2\sigma_{n+1}\ d\lambda = \frac{\lambda}{\sigma_{n+1}} \hat{\boldsymbol{n}}^T_{n+1}\ d\boldsymbol{\sigma}_{n+1} + 2\sigma_{n+1}\ d\lambda \tag{5.40}$$

Substituting Equation (5.40) into (5.39) yields,

$$d\lambda = \frac{1}{\beta_{n+1}} \hat{\boldsymbol{n}}^T_{n+1}\ d\boldsymbol{\sigma}_{n+1} \tag{5.41}$$

where we have introduced the following definitions,

$$\beta_{n+1} = \frac{2\alpha\sigma_{n+1}}{1 - \alpha\lambda/\sigma_{n+1}} \qquad \alpha = 2H\left(\sigma_\circ + H\varepsilon^p_{n+1}\right) \tag{5.42}$$

Now the linearized discrete stress–strain Equation (5.37) can be re–expressed as,

$$d\boldsymbol{\sigma} = \left[\mathbb{H}^{-1} + \frac{1}{\beta} \hat{\boldsymbol{n}}\, \hat{\boldsymbol{n}}^T\right]^{-1}\ d\boldsymbol{\epsilon} \tag{5.43}$$

where we have dropped the subscript $n+1$ for clarity. The inverse can be obtained by using the Shermann–Morrison formula for the inverse of rank–one update, (see for example Golub and Loan (1989)), and finally the consistent tangent modular matrix becomes,

$$\mathbb{C}_t = \mathbb{H} - \frac{\mathbb{H}\hat{\boldsymbol{n}}\, \hat{\boldsymbol{n}}^T \mathbb{H}}{\hat{\boldsymbol{n}}^T \mathbb{H} \hat{\boldsymbol{n}} + \beta} \tag{5.44}$$

A similar matrix was obtained by Ibrahimbegović and Frey (1992) for elasto–plastic formulation based on stress resultants.

It is important to note that the local iterations in Equation (5.31) should strictly be based on the last converged results at state n for the effect of the consistent modular matrix to be considered. Any solution that is based on the intermediate unconverged results will lead to a questionable use of matrix (5.44) as a continuum tangent modular matrix (Simo and Taylor 1985).

URN:NBN:no-1282

5.4 Through–the Thickness Integration

There are two principal methods that are used to describe the nonlinear behavior in shell elements, namely the volume and area approaches. In the volume approach, the constitutive equations in terms of stresses and strains are applied to the shell layers and then integrated through the thickness. This conventional method, that we will refer to it as *through–the thickness integration*, is generally viewed as computationally demanding over the other.

The area approach is generally believed to offer reasonable reduction in computer time and storage by formulating the constitutive laws in terms of stress resultants, conjugate with the generalized strains of the mid–surface (Simo and Kennedy 1992). In this way, the integration over the thickness is avoided. This method, that is called the *stress resultants plasticity*, has the disadvantage that additional assumptions regarding the stress distribution over the shell thickness must be introduced.

With respect to the computational cost, however, it will nonetheless appear in this work that the advantage of the second approach over the first is not as significant as it is generally believed. In addition, since the second approach is based on the pre–integrated equations over the thickness, its final equations are usually less trivial as regard to computer implementation. It should not be ruled out, however, that there may be cases where the second approach can offer smoother numerical solutions than the first.

In the present section we shall focus on the volume approach and leave the area approach for the next section. So far we have presented all the equations in this chapter assuming that the rate equations will be solved at each respective integration point. Therefore, the yield function for through–the thickness integration can be taken from its original form as given by Equation (5.15) as,

$$f(\boldsymbol{\sigma}, \varepsilon^p) = \boldsymbol{\sigma}^T \boldsymbol{P} \boldsymbol{\sigma} - (\sigma_\circ + H\varepsilon^p)^2 = 0 \tag{5.45}$$

Following the discussion in Section 5.3, the next step will be to find an explicit form of matrix $\mathbb{V}_{n+1}$ in Equation (5.28). Performing the involved matrix algebra analytically, the result becomes,

$$\mathbb{V}_{n+1} = \frac{1}{2} \begin{bmatrix} s_1 + s_2 & s_1 - s_2 & 0 \\ s_1 - s_2 & s_1 + s_2 & 0 \\ 0 & 0 & s_3 \end{bmatrix} \tag{5.46}$$

where the following definitions have been made,

$$s_1 = \frac{k}{k + \lambda E} \qquad s_2 = \frac{h}{h + 3\lambda E} \qquad s_3 = \frac{2h}{h + 6c\lambda E} \tag{5.47}$$

in which $k = 1 - \nu$ and $h = 1 + \nu$. Note that for $c = 1/2$, which is the usual case, $s_3 = 2s_2$.

Substitution of Equations (5.24) and (5.28) into the yield function (5.45), and use of the spectral decomposition theorem (5.27), lead to an explicit yield function as a nonlinear

URN:NBN:no-1282

function of a single scalar variable λ,

$$f(\lambda) = \sigma_{trial}^2 - \left(\sigma_\circ + H\left[\varepsilon_n^p + 2\lambda\sigma_{trial}\right]\right)^2 = 0 \tag{5.48}$$

where,

$$\sigma_{trial} = \sqrt{\boldsymbol{\sigma}_{trial}^T \mathbb{P} \boldsymbol{\sigma}_{trial}} \tag{5.49}$$

$$\mathbb{P} = \mathbb{Q}^{-T}\left[\boldsymbol{I} + 2\lambda\boldsymbol{\Lambda}\right]^{-T}\boldsymbol{\Lambda}_P\left[\boldsymbol{I} + 2\lambda\boldsymbol{\Lambda}\right]^{-1}\mathbb{Q}^{-1} \tag{5.50}$$

in which $\boldsymbol{\Lambda}_P$ is the diagonal matrix of eigenvalues of matrix $\boldsymbol{P}$. The subscript $n+1$ has been omitted for clarity. The matrix algebra in Equation (5.50) can also be performed analytically to obtain,

$$\mathbb{P} = \frac{1}{4}\begin{bmatrix} s_1^2 + 3s_2^2 & s_1^2 - 3s_2^2 & 0 \\ s_1^2 - 3s_2^2 & s_1^2 + 3s_2^2 & 0 \\ 0 & 0 & 3s_3^2 \end{bmatrix} \tag{5.51}$$

where s_1, s_2, and s_3 are defined in Equation (5.47).

What remains now for the solution of the nonlinear Equation (5.31), is the derivative of the yield function (5.45) that we can write it as,

$$f_{,\lambda} = \hat{\sigma}_{trial}^2 - 2H\left(\sigma_\circ + H\left[\varepsilon_n^p + 2\lambda\sigma_{trial}\right]\right)\left(2\sigma_{trial} + \frac{\hat{\sigma}_{trial}^2}{\sigma_{trial}}\lambda\right) \tag{5.52}$$

in which,

$$\hat{\sigma}_{trial} = \sqrt{\boldsymbol{\sigma}_{trial}^T \hat{\mathbb{P}} \boldsymbol{\sigma}_{trial}} \tag{5.53}$$

where $\hat{\mathbb{P}}$ is given by the derivative of $\mathbb{P}$ in Equation (5.50) with respect to λ. This matrix can be obtained as,

$$\hat{\mathbb{P}} = \frac{1}{4}\begin{bmatrix} \hat{s}_1 + 3\hat{s}_2 & \hat{s}_1 - 3\hat{s}_2 & 0 \\ \hat{s}_1 - 3\hat{s}_2 & \hat{s}_1 + 3\hat{s}_2 & 0 \\ 0 & 0 & 3\hat{s}_3 \end{bmatrix} \tag{5.54}$$

where,

$$\hat{s}_1 = -\frac{2}{k}Es_1^3 \qquad \hat{s}_2 = -\frac{6}{h}Es_2^3 \qquad \hat{s}_3 = -\frac{6}{h}cEs_3^3 \tag{5.55}$$

By using Equations (5.51) and (5.54), we can go further and give the explicit expressions for Equations (5.49) and (5.53) so that,

$$\sigma_{trial}^2 = \left[\sigma_{11}^2 + \sigma_{22}^2\right]\mathbb{P}_{11} + 2\sigma_{11}\sigma_{22}\mathbb{P}_{12} + \sigma_{12}^2\mathbb{P}_{33} \tag{5.56}$$

URN:NBN:no-1282

$$\hat{\sigma}^2_{trial} = \left[\sigma^2_{11} + \sigma^2_{22}\right] \hat{\mathbb{P}}_{11} + 2\sigma_{11}\sigma_{22}\hat{\mathbb{P}}_{12} + \sigma^2_{12}\hat{\mathbb{P}}_{33} \tag{5.57}$$

where σ_{ij} are the components of the stress tensor, and $\mathbb{P}_{ij}$ and $\hat{\mathbb{P}}_{ij}$ are respectively the scalar components of matrices $\mathbb{P}$ and $\hat{\mathbb{P}}$.

Having solved for the plasticity multiplier λ, the current stresses at the integration point are obtained from Equation (5.28) and the consistent tangent modular matrix from Equation (5.44). Then the resultants of the constitutive equation are obtained as described in Section 2.7.2.

5.5 Stress Resultants Plasticity

In this section, we shall present the theoretical formulation for the modification of the flow theory of plasticity to the application on M–N type interaction curves, instead of σ–type yield functions discussed in the foregoing sections. In other words, the constitutive laws will be presented in terms of generalized stresses which in Kirchoff–Love assumptions are the stress resultants $\boldsymbol{N}$ and stress couples $\boldsymbol{M}$ that we shall refer to both of them as *stress resultants*. The yield function is represented by stress resultants which are obtained by pre–integration of the corresponding equations presented in Section 2.7.2 after neglecting any partial yielding.

Typical for the previous equations, the approximate Ilyushin (1956) yield function is used. However, the word approximate is dropped unless needed specifically. This criterion involves quadratic stress intensities and was derived by means of strain ratio parameters. In fact, the Ilyushin yield criterion is a special form of the Huber–von Mises criterion expressed in terms of stress resultants. To illustrate, let Equation (5.14) be presented in terms of the stress resultants of the outer fibers of a shell cross–section.

As long as the material remain elastic through the depth of the shell, the stress distribution over the cross–section is linear and the components at the outer fibers are given by,

$$\sigma_{ij} = \frac{N_{ij}}{t} \pm 6\frac{M_{ij}}{t^2} \tag{5.58}$$

When Equation (5.58) is inserted to (5.14), the result is,

$$f = \left(\frac{\bar{N}}{t^2} \pm \frac{12\bar{P}}{t^3} + \frac{36\bar{M}}{t^4}\right) - \sigma^2 = 0 \tag{5.59}$$

where σ is given in Equation (5.13), and

$$\bar{N} = N^2_{11} - N_{11}N_{22} + 3N^2_{12} + N^2_{22} \tag{5.60}$$

$$\bar{M} = M^2_{11} - M_{11}M_{22} + 3M^2_{12} + M^2_{22} \tag{5.61}$$

$$\bar{P} = N_{11}M_{11} - 0.5\left(N_{11}M_{22} + N_{22}M_{11}\right) + 3N_{12}M_{12} + N_{22}M_{22} \tag{5.62}$$

Equation (5.59) has been applied by Eidsheim (1980) as the initial yield criterion, while keeping the Ilyushin surface as the limit criterion.

URN:NBN:no-1282

5.5.1 The Approximate Ilyushin Surface

The exact Ilyushin yield surface has not been used because its parametric form in which it was described was not amenable to calculation (Burgoyne and Brennan 1993b). Instead, its approximate version has widely been applied. In bending dominant conditions, Ilyushin suggested an approximate surface which in its quadratic form can be expressed as,

$$f(\boldsymbol{N}, \boldsymbol{M}) = \left(\frac{\bar{N}}{t^2} + \frac{4\mu\bar{P}}{\sqrt{3}t^3} + \frac{16\bar{M}}{t^4} \right) - \sigma^2 = 0 \tag{5.63}$$

where $\mu = |\bar{P}|/\bar{P} = \pm 1$. What is said to be a better approximation has been given by Ivanov (1967), (see also Crisfield (1979)).

It is seen that apart from the two coefficients of the last two terms within the parenthesis, Equations (5.59) and (5.63) are quite similar. This difference is mainly caused by the assumed stress distribution over the cross–section where only two–thirds of the bending term in Equation (5.58) is needed for an almost recovery of the approximate Ilyushin surface.

Similar to Equation (5.15), the functional (5.63) may be expressed in matrix form as,

$$f(\bar{\boldsymbol{\sigma}}, \varepsilon^p) = \bar{\boldsymbol{\sigma}}^T \boldsymbol{A} \bar{\boldsymbol{\sigma}} - \frac{1}{\sigma_\circ^2} \left(\sigma_\circ + H\varepsilon^p \right)^2 = 0 \tag{5.64}$$

where $\bar{\boldsymbol{\sigma}}$ is the stress resultant tensor, and matrix $\boldsymbol{A}$ is of constant coefficients. These are defined,

$$\bar{\boldsymbol{\sigma}} = \begin{bmatrix} \boldsymbol{N} \\ \boldsymbol{M} \end{bmatrix} \qquad \boldsymbol{A} = \begin{bmatrix} \frac{1}{n_\circ^2}\boldsymbol{P} & \frac{\mu}{2\sqrt{3}m_\circ n_\circ}\boldsymbol{P} \\ \frac{\mu}{2\sqrt{3}m_\circ n_\circ}\boldsymbol{P} & \frac{1}{m_\circ^2}\boldsymbol{P} \end{bmatrix} \tag{5.65}$$

where $\boldsymbol{P}$ is given by Equation (5.16). In accordance to the discussions on stress distribution which follows after Equation (5.63), the following definitions are used,

$$n_\circ = \sigma_\circ t \qquad m_\circ = \frac{1}{4}\sigma_\circ t^2 \tag{5.66}$$

Expressions similar to (5.64) have been applied by Ibrahimbegović and Frey (1992), and Simo and Kennedy (1992), to represent the Ilyushin–Shapiro yield criteria.

The yield surface defined by Equation (5.64) remains convex, however, as a result of μ being equal to ± 1 it has corner discontinuities. This results into a double surface for stress update at the corner. Like other yield surfaces with corners, many works have been reported to treat these discontinuities (see Crisfield (1997) for references). In their publications, Burgoyne and Brennan (1993a) and Burgoyne and Brennan (1993b) have presented what they termed as the *exact Ilyushin yield surface* which reduces the discontinuties from two points to one. In the present work, a simplified approach is used to treat the discontinuities in the approximate surface given by (5.64).

URN:NBN:no-1282

5.5.2 Resultants Plasticity Equations

Adopting the stress resultants yield criterion, means in principle that all the plasticity equations resulting from the integration algorithm should be re–derived using the new yield function. For the present case, it can nonetheless be shown that the equations will remain the same but the vectors and matrices need to be replaced with their corresponding resultant ones. As it has appeared in Equation (5.64) and in what follows, we shall denote all the matrices corresponding to resultants by a superposed bar, except for $\boldsymbol{P}$ which has been replaced by $\boldsymbol{A}$. As we have divided the resultants yield function (5.64) throughout by the square of $\sigma_\circ$, the definition of α in Equation (5.42) is also replaced by,

$$\bar{\alpha} = \frac{2H}{\sigma_\circ^2}\left(\sigma_\circ + H\varepsilon^p_{n+1}\right) \tag{5.67}$$

Following a similar procedure as done for the integration through–the thickness in Section 5.3, the correct stress resultants are given in terms of the trial stress resultants as,

$$\bar{\boldsymbol{\sigma}}_{n+1} = \left[\boldsymbol{I} + 2\lambda\bar{\mathbb{C}}\boldsymbol{A}\right]^{-1}\bar{\boldsymbol{\sigma}}^{trial}_{n+1} \tag{5.68}$$

where $\bar{\mathbb{C}}$ is the elastic modular matrix which is given by,

$$\bar{\mathbb{C}} = \begin{bmatrix} t\mathbb{C} & \mathbf{0} \\ \mathbf{0} & \frac{t^3}{12}\mathbb{C} \end{bmatrix} \tag{5.69}$$

Using the spectral decomposition theorem (5.27), Equation (5.68) can be conveniently expressed as,

$$\bar{\boldsymbol{\sigma}}_{n+1} = \left(\bar{\mathbb{Q}}\left[\boldsymbol{I} + 2\lambda\bar{\boldsymbol{\Lambda}}\right]^{-1}\bar{\mathbb{Q}}^{-1}\right)\bar{\boldsymbol{\sigma}}^{trial}_{n+1} = \bar{\mathbb{V}}_{n+1}\bar{\boldsymbol{\sigma}}^{trial}_{n+1} \tag{5.70}$$

where $\bar{\mathbb{Q}}$ is the matrix of eigenvectors of the product matrix $\bar{\mathbb{C}}\boldsymbol{A}$, and $\bar{\boldsymbol{\Lambda}} = \boldsymbol{\Lambda}_{\bar{C}}\boldsymbol{\Lambda}_A$ is the corresponding diagonal matrix of eigenvalues. These are given by,

$$\bar{\mathbb{Q}} = \begin{bmatrix} \mathbb{Q} & \mathbf{0} \\ \mathbf{0} & \mathbb{Q} \end{bmatrix} \tag{5.71}$$

$$\boldsymbol{\Lambda}_A = diag\left[\frac{1}{2n_\circ^2} \quad \frac{3}{2n_\circ^2} \quad \frac{3}{n_\circ^2} \quad \frac{1}{2m_\circ^2} \quad \frac{3}{2m_\circ^2} \quad \frac{3}{m_\circ^2}\right] \tag{5.72}$$

$$\boldsymbol{\Lambda}_{\bar{C}} = diag\left[\frac{Et}{1-\nu} \quad \frac{Et}{1+\nu} \quad \frac{cEt}{(1+\nu)} \quad \frac{Et^3}{12(1-\nu)} \quad \frac{Et^3}{12(1+\nu)} \quad \frac{cEt^3}{12(1+\nu)}\right] \tag{5.73}$$

5.5.3 Modified Yield Surface

For the purpose of avoiding the corner discontinuities in the Ilyushin yield surface, we consider a rather simplified approach by setting $\mu = 0$ in Equation (5.63). By doing so, we

URN:NBN:no-1282

are rendering the surface (5.64) to a hyperellipse and hence a smooth single surface for stress update of any return value, instead of two active yield surfaces on special circumstances.

With the integration algorithm presented in Section 5.3, the current modification simplifies the calculations remarkably. The outcome is the solution of a single scalar equation for the plasticity multiplier as it was for the through–the thickness integration in Section 5.4. This modified form was initially proposed by Skallerud and Haugen (1999), and it has been applied with success since then by Mohammed *et al.* (2001).

With respect to the approximate yield function, however, the present modification introduces inaccuracy ranging between 0—12 percent as illustrated in Figure 5.3. By considering the uncertainties involved in other input parameters (e.g. boundary conditions, external loads, geometry, and material properties) and the fact that an approximation is already introduced in the Ilyushin original surface, it may be considered acceptable to employ this modified surface.

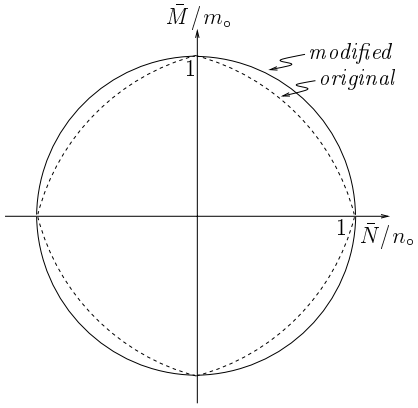

Figure 5.3 The Ilyushin yield surafce.

Substituting Equation (5.70) into the yield function (5.64) together with the update equation for the equivalent plastic strains similar to Equation (5.24), the modified yield surface can be expressed as a nonlinear function of a single scalar variable λ as,

$$f(\lambda) = \bar{\sigma}^2_{trial} - \left(1 + \frac{H}{\sigma_\circ}\left[\varepsilon^p_n + 2\lambda\bar{\sigma}_{trial}\right]\right)^2 = 0 \tag{5.74}$$

where,

$$\bar{\sigma}_{trial} = \sqrt{\bar{\boldsymbol{\sigma}}^T_{trial}\mathbb{A}\bar{\boldsymbol{\sigma}}_{trial}} \tag{5.75}$$

$$\mathbb{A} = \bar{\mathbb{Q}}^{-T}\left[\boldsymbol{I} + 2\lambda\boldsymbol{\Lambda}\right]^{-T}\boldsymbol{\Lambda}_A\left[\boldsymbol{I} + 2\lambda\boldsymbol{\Lambda}\right]^{-1}\bar{\mathbb{Q}}^{-1} \tag{5.76}$$

in which $\boldsymbol{\Lambda}_A$ is the diagonal matrix of eigenvalues of matrix $\boldsymbol{A}$. The subscript $n+1$ has been omitted for clarity. The derivative of the yield function, which is required for the

URN:NBN:no-1282

solution of the nonlinear Equation (5.48), can be expressed as,

$$f_{,\lambda} = \hat{\bar{\sigma}}^2_{trial} - \frac{2H}{\sigma_\circ}\left(1 + \frac{H}{\sigma_\circ}\left[\varepsilon^p_n + 2\lambda\bar{\sigma}_{trial}\right]\right)\left(2\bar{\sigma}_{trial} + \frac{\hat{\bar{\sigma}}^2_{trial}}{\bar{\sigma}_{trial}}\lambda\right) \tag{5.77}$$

where,

$$\hat{\bar{\sigma}}_{trial} = \sqrt{\bar{\boldsymbol{\sigma}}^T_{trial}\hat{\mathbb{A}}\bar{\boldsymbol{\sigma}}_{trial}} \tag{5.78}$$

in which $\hat{\mathbb{A}}$ is given by the derivative of $\mathbb{A}$ with respect to λ.

5.5.4 Simplified Matrices and Explicit Equations

Following the derivations in Sections 5.5.2 and 5.5.3, one may agree that the matrix operations involved in the the nonlinear Equation (5.31) can be quite demanding with respect to computer time. However, it will be shown in this section that these operations can actually be performed analytically so as to minimize the computer time. As a result, simple and explicit expressions are obtained for the plasticity calculations, notably the modified yield surface (Equation (5.74)).

To facilitate the simplification, we first focus on Equations (5.68) and (5.76) for matrices $\bar{\mathbb{V}}$ and $\mathbb{A}$. After lengthy matrix algebra, these matrices can be expressed as

$$\bar{\mathbb{V}} = \begin{bmatrix} \mathbb{V}^n & \mathbf{0} \\ \mathbf{0} & \mathbb{V}^m \end{bmatrix} \qquad \mathbb{A} = \begin{bmatrix} \mathbb{A}^n & \mathbf{0} \\ \mathbf{0} & \mathbb{A}^m \end{bmatrix} \tag{5.79}$$

in which,

$$\mathbb{V}^n = \frac{1}{2}\begin{bmatrix} n_1 + n_2 & n_1 - n_2 & 0 \\ n_1 - n_2 & n_1 + n_2 & 0 \\ 0 & 0 & n_3 \end{bmatrix} \qquad \mathbb{V}^m = \frac{1}{2}\begin{bmatrix} m_1 + m_2 & m_1 - m_2 & 0 \\ m_1 - m_2 & m_1 + m_2 & 0 \\ 0 & 0 & m_3 \end{bmatrix} \tag{5.80}$$

$$\mathbb{A}^n = \frac{1}{4n^2_\circ}\begin{bmatrix} n_1^2 + 3n_2^2 & n_1^2 - 3n_2^2 & 0 \\ n_1^2 - 3n_2^2 & n_1^2 + 3n_2^2 & 0 \\ 0 & 0 & 3n_3^2 \end{bmatrix} \tag{5.81}$$

$$\mathbb{A}^m = \frac{1}{4m^2_\circ}\begin{bmatrix} m_1^2 + 3m_2^2 & m_1^2 - 3m_2^2 & 0 \\ m_1^2 - 3m_2^2 & m_1^2 + 3m_2^2 & 0 \\ 0 & 0 & 3m_3^2 \end{bmatrix} \tag{5.82}$$

where the following definitions have been made,

$$n_1 = \frac{k_n}{k_n + \lambda E t} \qquad n_2 = \frac{h_n}{h_n + 3\lambda E t} \qquad n_3 = \frac{2h_n}{h_n + 6c\lambda E t} \tag{5.83}$$

$$m_1 = \frac{k_m}{k_m + \lambda E t^3} \qquad m_2 = \frac{h_m}{h_m + \lambda E t^3} \qquad m_3 = \frac{2h_m}{h_m + 2c\lambda E t^3} \tag{5.84}$$

URN:NBN:no-1282

in which,

$$k_n = n_\circ^2(1-\nu) \qquad h_n = n_\circ^2(1+\nu) \qquad k_m = 12m_\circ^2(1-\nu) \qquad h_m = 4m_\circ^2(1+\nu) \tag{5.85}$$

Similarly, the derivative of matrix $\mathbb{A}$ with respect to the consistency parameter λ, which is required in Equation (5.78), can be expressed as

$$\hat{\mathbb{A}} = \begin{bmatrix} \hat{\mathbb{A}}^n & \mathbf{0} \\ \mathbf{0} & \hat{\mathbb{A}}^m \end{bmatrix} \tag{5.86}$$

where,

$$\hat{\mathbb{A}}^n = \frac{1}{4n_\circ^2}\begin{bmatrix} \hat{n}_1 + 3\hat{n}_2 & \hat{n}_1 - 3\hat{n}_2 & 0 \\ \hat{n}_1 - 3\hat{n}_2 & \hat{n}_1 + 3\hat{n}_2 & 0 \\ 0 & 0 & 3\hat{n}_3 \end{bmatrix} \tag{5.87}$$

$$\hat{\mathbb{A}}^m = \frac{1}{4m_\circ^2}\begin{bmatrix} \hat{m}_1 + 3\hat{m}_2 & \hat{m}_1 - 3\hat{m}_2 & 0 \\ \hat{m}_1 - 3\hat{m}_2 & \hat{m}_1 + 3\hat{m}_2 & 0 \\ 0 & 0 & 3\hat{m}_3 \end{bmatrix} \tag{5.88}$$

in which,

$$\hat{n}_1 = -\frac{2}{k_n}Etn_1^3 \qquad \hat{n}_2 = -\frac{6}{h_n}Etn_2^3 \qquad \hat{n}_3 = -\frac{6}{h_n}cEtn_3^3 \tag{5.89}$$

$$\hat{m}_1 = -\frac{2}{k_m}Et^3m_1^3 \qquad \hat{m}_2 = -\frac{2}{h_m}Et^3m_2^3 \qquad \hat{m}_3 = -\frac{2}{h_m}cEt^3m_3^3 \tag{5.90}$$

Substituting Equations (5.79) and (5.81) into Equation (5.75) yields an explicit form of $\bar{\sigma}^2_{trial}$ as

$$\begin{aligned} \bar{\sigma}^2_{trial} \;=\; & \left[N_{11}^2 + N_{22}^2\right]\mathbb{A}_{11} + 2N_{11}N_{22}\mathbb{A}_{12} + N_{12}^2\mathbb{A}_{33} + \\ & \left[M_{11}^2 + M_{22}^2\right]\mathbb{A}_{44} + 2M_{11}M_{22}\mathbb{A}_{45} + M_{12}^2\mathbb{A}_{66} \end{aligned} \tag{5.91}$$

where N_{ij} and M_{ij} are the components of the stress resultant tensor. A similar expression corresponding to $\hat{\bar{\sigma}}^2_{trial}$ (i.e. Equation (5.78)) can be expressed as,

$$\begin{aligned} \hat{\bar{\sigma}}^2_{trial} \;=\; & \left[N_{11}^2 + N_{22}^2\right]\hat{\mathbb{A}}_{11} + 2N_{11}N_{22}\hat{\mathbb{A}}_{12} + N_{12}^2\hat{\mathbb{A}}_{33} + \\ & \left[M_{11}^2 + M_{22}^2\right]\hat{\mathbb{A}}_{44} + 2M_{11}M_{22}\hat{\mathbb{A}}_{45} + M_{12}^2\hat{\mathbb{A}}_{66} \end{aligned} \tag{5.92}$$

What we can simplify further is the tangent modular matrix in Equation (5.44) expressed specifically for resultants plasticity. This matrix takes a remarkably simple form as a result of a null sub–matrices and symmetry of matrices we have encountered in this section. With the simplified surface, the corresponding symmetric matrix of compliance $\bar{\mathbb{H}}_{n+1}$ from Equation (5.38) is completely described by the components,

$$\bar{\mathbb{H}}_{11} = \bar{\mathbb{V}}_{11}\bar{\mathbb{C}}_{11} + \bar{\mathbb{V}}_{12}\bar{\mathbb{C}}_{12} \qquad \bar{\mathbb{H}}_{44} = \bar{\mathbb{V}}_{44}\bar{\mathbb{C}}_{44} + \bar{\mathbb{V}}_{45}\bar{\mathbb{C}}_{45} \tag{5.93}$$

$$\bar{\mathbb{H}}_{12} = \bar{\mathbb{V}}_{11}\bar{\mathbb{C}}_{12} + \bar{\mathbb{V}}_{12}\bar{\mathbb{C}}_{11} \qquad \bar{\mathbb{H}}_{45} = \bar{\mathbb{V}}_{44}\bar{\mathbb{C}}_{45} + \bar{\mathbb{V}}_{45}\bar{\mathbb{C}}_{44} \tag{5.94}$$

$$\bar{\mathbb{H}}_{33} = \bar{\mathbb{V}}_{33}\bar{\mathbb{C}}_{33} \qquad \bar{\mathbb{H}}_{66} = \bar{\mathbb{V}}_{66}\bar{\mathbb{C}}_{66} \tag{5.95}$$

URN:NBN:no-1282

with $\bar{\mathbb{H}}_{22}$ equal to $\bar{\mathbb{H}}_{11}$ and $\bar{\mathbb{H}}_{55}$ equal to $\bar{\mathbb{H}}_{44}$. Then, if we define a vector $\mathbb{R} = \bar{\mathbb{H}}\bar{\boldsymbol{n}}$ and its components to be expressed as,

$$\mathbb{R}_1 = \bar{\mathbb{H}}_{11}\bar{\boldsymbol{n}}_1 + \bar{\mathbb{H}}_{12}\bar{\boldsymbol{n}}_2 \qquad \mathbb{R}_2 = \bar{\mathbb{H}}_{12}\bar{\boldsymbol{n}}_1 + \bar{\mathbb{H}}_{11}\bar{\boldsymbol{n}}_2 \qquad \mathbb{R}_3 = \bar{\mathbb{H}}_{33}\bar{\boldsymbol{n}}_3 \tag{5.96}$$

$$\mathbb{R}_4 = \bar{\mathbb{H}}_{44}\bar{\boldsymbol{n}}_4 + \bar{\mathbb{H}}_{45}\bar{\boldsymbol{n}}_5 \qquad \mathbb{R}_5 = \bar{\mathbb{H}}_{45}\bar{\boldsymbol{n}}_4 + \bar{\mathbb{H}}_{44}\bar{\boldsymbol{n}}_5 \qquad \mathbb{R}_6 = \bar{\mathbb{H}}_{66}\bar{\boldsymbol{n}}_6 \tag{5.97}$$

in which,

$$\bar{\boldsymbol{n}} = 2\boldsymbol{A}\bar{\boldsymbol{\sigma}} \tag{5.98}$$

the consistent tangent modular matrix for resultants plasticity is simplified to,

$$\bar{\mathbb{C}}_t = \bar{\mathbb{H}} - \frac{\mathbb{R}\mathbb{R}^T}{\bar{\boldsymbol{n}}^T\mathbb{R} + \bar{\beta}} \tag{5.99}$$

where,

$$\bar{\beta} = \frac{2\bar{\alpha}\bar{\sigma}}{1 - \bar{\alpha}\lambda/\bar{\sigma}} \qquad \bar{\sigma} = \sqrt{\bar{\boldsymbol{\sigma}}^T\boldsymbol{A}\bar{\boldsymbol{\sigma}}} \tag{5.100}$$

5.5.5 Yield Stress Control

As mentioned in Section 5.5.3, the modification of the Ilyushin yield surface by setting $\mu = 0$, introduces an overestimation as compared to the unmodified surface. With reference to Figure 5.4, it can be shown that this overestimation can be controlled if the plasticity calculations are based on the reduced yield stress given by,

$$\sigma_\circ^{red} = \sigma_\circ(1 - r) \tag{5.101}$$

where r is the reduction factor. It can be readily seen that this reduction is higher with combined membrane and bending situations, but vanishes otherwise.

A quick solution to the control of this envelope would be to set a constant factor between 0—0.12 that will be used throughout the analysis. This must be based on a prior knowledge of the problem. Another alternative which may turn out to require more computer time would be an automatic reduction. Both, analytical and numerical investigations have shown that it is possible to approximate the reduction factor by a polynomial function $r(x)$, where x stands for either $\bar{M}/m_\circ$ or $\bar{N}/n_\circ$.

Applying a polynomial for stress reduction is equivalent to introducing an infinite number of hyperelliptic yield surfaces between the two boundaries — i.e. upper and lower. The upper surface corresponds to $r = 0$ while the lower one corresponds to $r = 0.12$ for balanced membrane–bending interaction. The value of r is calculated as a ratio of the distance between the two surfaces to the distance from the origin. It is pointing in the radial direction. A curve fitting gives the following polynomial,

$$r(x) = 0.272x + 0.042x^2 - 1.231x^3 + 3.567x^4 - 4.519x^5 + 1.995x^6 \tag{5.102}$$

URN:NBN:no-1282

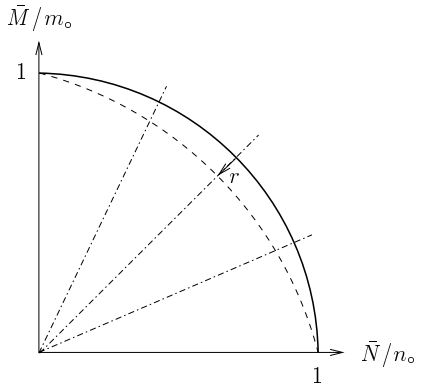

Figure 5.4 Yield stress control.

where when $f(\lambda) = 0$,

$$x = \begin{cases} \bar{N}/n_\circ & \text{for} \quad \bar{M}/m_\circ \geq 1/\sqrt{2} \\ \bar{M}/m_\circ & \text{for} \quad \bar{N}/n_\circ \geq 1/\sqrt{2} \end{cases} \tag{5.103}$$

in which $n_\circ$ and $m_\circ$ are calculated before the reduction and recalculated thereafter.

Equation (5.102) is applicable only when the stress resultants are based on the proposed new surface. With the reduced yield stress, the stress resultants are evaluated at the unmodified Ilyushin surface using a reduced hyperellipse surface. The corrected trial stress resultants based on the reduced yield stress are used to recalculate the consistency parameter λ. This implies that the nonlinear equation need to be solved twice if the automated yield stress reduction is used.

URN:NBN:no-1282

Chapter 6

Nonlinear Solution and Numerical Examples

6.1 Introduction

The governing equations for the discretized geometric nonlinear problem have been derived in Chapters 3 and 4. The result is a set of parametrized nonlinear algebraic equations called residuals which are analogous to Equation (2.4). The solution of these equations as the control parameters are varied provide an equilibrium path of response. This path is typically achieved by Newton's method whereby a sequence of linear problems are solved.

If the linear problems are obtained by consistent linearization of the nonlinear problem, a quadratic rate of asymptotic convergence to the nonlinear problem is guaranteed. It is, therefore, generally assumed that the solution procedure of practical importance is based on advancing the solution by continuation. The basic idea in this process is that the equilibrium response of the structure is followed as the control and state parameters varies by small amounts.

The continuation process is a multilevel one and involves a hierarchical breakdown into stages, incremental and iterative steps. The incremental steps are always present and make the major part of the continuation. Stages are related to each other in the sense that the end of one solution may provide the starting point for the next. In a single stage, incremental and, if desired, iterative steps are performed. Iterative or rather corrective steps are used to reduce or eliminate the so–called drift error which is accumulated during incremental steps.

Usually, an equilibrium response obtained by continuation reaches a maximum load level (or state) commonly known as the *critical* point. This point is illustrated in Figure 6.1, and it is characterized by a singular stiffness matrix. The critical point is said to be a *limit*

URN:NBN:no-1282

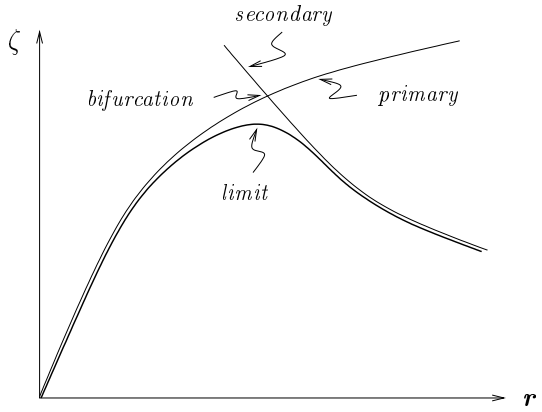

Figure 6.1 A typical bifurcation example.

point if it is smooth, or a *bifurcation* point if it is sharp. The latter can be avoided by introducing initial imperfection in the finite element modelling.

The limit point is associated with snapping, and the bifurcation point is an indication of buckling where the response curve switches from the primary to the secondary equilibrium path. More precisely, bifurcation is a point where more than one equilibrium path exist. In some cases, the equilibrium path goes through a *turning* point where the tangent stiffness becomes infinity in transition from negative to positive or vice versa.

The main difficulty in advancing the solution by continuation is the traversal of critical and turning points. These make the choice of incremental control of great importance. Usually, the equilibrium response is traced using either load control, displacement control, or their combination. Up to mid–seventies, nonlinear problems were solved with purely incremental methods under load control. However, the procedure causes the computed solution to drift away from the equilibrium path unless the size of incremental steps are kept very small.

Following the invention of corrective methods, the shortcoming of the drift error accumulation was overcome by iterating the solution back to the equilibrium path. As long as it converges, the solution is independent of the incremental step size. However, even if the load control is associated with iterative steps, it has the problem of traversing the critical points. As an alternative, the displacement control algorithm can be used, but it has the problem of traversing turning points.

In the past two decades, improvements have been made that allow loads and displacements to be varied simultaneously. These incremental controls are widely discussed in the literature and they include the arc–length control of Riks (1972) and Wempner (1971), and the hyperplane displacement control of Simons *et al.* (1984). Unfortunately, none of these improvements are best for all problems. However, the arc–length type algorithms are considered the most versatile in terms of the range of problems they can solve.

In this thesis, the arc–length incremental control is used as the projector step. During

URN:NBN:no-1282

the iterative steps, either the so–called normal plane iterations or the orthogonal trajectory iterations is used. Each of these methods is discussed in the following sections.

6.2 The Solution Procedure

The equilibrium response or equilibrium path, which is usually presented in a load–displacement diagram, says more about the structural behavior than just knowing the final solution. The response path includes physical actions such as snapping and buckling. This response curve is normally obtained by continuation method.

In Chapter 2, we have presented what we called the residual equations of nonlinear equilibrium equations. Repeating here for convenience, it can be written as

$$\boldsymbol{\rho}(\boldsymbol{r},\zeta) = \boldsymbol{f}(\boldsymbol{r}) - \boldsymbol{p}(\zeta) = \boldsymbol{0} \tag{6.1}$$

where the control parameters are the displacement vector $\boldsymbol{r}$ and the external load intensity ζ. For proportional conservative loading, the external load vector can be expressed as,

$$\boldsymbol{p} = \zeta \bar{\boldsymbol{p}} \tag{6.2}$$

where $\bar{\boldsymbol{p}}$ is the constant vector of the actual external loads. Gradual variation of the independent control parameters, or precisely the linearization of the residual Equation (6.1), allow many solution points to be calculated and the equilibrium path be traced through them.

What appears to be a formidable task, is the implementation of a solution procedure which is capable of tracing and traversing the *bifurcation* points and switch the solution to the secondary equilibrium path. Alternatively, bifurcation points can always be transferred to limit points by introducing small geometric imperfections. In this way, the correct equilibrium path can be asymptotically followed by avoiding to hit the bifurcation point. Practically, this is the natural approach for solving problems in structural mechanics. This is mainly due to the fact that structures are rarely ideal and geometric imperfections do always exist making the bifurcation points only hypothetical.

The variation of the residual Equation (6.1) can be expressed as,

$$\delta\boldsymbol{\rho} = \frac{\partial \boldsymbol{f}}{\partial \boldsymbol{r}}\frac{\partial \boldsymbol{r}}{\partial \zeta}\delta\zeta - \frac{\partial \boldsymbol{p}}{\partial \zeta}\delta\zeta = [\boldsymbol{K}_t\bar{\boldsymbol{w}} - \bar{\boldsymbol{p}}]\,\delta\zeta = \boldsymbol{0} \tag{6.3}$$

where $\boldsymbol{K}_t$ is the tangent stiffness matrix and $\bar{\boldsymbol{w}}$ is the so–called incremental velocity vector. This representation has been conveniently used by Felippa (1996). Since $\delta\zeta$ is arbitrary, we can write,

$$\boldsymbol{K}_t\bar{\boldsymbol{w}} - \bar{\boldsymbol{p}} = \boldsymbol{0} \tag{6.4}$$

Equation (6.4) can be solved for the incremental velocity vector $\bar{\boldsymbol{w}}$ and the results be applied over a finite increment $(\Delta\boldsymbol{r}, \Delta\zeta)$ instead of virtual increments in Equation (6.3).

URN:NBN:no-1282

This procedure provides the incremental control variable with a possible drift error. The error can be eliminated by performing corrective iterations. With finite increments, the incremental displacement vector can be obtained from the velocity vector as,

$$\Delta \boldsymbol{r} = \bar{\boldsymbol{w}} \Delta \zeta \tag{6.5}$$

6.2.1 The Arc–length Method

The arc–length method was originally proposed by Riks (1972) and Wempner (1971) and it was developed further by Riks (1979). This method is commonly known as the Riks–Wempner algorithm and it adds to the standard equilibrium equations a constraint equation. The constraint fixes the size of incremental steps by prescribing the tangent of equilibrium path at the previously converged solution. Following the modifications introduced by Crisfield (1982) and Ramm (1982), the Riks–Wempner algorithm was made suitable for finite element method.

The arc–length method allows both loads and displacements to be incremented simultaneously and as long as the increments are small enough, the system equations become singular only at bifurcation points. Therefore, limit points can be passed without difficulties. Before proceeding, let a normalized tangent vector along the equilibrium path be defined as,

$$\boldsymbol{t}_u = \frac{1}{f} \begin{bmatrix} \bar{\boldsymbol{w}} \\ 1 \end{bmatrix} \qquad\qquad f = \sqrt{1 + \bar{\boldsymbol{w}}^T \bar{\boldsymbol{w}}} \tag{6.6}$$

where f is the scaling factor.

An arc–length method which is discretization independent has been presented by Haugen (1994). Its main advantage is that the actual displacement increment which matches a normalized prescribed arc–length f is not influenced by mesh refinement. In this procedure, a change in the arc–length definition is introduced by scaling the norm of the incremental velocity vector $\bar{\boldsymbol{w}}^T \bar{\boldsymbol{w}}$ with the number of nodes in the element mesh. In addition to this special scaling of displacements, the loads are scaled as well. With the latter modification, the magnification of the actual applied loads does not change the actual step size of the path following algorithm.

For the present work, it is chosen to employ the scaling technique for the displacements only. However, instead of scaling with the number of nodes in the element mesh we shall rather use the number of equations in the system which is equal to the number of free degrees of freedom. The main reason behind this decision is that the element nodes in this thesis do not have an equal number of degrees of freedom.

The predictor step

The equilibrium path is a curve in $N + 1$ dimensional space with an unknown vector involving $\boldsymbol{r}$ and ζ. In the finite element method, the arc–length method is a two step

URN:NBN:no-1282

procedure involving matrices of order N. Within a continuing solution, we start from a converged solution at step n and predict the solution at step $n+1$. Between these two steps, a number iterations can be performed to bring the solution back to the equilibrium path.

The exact load and displacement increments to be added to the structure are initially not known. However, the approximation of the load intensity — which in turn gives the approximate displacements from Equation (6.5) — can be obtained from the constraint equation given by,

$$\Delta s = \sqrt{\Delta\zeta^2 + \frac{1}{n_d}\Delta \boldsymbol{r}^T \Delta \boldsymbol{r}} \tag{6.7}$$

where Δs is the prescribed arc–length and $\Delta\zeta$ is the load increment. Note that, following the discussion is Section 6.2.1, we have introduced the scaling factor n_d equal to the number of free degrees of freedom.

The incremental velocity vector $\bar{\boldsymbol{w}}_\circ$ is predicted by solving Equation (6.4). When the result is submitted to Equation (6.5) followed by substitution into (6.7), it provides the approximate load increment as,

$$\Delta\zeta = \pm \frac{\Delta s}{\sqrt{1 + \frac{1}{n_d}\bar{\boldsymbol{w}}_\circ^T \bar{\boldsymbol{w}}_\circ}} \tag{6.8}$$

The sign of $\Delta\zeta$ is determined by assuming that the equilibrium path is smooth, and in tracing this path the present predictor must form a positive vector with the previous predictor. Alternatively, we could use the so–called positive external work criteria.

The complete incremental–iterative algorithm for arc–length method is summarized in Table 6.1. To maintain an approximately equal number of iterations at each load increment, an automatic scaling factor is applied to account for special circumstances,

$$\xi = \sqrt{\frac{I_d}{I_n}} \qquad\qquad I_n > I_d \tag{6.9}$$

where I_d and I_n are, respectively, the desired number of iterations at any incremental step and the number of iterations in the previous converged solution. This scaling appears to have been introduced by Providas (1990). It allows the magnitude of load increments to be reduced automatically when severe nonlinearities occur.

A purely incremental solution with arc–length control, which avoids the corrective step, is explained by Felippa (1996). By monitoring the numerical accuracy and stability, the method introduces a special automatic adjustment of incremental load. This procedure has been used during the early stages in the preparation of this thesis and has proved to be very robust.

The corrector step

Having obtained the predictor increment $(\Delta\boldsymbol{r}, \Delta\zeta)$, the next step is to correct it for the drift error. With reference to Figure 6.2, this is achieved by assuming that the shortest

URN:NBN:no-1282

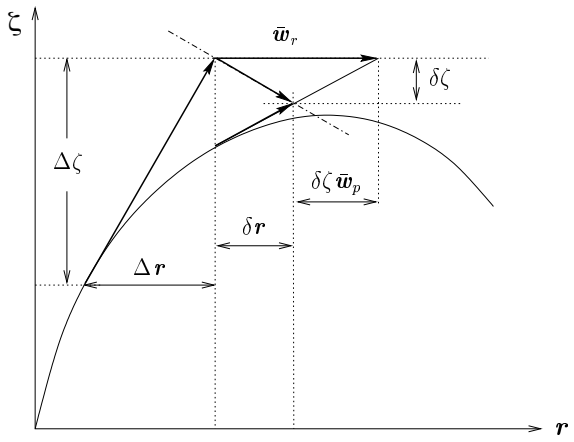

Figure 6.2 Normal plane iterations.

distance to the equilibrium path lies in the direction orthogonal to the predictor increment.

Since the normal plane to the predictor is a hyperplane, subsequent corrector iterations are forced to be on that surface. In doing so, the solution is decomposed into two contributions — one due to the incremental load solution, and the other due to the residual solution which is the cause of the drift error. In other words, one solves for a set of two equations involving,

$$\boldsymbol{K}_t\,\bar{\boldsymbol{w}}_p = \bar{\boldsymbol{p}} \tag{6.10}$$

$$\boldsymbol{K}_t\,\bar{\boldsymbol{w}}_r = -\boldsymbol{\rho} = \boldsymbol{p} - \boldsymbol{f} \tag{6.11}$$

with a combined solution given in augmented form as,

$$\begin{bmatrix}\delta\boldsymbol{r}\\ \delta\zeta\end{bmatrix} = \begin{bmatrix}\bar{\boldsymbol{w}}_p\\ 1\end{bmatrix}\delta\zeta + \begin{bmatrix}\bar{\boldsymbol{w}}_r\\ 0\end{bmatrix} \tag{6.12}$$

Forcing the iteration path to follow a plane normal to the tangent of the equilibrium path is equivalent to introducing the constraint,

$$\frac{1}{n_d}\Delta\boldsymbol{r}^T\delta\boldsymbol{r} + \Delta\zeta\delta\zeta = 0 \qquad \Longrightarrow \qquad \frac{1}{n_d}\boldsymbol{w}_\circ^T\delta\boldsymbol{r} + \delta\zeta = 0 \tag{6.13}$$

where $\delta\boldsymbol{r}$ and $\delta\zeta$ are the iterative increments. By substituting the augmented Equation (6.12) into (6.13), the iterative load increment is obtained as,

$$\delta\zeta = -\frac{\bar{\boldsymbol{w}}_\circ^T\bar{\boldsymbol{w}}_r}{\bar{\boldsymbol{w}}_\circ^T\bar{\boldsymbol{w}}_p + n_d} \tag{6.14}$$

It has been established by Haugen (1994) that the *orthogonal trajectory* iterations of Fried (1984) are more effective than the normal plane iterations. This method was

URN:NBN:no-1282

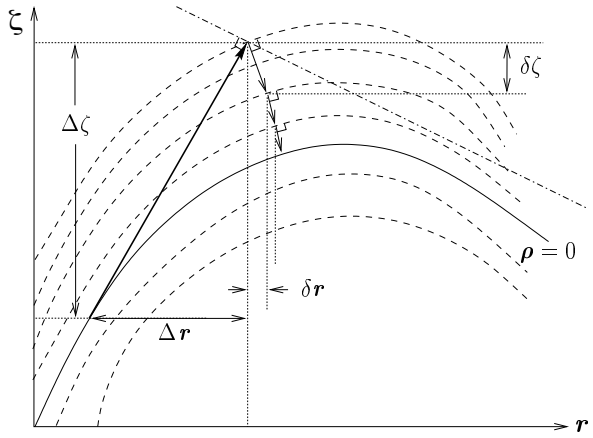

Figure 6.3 Orthogonal trajectory iterations.

originally developed as a means of inducing convergence to an equilibrium state from an arbitrary starting configuration.

The orthogonal trajectory procedure is illustrated in Figure 6.3 and its main theme is that the normality to the hyperplane is renewed at each subsequent iteration. More precisely, the combined iterative solution is forced to be orthogonal to the incremental flow at the current non–equilibrium path. Consequently, the corresponding iterative load increment is given by,

$$\delta\zeta = -\frac{\bar{\boldsymbol{w}}_p^T \bar{\boldsymbol{w}}_r}{\bar{\boldsymbol{w}}_p^T \bar{\boldsymbol{w}}_p + n_d} \tag{6.15}$$

This iteration procedure is the default in the computer program developed along with this thesis. Among its advantages is that it allows larger increments than what would have been possible with the normal plane iterations. The procedure has less possibility of missing a critical point.

The convergence criterion

As usual for incremental–iterative solutions, the criterion for stopping the iterations need to be set. The desired outcome is that the solution converges according to the minimum tolerance requirement. However, it may also happen that the solution diverges or oscillations take place. In this situation, the analysis is terminated when the desired maximum number of iterations has been exceeded.

For checking iteration convergence, there exist several criteria. These include displacement norms, residual norms, energy norms, etc. If the displacement criterion is used,

URN:NBN:no-1282

Table 6.1 Arc–length algorithm

Incremental step.

Solve $\boldsymbol{K}_t(\boldsymbol{r}_n)\bar{\boldsymbol{w}}_\circ = \bar{\boldsymbol{p}}$ to get $\bar{\boldsymbol{w}}_\circ$
Set $f = \sqrt{1 + \frac{1}{n_d}\bar{\boldsymbol{w}}_\circ^T \bar{\boldsymbol{w}}_\circ}$
Find $\mu = \bar{\boldsymbol{w}}_\circ^T \bar{\boldsymbol{p}}$ or $\mu = \bar{\boldsymbol{w}}_\circ^T \Delta \boldsymbol{r}_n$
Define $\Delta\zeta = \frac{\mu}{|\mu|}\frac{\Delta s}{f}\xi$
Set $\Delta \boldsymbol{r} = \Delta\zeta \bar{\boldsymbol{w}}_\circ$
Update $\zeta_{n+1} = \zeta_n + \Delta\zeta$
Update $\boldsymbol{r}_{n+1} = \boldsymbol{r}_n + \Delta \boldsymbol{r}$

Iterative step.

$i = 1$
Do while $TOL < \epsilon$
  Find $\bar{\boldsymbol{w}}_p$ and $\bar{\boldsymbol{w}}_r$ by solving (6.10) and (6.11)
  Find $\delta\zeta$ from (6.14) or (6.15)
  Set $\delta \boldsymbol{r} = \bar{\boldsymbol{w}}_p \delta\zeta + \bar{\boldsymbol{w}}_r$
  Update $\zeta^{i+1} = \zeta^i + \delta\zeta$
  Update $\boldsymbol{r}^{i+1} = \boldsymbol{r}^i + \delta \boldsymbol{r}$
  $i = i + 1$
Continue until criterion ϵ is fulfilled.

the convergence is monitored by the Euclidean norm such that,

$$\frac{1}{n_d}\|\delta \boldsymbol{r}^T \delta \boldsymbol{r}\| = \epsilon_r < TOL \tag{6.16}$$

where n_d is the number of *free* degrees of freedom and TOL is a predefined tolerance for solution convergence. For the residual force criterion, the Euclidean norm is given by,

$$\|\boldsymbol{\rho}^T \boldsymbol{\rho}\| = \epsilon_\rho < TOL \tag{6.17}$$

The residual energy can be considered as a compromise between the displacement and residual force criteria. It avoids the so–called scaling problems by adopting a unique Unit of energy for both translational and rotational degrees of freedom. The convergence is monitored against the tolerance given by,

$$\delta \boldsymbol{r}^T \boldsymbol{\rho} = \epsilon_e < TOL \tag{6.18}$$

The choice of convergence criterion and its tolerance limit is of crucial importance in traversing the equilibrium path. For the majority of problems, monitoring by residual energy can be the best choice. In setting the magnitude of tolerance requirement, however, special considerations need to taken. For instance, a too strict threshold will do no better than just increasing the computational time unnecessarily. A loose convergence threshold, on the other hand, may not provide sufficient accuracy and soon or later it may induce divergence due to accumulated drift error.

URN:NBN:no-1282

6.3 Implementation and Numerical Examples

All formulations presented in this thesis have been implemented in a stand–alone computer program NSHEL (2000). This code has been developed along with several independent packages for mesh generation and input file processing. A number of packages from SAM library (Bell 1997) have been used for assembly and solution of the system equations. Among other things, the output includes a complete GLView (1999) file in a VTF format for graphical presentation. By using this file, the structural response in terms of deformations and stress levels can be viewed as either a video or a still picture.

In this section, numerical examples are presented to demonstrate the performance of the foregoing formulations. Since it is not possible to present each and every benchmark problem that has been solved during the present thesis, only a selected number of examples are presented. Unless specifically mentioned, the stress resultants plasticity formulation is used in the analysis.

6.3.1 Elastic Problems

Before looking into the performance of the material formulation, it is important to check that the element formulation and the solution procedure work well in the elastic range. In that respect, two problems which have been widely used as benchmarks are presented. They represent a hinged cylindrical shell problem, and a plate cantilever subjected to pure bending. Both problems involve only geometric nonlinearity.

Hinged cylindrical shell

The circular cylindrical shell of Sabir and Lock (1972) has been widely used as a benchmark problem in testing nonlinear shell formulations. The geometry is shown in Figure 6.4 with $t = 12.7$mm, $R = 2540$mm, $L = 254$mm, and $\theta = 0.1$ radian. The elastic material is characterized by $E = 3.10275 \times 10^3$MPa, and $\nu = 0.3$. The two longitudinal straight edges are fixed against all possible translations while the curved boundaries are kept free.

The nonlinear response of this example involves a deep snap–through. This feature makes it not only a test for geometric nonlinearity, but for robustness of the solution procedure as well. The structure is subjected to a concentrated vertical force at the center. Due to double symmetry in geometry and loading, only one quarter of the shell is modelled as depicted in Figure 6.4. The finite element mesh involves 124 triangular elements.

The results are presented in Figure 6.5 along with the results by Sabir and Lock (1972), Horrigmoe and Bergan (1978), and Meek and Tan (1986). Both elements presented in Chapters 3 and 4 have been used. The curves from the two elements lie almost over each other. The results correspond very well with other publications. A point should be mentioned that, for shell problems, the Morley element is softer with coarse mesh. This implies that improved results can be obtained with a finer mesh. The same observation

URN:NBN:no-1282

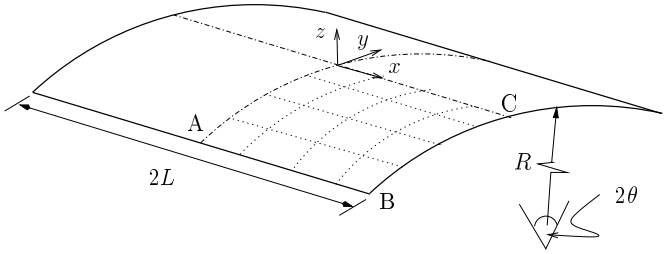

Figure 6.4 Cylindrical shell; Geometry.

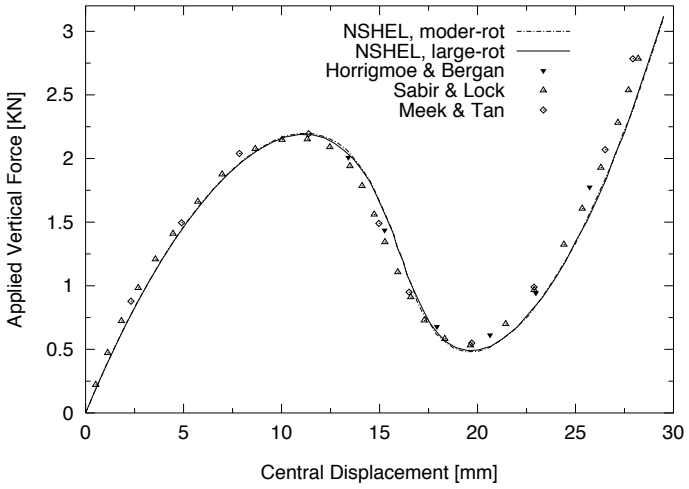

Figure 6.5 Response of hinged cylindrical shell ($t = 12.7$mm).

was made in a study by Providas (1990) while analyzing shell structures. Due to identical results for moderate and large rotation elements, the example can be said to be in the range of moderate rotations.

When the thickness of this cylindrical shell is reduced by one–half, so that $t = 6.35$mm is used, the structural response becomes quite different from the one in Figure 6.5. In this case, the response involves a dramatic snap–back behaviour. It is, therefore, a suitable example for verifying path following capabilities of a solution algorithm. From the results in Figure 6.6, it can be observed that the performance of the present formulations is of the same quality as in the previous example.

Cantilever subjected to an end moment

In the previous example, the performance of the elastic formulations within the range of moderate rotations were tested. In this example, the performance within arbitrary large

URN:NBN:no-1282

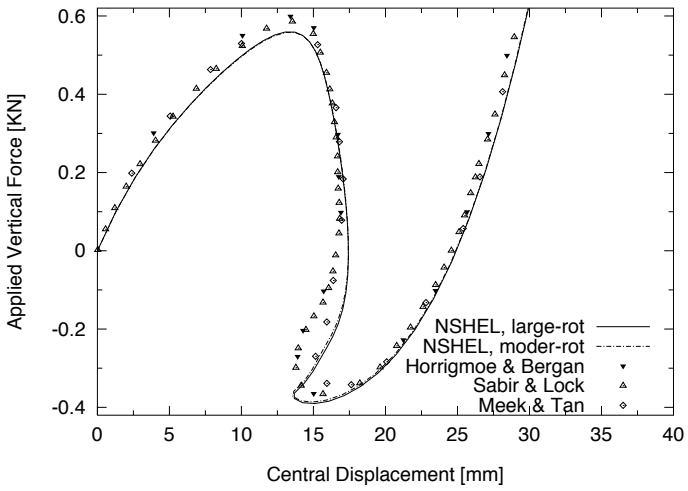

Figure 6.6 Response of hinged cylindrical shell ($t = 6.35$mm).

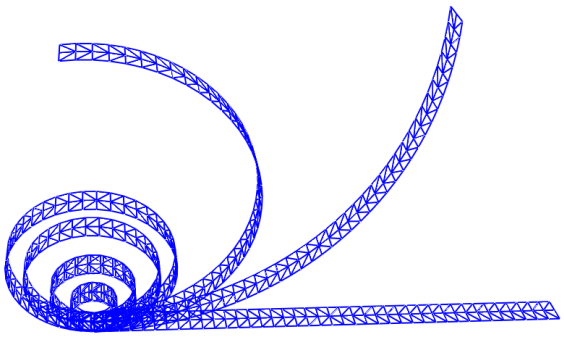

Figure 6.7 Cantilever under pure bending.

displacements and rotations is studied. Bending of an elastic cantilever subjected to an end moment is considered (Figure 6.7). This is a common benchmark problem for which analytical solution exists.

Under pure bending, the beam should respond without membrane stresses. However, many finite element formulations are subjected to *membrane locking* and either fail completely or give erroneous results. In those cases, they usually give over–stiff solutions once the beam reaches a half–cylinder shape. In this analysis, the large rotation element presented in Chapter 4 is used.

The analytical solution for the end moment is given by,

$$M = \frac{1}{12}\frac{E}{(1-\nu^2)}\frac{t^3}{L}\vartheta \tag{6.19}$$

URN:NBN:no-1282

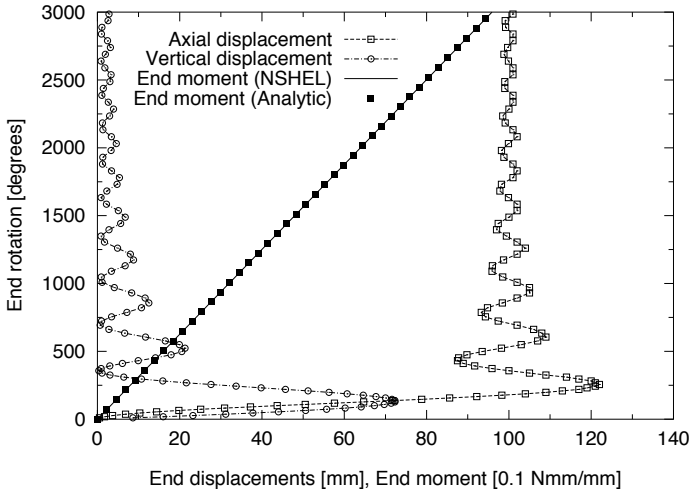

Figure 6.8 Elastic response of a cantilever under pure bending.

where ϑ is the end rotation, L is the length, t is the thickness, E is the Young's modulus, and ν is the Poisson's ratio. Usually, there are no common dimensions for this problem. In the present case, a beam having dimensions such that $L = 100$, $b = 5$, and $t = 1$ is analyzed. The elastic material is described by $E = 200$ and $\nu = 0.3$.

The beam is folded up to 10 times before the solution fails, and the selected circles are shown in Figure 6.7. The response is shown in Figure 6.8. It is observed that the end rotations from the analysis correspond remarkably well with the analytical solution.

6.3.2 Elasto–Plastic Plate Problems

The examples in Section 6.3.1 indicate that the elastic formulations and numerical solution presented in Chapters 3–4 and 6 perform very well. The next task is to verify the performance of the plasticity model as presented in Chapter 5. In the present section, several examples on elasto–plastic plate bending, buckling, and torsion analysis are presented. Examples involving problems on shell collapse are given in the next section.

Bending

A simply supported square plate subjected to a distributed pressure loading is analyzed. This example was introduced by Levy (1942), and it demonstrates high membrane effects in the post–yield range. With reference to Figure 6.9, the plate geometry is described by side lengths $a = b = 407$mm and thickness $t = 2.54$mm. This gives a width to thickness ratio $b/t = 160$. In this case the initial axial load is equal to zero. The material is assumed

URN:NBN:no-1282

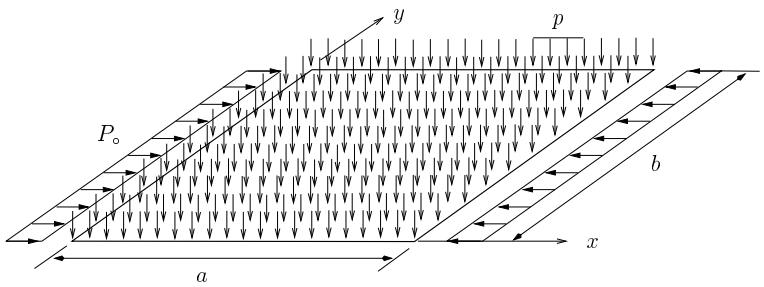

Figure 6.9 Plate loading and geometry.

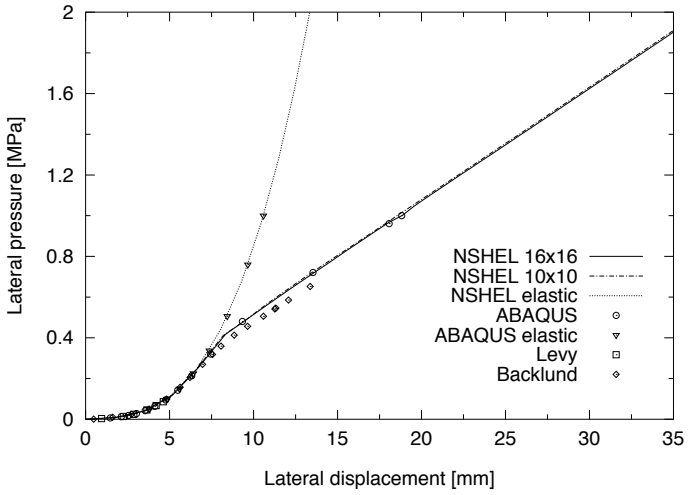

Figure 6.10 Response of a simply–supported square plate.

to be elastic–perfectly plastic with $E = 2.11 \times 10^5$MPa, $\nu = 0.316$, $\sigma_\circ = 248$MPa and $H = 0$.

The plate is fixed against translations along all four edges and a full model is analyzed. Both, elastic and elasto–plastic analyses are considered. The finite element model uses the large rotation element from Chapter 4. The results are shown in Figure 6.10 along with ABAQUS (1998) predictions, and the results by Levy (1942) and Bäcklund (1973).

Bäcklund used integration through thickness on an element having the same degrees of freedom as the present element. Levy analyzed this plate up to about 5mm of lateral displacement which is in the elastic range. Very good correspondence with other simulations is observed, and the evidence of pure membrane effects in the post–yield range is very clearly seen. The deformed model and stress distribution in the post–collapse range are shown in Figure 6.11.

URN:NBN:no-1282

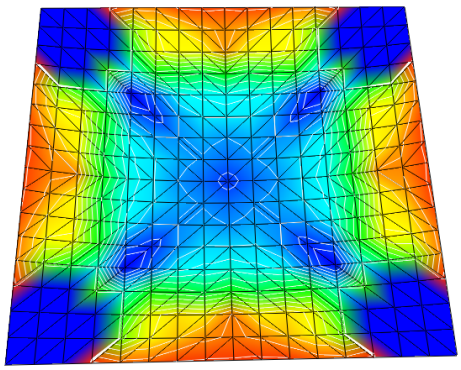

Figure 6.11 Stress distribution of the square plate.

Buckling

An imperfect plate, which was introduced by Javaherian and Dowling (1985) and studied also by Nygård (1986), is analyzed in this example. It involves elasto–plastic buckling of a simply supported short rectangular plate. The longitudinal edges are transversely free. With reference to Figure 6.9, the geometry is described by the aspect ratio $a/b = 0.875$, slenderness $b/t = 80$ and thickness $t = 3.175$mm. The material is assumed to be elastic–perfectly plastic with $E = 2.062 \times 10^5$MPa, $\nu = 0.3$, $\sigma_\circ = 250$MPa and $H = 0$. Moderate rotation element is used.

The loading involves proportional increments of the prescribed uniform axial displacements at one of the longer edge of the plate. The lateral distributed load is absent in this case. The initial imperfection is described by a single sine wave in both directions with a maximum amplitude of $w_p = 0.001b$ at the plate center.

Both, elastic and elasto–plastic analyses are considered. The results shown in Figure 6.12, display a very good agreement to those of Nygård (1986) (see also Bergan *et al.* (1990)), and are close to that of Javaherian and Dowling (1985).

In another buckling problem, we again consider imperfect plate with two aspect ratios of $a/b = 1$, and $a/b = 3$. With reference to Figure 6.9, the geometry is defined by $b = 240$mm and $t = 4$mm. The material properties are $E = 2.05 \times 10^5$Mpa, $\sigma_\circ = 245$MPa, $\nu = 0.3$, and $H = 0$. An initial single wave sinusoidal imperfection with a maximum amplitude of $w_p = 1.5t$ is introduced. Moderate rotation element is used.

A uniformly distributed axial load, equivalent to $P_\circ = \sigma_\circ t$, is applied at the shorter side of the plate. Again, there is no distributed lateral load in this example. The results for different mesh densities are shown in Figure 6.13. They are given as normalized load versus normalized axial strain, and are compared to the predictions of an eight–node rectangular ABAQUS element.

Excellent agreement is obtained with an expected deviation at the ultimate load for $a/b = 3$. The overestimation is attributed to the different plasticity formulations used.

URN:NBN:no-1282

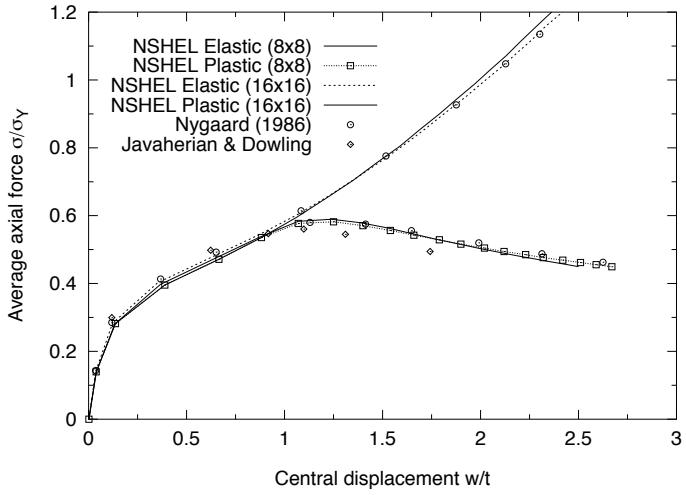

Figure 6.12 Rectangular plate buckling (I).

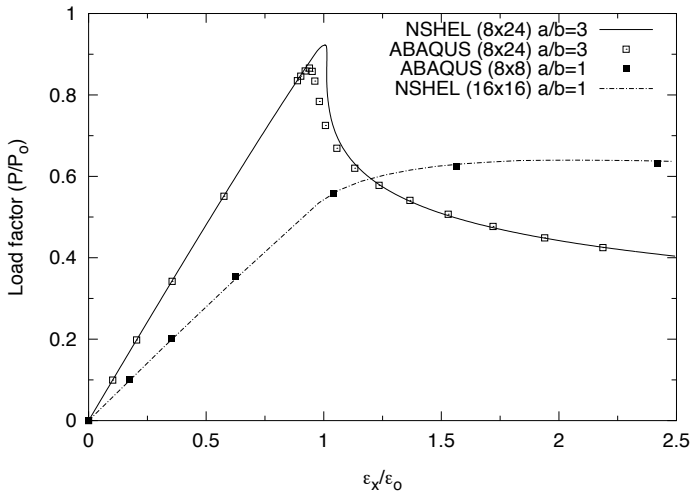

Figure 6.13 Rectangular plate buckling (II).

While (for this example) NSHEL uses the modified resultant plasticity, ABAQUS uses 5 integration points over the thickness. The deviation is less pronounced for $a/b = 1$. As far as the present resultants plasticity is concerned, these results support the previous demonstration in Section 5.5.5. It was said that the overestimation is larger with combined membrane and bending situations, and it vanishes for pure bending or membrane actions.

URN:NBN:no-1282

Torsion

The torsion of a plate sheet with a hole at the center has been presented recently in a paper by Başar and Itskov (1999). It has an aspect ratio of $a/b = 5$ with geometry defined by $a = 5$ and $t = 0.05$. The material with isotropic hardening is described by $E = 210$, $\nu = 0.2$, $\sigma_\circ = 0.2$ and $H = 3$. The circular hole has a radius of $r = 0.15$. The sheet has rigid ends, and it is clamped on one end. On the other end, the axial translations are restrained and a concentrated twisting moment is applied at the middle of this end. Large rotation element is used.

The characteristic moment–rotation diagram for the twisted end is plotted in Figure 6.14 along with the results by Başar and Itskov (1999) and Skallerud *et al.* (2001). The plate is twisted up to a rotation angle equal to 180° as shown in Figure 6.15.

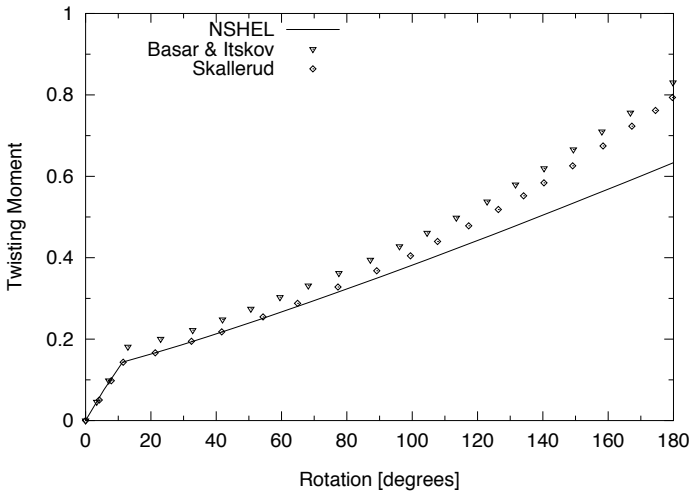

Figure 6.14 Response of plate under twisting moment.

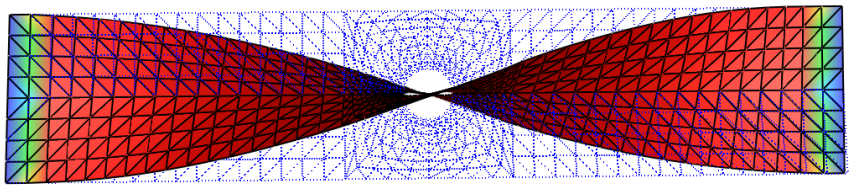

Figure 6.15 Plate with circular hole; Deformed model.

URN:NBN:no-1282

6.3.3 Elasto–Plastic Shell Problems

Pinched cylinder

This example was introduced by Simo and Kennedy (1992) who used the generalized Ilyushin–Shapiro material model formulated entirely in stress resultants. Since then, it has also been studied by Brank *et al.* (1997) using von Mises material and seven integration points through thickness, and by Skallerud and Haugen (1999) using stress resultant plasticity formulation similar to the present one. In this problem, the short cylinder is pinched by two concentrated forces at its mid–section, and it is bounded by two rigid diaphragms at its ends (see Figure 6.16). The analysis represents a complex distribution of shell stresses.

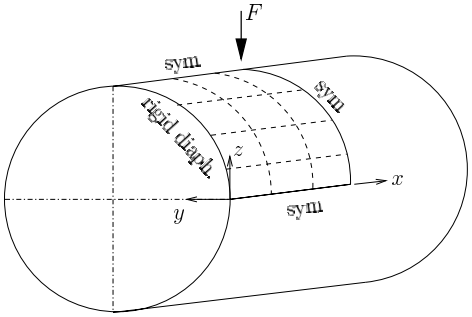

Figure 6.16 Pinched cylinder; Geometry.

The geometry of the cylinder is described by the length $L = 300$, thickness $t = 3$, and radius $R = 300$. The material is characterized by an isotropic hardening plastic response with $E = 3000$, $\nu = 0.3$, $\sigma_\circ = 24.3$ and hardening $E_h = 50$. This hardening value is different from the isotropic hardening modulus H used in the present formulation. Therefore, an equivalent value based on a tensile test simulation using the stress resultant model is used instead. In this way, the uniaxial hardening modulus is applied indirectly.

One octant of the cylinder is analyzed with the boundary conditions described in Figure 6.16. Large rotation element is used. The results are shown in Figure 6.17 along with those presented by Skallerud and Haugen (1999), Simo and Kennedy (1992) and Brank *et al.* (1997). The simulation by Brank *et al.* (1997) considers the out–of–plane shear deformations and thickness update, and may therefore be considered to be the most accurate. In general, the present results are in good agreement with all the other simulations. The response involve sharp load drops which may be due to bifurcations.

Scordelis–Lo roof

In this example, a shallow cylindrical shell shown in Figure 6.4 is analyzed. It has been a primary benchmark problem for testing elasto–plastic shell finite–elements, and it demonstrates a high degree of geometric and material nonlinearities. Many researchers have analyzed this problem with the first complete results presented by Peric and Owen (1991).

URN:NBN:no-1282

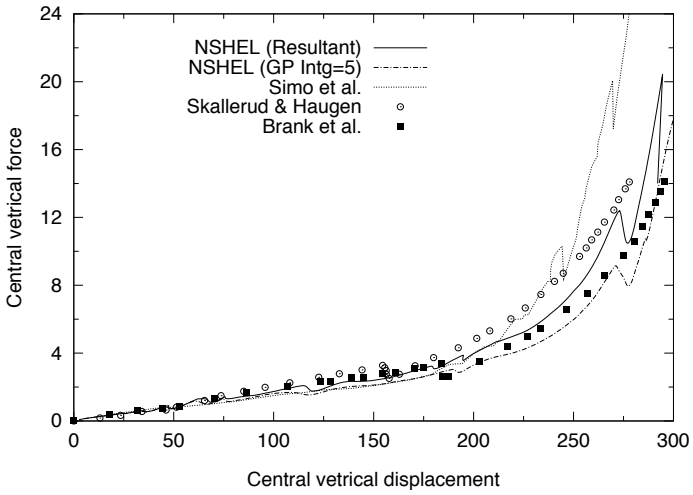

Figure 6.17 Elasto–plastic response of the pinched cylinder.

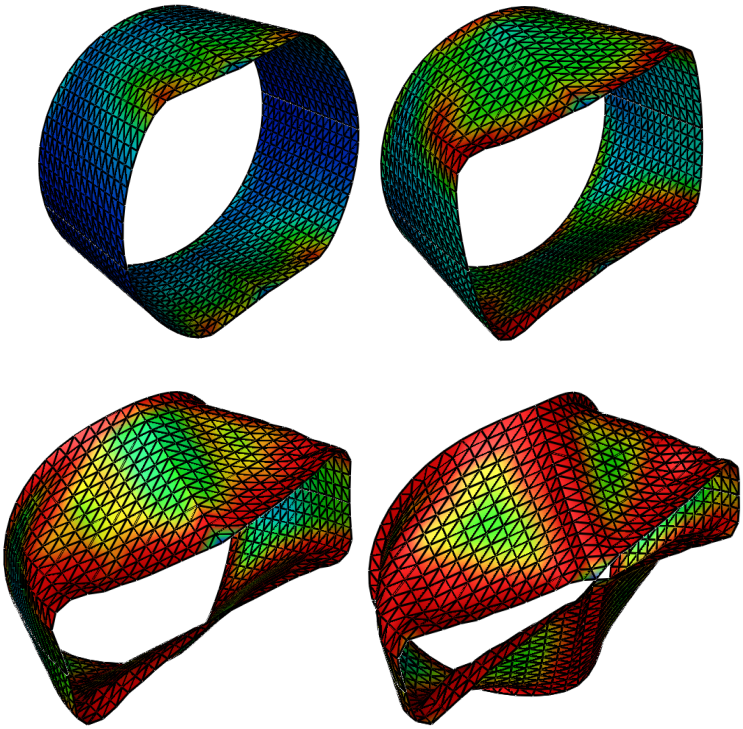

Figure 6.18 Pinched cylinder; Deformed shapes.

URN:NBN:no-1282

Skallerud and Haugen (1999) have presented results based on resultants plasticity, similar to the one in this thesis, using an ANDES finite element. While Peric and Owen (1991) used a large strain plasticity and a number of integration points through the thickness on a Morley element, Skallerud and Haugen (1999) used four integration points along the surface. The present analysis considers a single integration point per element.

The analysis is performed under increasing self–weight of 4KN/m^2 up to collapse. One quarter of the model is analyzed, restricting deformations to be symmetric along the lines $x = 0$ and $y = 0$. The straight edge AB is free while edge BC is pinned in the y and z directions and free axially. The geometry is described by $L = R = 7.6\text{m}$, $t = 0.076\text{m}$, and $\theta = 40°$. The material is assumed to be elastic–perfectly plastic with $E = 2.1 \times 10^4 \text{N/mm}^2$, $\nu = 0$, and $\sigma_\circ = 4.2\text{N/mm}^2$. Moderate rotation element is used.

The results are shown in Figure 6.19 along with those presented by Peric and Owen (1991) and Skallerud and Haugen (1999). The results from ABAQUS (1998) with a four–node element are also included. It is seen that the present results agree well with the others up to the ultimate load where, if we consider the fine mesh, they tend to follow those by Peric and Owen (1991) with an earlier load drop.

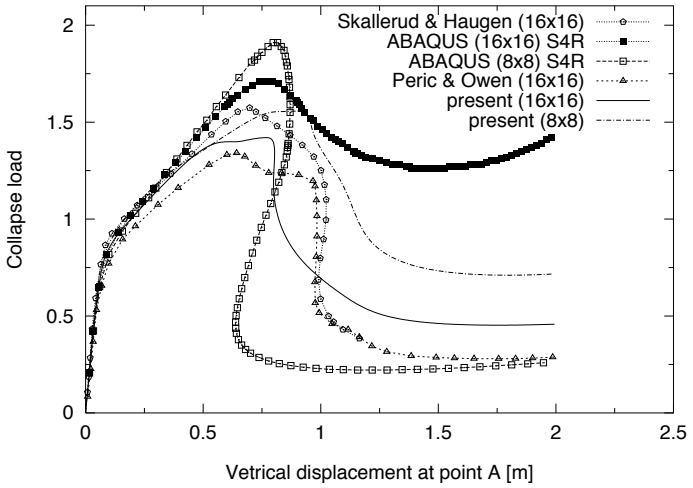

Figure 6.19 Scordelis–Lo roof; Vertical displacement at point A.

More comparisons are shown in Figure 6.20 including the results by Crisfield and Peng (1992), Roehl and Ramm (1996), and Brank *et al.* (1997). The variety of solutions in the post–collapse range is clearly observed. It demonstrates the problem's sensitivity to meshing, element type, number of integration points through thickness (denoted as 3PSI and 7PSI), etc. The difference in the results obtained with fine and coarse meshes with ABAQUS is particularly noticed.

For the present analysis, the results in Figure 6.20 are obtained by using a constant yield stress or surface reduction factor of 12%, (see Figure 5.4). This is is considered to be

URN:NBN:no-1282

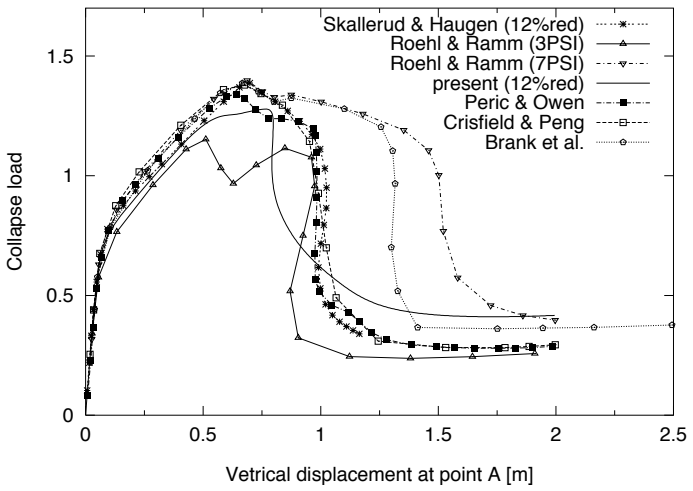

Figure 6.20 Scordelis–Lo roof; More comparisons.

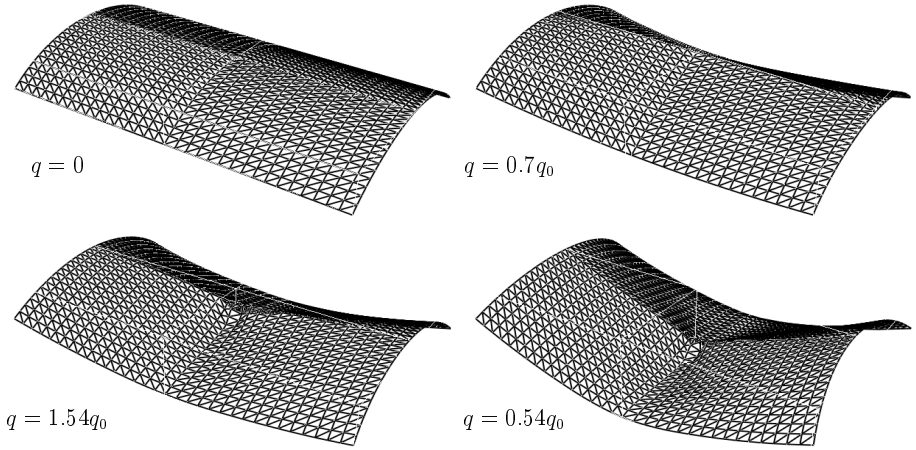

Figure 6.21 Scordelis–Lo roof; Deformed model.

reasonable because the problem is dominated by combined membrane and bending action. The same reduction was used by Skallerud and Haugen (1999). The deformed shapes at different load conditions are shown in Figure 6.21.

With reference to Figure 6.20, one may assume the results by Peric and Owen (1991) as a reference solution. Not only do they represent the averages in the post–collapse range, but also the following results by Crisfield and Peng (1992) and Skallerud and Haugen (1999) correspond well to them. It is interesting to notice that, apart from Skallerud and Haugen (1999), these results are based on the Morley shell elements. An important point,

URN:NBN:no-1282

however, is that the difficulties of using this example as a benchmark problem is clearly identified.

6.4 Efficiency of Plasticity Computations

In this section, the computational advantage of resultants plasticity with respect to the conventional through–the thickness integration is compared. This concern appears to have first been put forward by Mohammed *et al.* (2001) where it is mentioned that such an investigation will be presented in this thesis.

Four examples are selected for analysis. These include plate bending and buckling as well as shell collapse. For each case, pure elastic analysis is performed and followed by elasto–plastic analysis using resultants plasticity. Thereafter, several elasto–plastic analyses are performed using different number of integration points (NINT) over the thickness. The number of increments for each case is kept constant with the same convergence tolerance.

The computational efficiency is measured based on the Central Processing Unit (CPU) time of the machine. In order to obtain the computational time which is only demanded by the plasticity routines, CPU time of the elastic analysis is subtracted from the total elasto–plastic CPU time. The remaining computational time is normalized with respect the required time for resultants plasticity (NINT=1). The relative times are presented in Table 6.2. Cases 1 to 4 correspond to square plate bending, Scordelis–Lo roof, square plate buckling, and rectangular plate buckling, respectively.

Table 6.2 CPU time versus number of integration points.

NINT	1=Resultant	2	3	5	7	10	12
Case1	1.0000	1.2274	1.3981	1.5483	1.7539	2.2492	2.2243
Case2	1.0000	1.2835	1.3824	1.4941	1.6176	1.8529	2.0000
Case3	1.0000	1.0241	1.1270	1.2857	1.3333	1.5079	1.7460
Case4	1.0000	1.2197	1.3068	1.5227	1.8030	2.0265	2.2121
Average	1.0000	1.1887	1.3036	1.4627	1.6270	1.9092	2.0456

If we consider that most of the engineering problems would be solved efficiently using 3 to 5 number of integration points over the thickness, we can say that the time gain in a typical problem is in average about 30 to 50 percent. It should be noted that the resultant plasticity which is presented in Chapter 5 is very simplified in terms of computational requirements. For example, most of the very demanding matrix operations are performed analytically to obtain simple expressions.

It is, therefore, fair to say that most of the computational advantage depicted in Table 6.2 is a result of the present simplification. The conclusion may be that a typical double

URN:NBN:no-1282

surface resultants plasticity does not seem to have a significant computational advantage. This appears reasonable since the local matrices for thin shell resultants plasticity are 6×6, whereas 3×3 matrices appear in through–the thickness integration.

On the numerical stability, however, it seems that resultants plasticity can be more stable in some cases towards convergence. For example, it was observed that the main reason for CPU increase with respect to the number of integration points was generally due to the increase in the number of iterations per increment.

6.5 Efficiency of Element Formulations

It is worth to disclose that during the initial stage of this thesis, several element formulations in the family of Morley shell elements were investigated. At the end of the this study, two formulations were selected as presented in Chapters 3–4. According to the listing that follows this paragraph, these two formulations provide four alternative element types. The remaining elements are not described in this thesis, but their implementation in NSHEL (2000) offers the opportunity to measure their computational efficiency. The complete listing of the various element types is classified as,

1. Simplified TL element undergoing moderate rotations as described by Providas and Kattis (1999). This is similar to the element in Chapter 3 when $\boldsymbol{B}_k$ is equal to zero.

2. TL element undergoing moderate rotations as described in Chapter 3.

3. CR element undergoing large rotations as described by Peng and Crisfield (1992). The consistent CR formulation is applied directly to the assembly of linear constant strain triangle of Turner *et al.* (1956) and the linear constant bending element of Morley (1971).

4. CR element undergoing large rotations. This element is similar to number 3 above but it is derived in a different and more convenient way. It can be obtained from the textbook by Crisfield (1997) and also in the work of Zhong and Crisfield (1998). For this element, the implementation neglects the contribution of $\boldsymbol{K}_{rt}$ which is the geometric stiffness matrix resulting from coupled membrane–bending action. This omission was motivated by the study using element 3 from which it was found to have no significant contribution.

5. Facet TL–CR element undergoing large rotations. This is as described in Chapter 4 when the initial curvature is excluded.

6. Curved TL–CR element undergoing large rotations. It is as described in Chapter 4 when the initial curvature is included.

7. Element number 1 in this list which undergoes large rotations. It is described by Mohammed *et al.* (2000a) using CR–TL formulation.

URN:NBN:no-1282

Though, element types 3, 4 and 7 are not in fully working order, their numerical operations are not supposed to increase after they have been debugged. Therefore, they will be treated in a similar way to compare their computational efficiency as the other elements in the listing.

Table 6.3 shows the CPU time comparisons for four examples. Cases 1 to 4 correspond to square plate bending, Scordelis–Lo roof, rectangular plate buckling, and hinged roof, respectively. For each case, the number of increments is kept equal for all formulations. It is seen that the moderate rotation elements 1 and 2 are in average 2.8–3.6 faster than the other elements. In some few cases, the speed gain is almost 5 times more.

Table 6.3 CPU time versus element formulations.

Type	1&2	3	4	5&6	7
Case1	1.0000	2.4802	3.1186	2.9181	2.4774
Case2	1.0000	3.7699	4.8494	4.5021	3.7071
Case3	1.0000	2.4187	2.9864	2.8117	2.4038
Case4	1.0000	2.5342	3.1524	2.9545	2.5324
Average	1.0000	2.8007	3.5267	3.2966	2.7802

URN:NBN:no-1282

URN:NBN:no-1282

Chapter 7

Ultimate Strength and Collapse Analyses

7.1 Introduction

In Chapter 6, numerical examples have been presented to demonstrate the performance and efficiency of the developed formulations. The cases which have been studied are typically academic benchmark problems. The results have indicated that element formulations as well as the solution procedure perform very well. The purpose of the present chapter is to present examples of more practical significance.

The examples involve the study of some typical marine structural components and subsystems. In these examples, the ultimate strength and collapse analysis, due to extreme loads, are of great importance with respect to design. The analyses include stiffened plates subjected to axial compression, plate girder subjected to shear loading, and axial crushing of a cruciform. The latter is commonly known as X–element in the context of ship collision and grounding mechanics.

7.2 Stiffened Plate Panels

In ship structural design, one of the major considerations is the ultimate strength of the hull–girder. The key elements to this strength are the individual stiffened panels. These include plate panels, longitudinal stiffeners, and transverse frames as illustrated in Figure 1.1. The load–shortening curves of these panels can be utilized to predict the overall ultimate strength.

URN:NBN:no-1282

For panels in compression, the basic forces are axial compression from the overall hull girder bending moment, local bending from lateral pressure, transverse compression from the in–plane pressure loads, and shear. The problem in question is very complex with a large number of input parameters. Rigorously, the entire cross–section should be modelled.

In order to simplify the problem for design purposes, most of the Classification societies recommend a beam–column approach. In this approach, a single longitudinal stiffener with associated plate flange is considered being representative for the behaviour of the longitudinally stiffened panel.

7.2.1 Initial Imperfections

In a nonlinear finite element analysis of welded structures, it is generally necessary to introduce initial imperfections so as to obtain results of practical interest. The aim of these imperfections is to model the effects of true initial distortions and imperfect geometry, as well as residual stresses from fabrications. The real shape and magnitude of these imperfections are not exactly known. Normally, they are either selected so as to satisfy the tolerance requirements, or calibrated so that the buckling design curves are reproduced. Often, these two procedures yield approximately the same results.

The effect of initial imperfections is very significant for buckling strength of compressed members. The same is for the outcome of a numerical simulation on system collapse. If the structure is modelled as perfect or nearly perfect, the computed buckling resistance of various members will often be unrealistically high. An exception to this is when the load effects introduce significant deformational components which are compatible with the buckling mode. Numerically, the most common consequence of a perfect model is the singularity which is caused by bifurcation as illustrated in Figure 6.1.

Sources and types of imperfections

Structural imperfections can be grouped into two — *geometric deviations* and *residual stresses*. The geometric imperfections include deviations in axial out–of–straightness and cross–sectional parameters such as plate thickness, stiffener profile, and initial distortions. The out–of–straightness is particularly due to structural fabrication, but it is influenced by profile manufacturing as well. On the other hand, cross–sectional parameters are particularly due to profile manufacturing, but may also be influenced by structural fabrications. In addition to these sources, structural components do generally exhibit some degree of misalignments.

Residual stresses arise from manufacturing of the profile as well as fabrication of the structure (see e.g. Søreide (1981)). They are mainly caused by processes such as welding, flame cutting, and hot rolling of plates and profiles. All these processes create *heat affected zones* which cause expansion. The expansion is prevented by the adjacent cold regions in the expense of elastic stress mobilization in the cold regions. This leads to plastic

URN:NBN:no-1282

deformations in the heated zones with reduced yield stress. During cooling process, the heated zones contracts and are usually too short under normal temperature conditions. As a result, tension zones of residual stresses and permanent deformations are created.

While very little is known on imperfections due to fabrication of actual structures, significant information regarding geometric deviations and residual stresses for individual elements do exist. For stiffened plates, the residual stresses due to manufacturing balance in self–equilibrium in the sense that the net external force is zero. Normally, there is tension in the *heat affected zones* at the web toe and compression in the middle of the plate.

The beam–column approach, used in the design codes, considers the stiffener profile with the associated *effective* plate flange. In fact, the approach resembles the design of a regular beam–column where the concept of equivalent out–of–straightness is assumed to capture the combined effect of geometric deviations and residual stresses. For stiffened plates, however, three types of imperfections are considered. These types of imperfections can be considered in nonlinear finite element analysis as follows:

— *Plate imperfection.* This is taken in the form of plate out–of–plane displacement, and may be assumed to take a sinusoidal shape as,

$$w_p = w_p^\circ \sin\frac{n\pi x}{l} \sin\frac{\pi y}{s} \tag{7.1}$$

where w_p° is the allowable tolerance, n is the number of half sine–wave in the longitudinal direction, l is the plate length, and s is the plate width.

— *Interframe–stiffener imperfection.* This is given in the form of stiffener out–of–straightness relative to the plate plane. Herein, it is sometimes referred as stiffener beam imperfection. It is given by,

$$w_b = w_b^\circ \sin\frac{\pi x}{l} \tag{7.2}$$

where w_b° is the allowable tolerance.

— *Stiffener tripping imperfection.* This is the angular distortion of the stiffener that gives transverse displacements at the top of the stiffener. These displacements can be expressed as,

$$w_s = w_s^\circ \sin\frac{\pi x}{l} \tag{7.3}$$

where w_s° is again the allowable tolerance.

The tolerance requirements according to DNV (1992) Classification Note, are limited by the following expressions,

$$w_p^\circ = 0.01s \qquad w_b^\circ = 0.0015l \qquad w_s^\circ = 0.0015l \tag{7.4}$$

It should be noted that the best and proper way of considering initial imperfections is to use their measured values. However, these are not always available. Instead, eigenvalue

URN:NBN:no-1282

analysis has become a common practice in obtaining the buckling modes which are considered representative of the initial imperfections. The eigenvalue analysis is performed using a given loading condition, and the imperfections are applied with respect to the tolerance requirements as set for example by Equation (7.4). An alternative to eigenvalue analysis, is a meshing in which the initial coordinates follow Equations (7.1)–(7.3).

Using measured values of initial imperfections, Yao *et al.* (2001) have analyzed unstiffened rectangular thin plates under pure axial load. They concluded that hungry–horse imperfections cause the deflection of buckling mode to grow beyond the buckling load. However, the plastic deformations tend to localize and cause a rapid reduction of load carrying capacity in the post–collapse range. In a review by Soares and Søreide (1981), it is reported that the overall cylindrical deflection of the plate (which is caused by the welding process) may have a stiffening effect on rectangular plates. However, this increase in ultimate strength is of little practical interest since it is followed by a more violent nature of unloading.

Due to several uncertainties on the type and shape of the initial imperfections, and in the absence of measured values, the plate imperfection is best approximated by eigenvalue analysis in the form of buckling mode. Though this estimate does not represent the physical situation, it is based on the idea that it yields a lower bound or conservative critical load. For a stiffened plate subjected to lateral pressure, however, this procedure may not be straight forward since the type of buckling mode according to Figure 7.1 is not initially known. In this case, symmetric buckling is more likely, but with a low lateral pressure, asymmetric buckling may be possible.

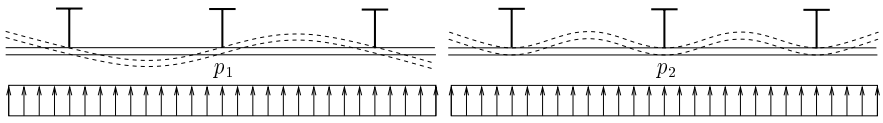

(a) Asymmetric buckling (b) Symmetric buckling

Figure 7.1 Buckling modes ($p_1 \ll p_2$).

When imperfections are introduced in the form of eigenmodes, several difficulties do arise. Generally, the individual eigenmodes are interrelated, and it may not be possible to obtain the three types of imperfections independently. This problem may be overcome by using, for example, a large plate thickness so as to trigger a pure stiffener beam buckling mode. However, as to plate buckling and stiffener tripping, the modes are definitely interrelated. Plate buckling induces rotations at the stiffener–plate intersection and hence torsional deformations of the stiffener, and vice versa. Again pure tripping of stiffener may, in principle, be obtained by using an artificially large plate thickness and add the two modes to obtain the correct maximum amplitude. If the stiffener is too flexible, tripping corresponding to correct plate imperfection may be too large. If subtraction and superposition can be used to obtain proper imperfection, it can be applied.

URN:NBN:no-1282

7.2.2 Reference Stiffened Plates

Nine T–stiffened plates of different geometries are analyzed. The panels are taken between two transverse frames. The scantlings, with reference to Figure 7.2, are given in Table 7.1 in which $\bar{\lambda}$ is the reduced slenderness ratio and β is the plate slenderness. These are defined as,

$$\bar{\lambda}^2 = \frac{\sigma_\circ}{\sigma_E} \qquad \beta = \frac{b_p}{t_p}\sqrt{\frac{\sigma_\circ}{E}} \tag{7.5}$$

where $\sigma_\circ$ is the yield stress, σ_E is the Euler buckling stress, and E is the Young's modulus. The transverse frame spacing is $l = 3000$mm, and the spacing between the longitudinal stiffeners is $s = b_p = 1000$mm. The steel material is assumed to be elastic–perfectly plastic with $E = 2.1 \times 10^5$ MPa, $\sigma_\circ = 300$ MPa, and $\nu = 0.3$.

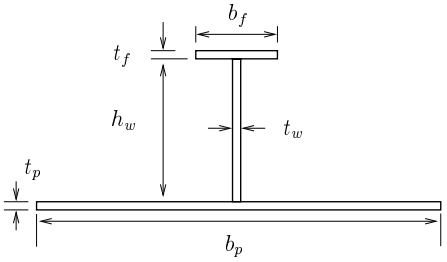

Figure 7.2 Cross–section of the stiffened plate.

Table 7.1 Geometrical parameters.

λ	β	t_p [mm]	h_w [mm]	t_w [mm]	b_f [mm]	t_f [mm]
	1.64	23.00	300	15.0	100	24.0
0.19	2.19	17.25	300	10.0	100	16.0
	2.74	13.80	300	10.0	100	11.2
	1.64	23.00	200	11.0	100	17.0
0.32	2.19	17.25	200	9.0	100	10.8
	2.74	13.80	200	6.0	100	7.8
	1.64	23.00	120	12.0	100	17.0
0.51	2.19	17.25	120	9.0	100	11.8
	2.74	13.80	120	6.0	100	8.7

7.2.3 Finite Element Modelling

The finite element mesh for the reference panel is shown in Figure 7.3. Depending on the height of the web, each model consists of 1920–2240 triangular shell elements. Assuming

URN:NBN:no-1282

symmetric buckling mode (Figure 7.1b), clamped boundary conditions are imposed at the panel ends. The axial boundary condition in one of the panel end is kept straight. Along the longer edges of the main plating, symmetric boundary conditions are imposed while transverse displacements are restrained for convenience. It is understood that transverse displacements are usually kept free with straight edge condition. However, numerical investigation has shown no difference between the two conditions for the the present panels. Slight difference could only be observed in very slender panels far from the present case.

Three types of initial imperfections are considered. They include plate imperfection, stiffener beam imperfection, and stiffener tripping. For plate imperfection, the buckling mode is selected as depicted in Figure 7.3 where the displacements are magnified 300 times for clarity. A single sinusoidal wave is taken as the stiffener beam imperfection. From Figure 7.3, it can be seen that the plate imperfection in the form of buckling mode introduces stiffener tripping inevitably. Based on DNV (1992) Classification notes, the tolerance values are set to $w_p^\circ = 10$mm and $w_b^\circ = 4.5$mm (see Equation (7.4)).

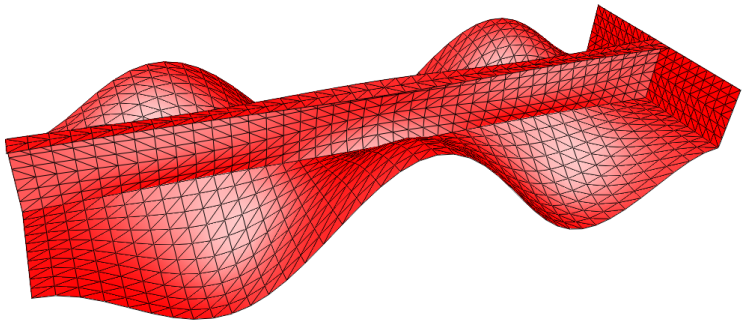

Figure 7.3 The reference panel; Mesh and initial imperfection.

7.2.4 Ultimate Strength Analysis

The analysis is limited to combined axial compression and lateral pressure. Anticipating plate induced failure, the lateral pressure is applied on the plate side in all the analyses. Both, axial compression and lateral pressure are incremented proportionally up to collapse. The basic idea behind simultaneous incrementation is that the ultimate capacity will be reached earlier than when the pressure is applied to a fixed unit factor. The results are compared with the beam–column predictions from the DNV (1992) Classification notes using a similar loading approach.

The load–shortening curves are shown in Figures 7.4–7.6 along with the results based on ABAQUS (1998) analysis. It is observed that there is a good agreement between the two simulations. A typical panel after failure is shown in Figure 7.7. Though the results from both finite element formulations show a good agreement, a deviation of up to 30% is

URN:NBN:no-1282

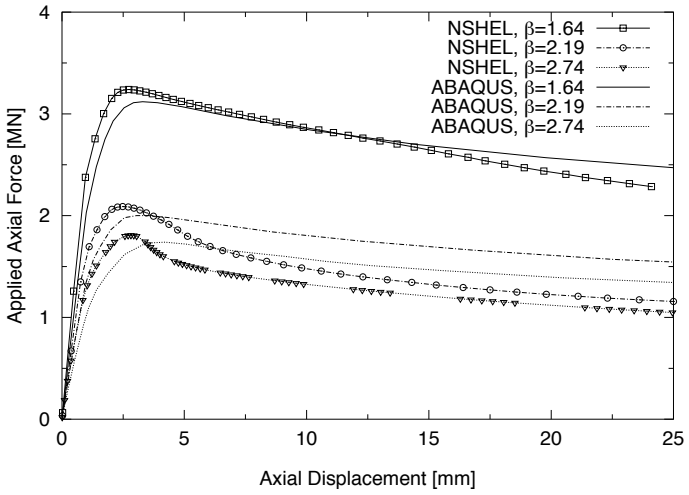

Figure 7.4 Load–shortening curves for $\bar{\lambda} = 0.19$

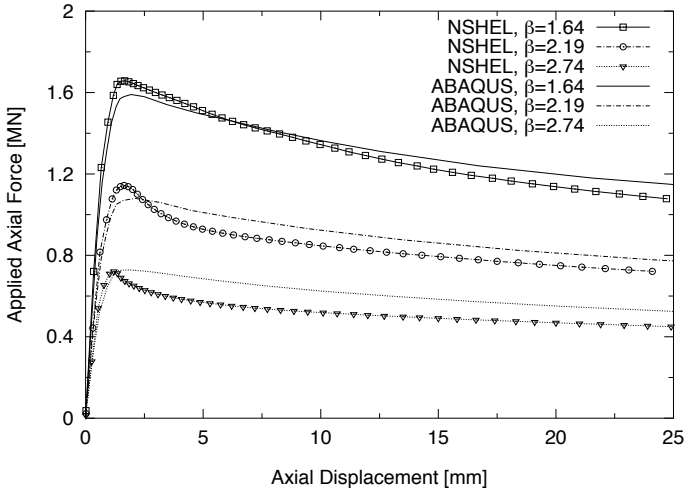

Figure 7.5 Load–shortening curves for $\bar{\lambda} = 0.32$

observed for stiffer panels with $\bar{\lambda} = 0.19$ when comparison with DNV (1992) is made. This is depicted in Figure 7.8 in terms of critical stress versus plate slenderness. In addition, the ultimate strength values for the present formulations are a little higher than those from ABAQUS results. This can be due to the difference in plasticity formulations.

Regarding critical failure mode, however, the DNV design code is found to be in

URN:NBN:no-1282

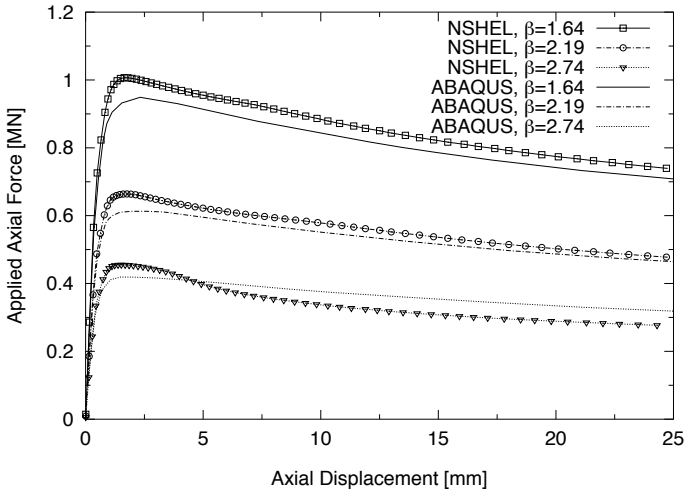

Figure 7.6 Load–shortening curves for $\bar{\lambda} = 0.54$

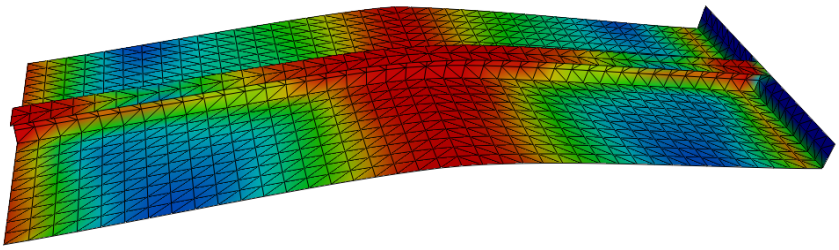

Figure 7.7 Example of deformed model.

agreement with the finite element simulations. For instance, in panels with $\bar{\lambda} = 0.19$, the finite element simulation shows that they are failing with plate induced compressive failure. On the other hand, for $\bar{\lambda} = 0.32$ and $\bar{\lambda} = 0.51$, tensile yielding of the stiffener is the governing mode. Similar predictions are made by the DNV design code.

The effect of lateral pressure

To evaluate the DNV (1992) design code for the observed deviation in ultimate capacity with respect to stiffer panels, a panel with $\bar{\lambda} = 0.19$ and $\beta = 2.19$ is selected for further investigation. Due to proportional load increments, it is anticipated that stiffer panels carry larger pressure loads as well. Therefore, it is interesting to vary the magnitude of reference pressure load for investigation. In doing so, the load–shortening curves are obtained as

URN:NBN:no-1282

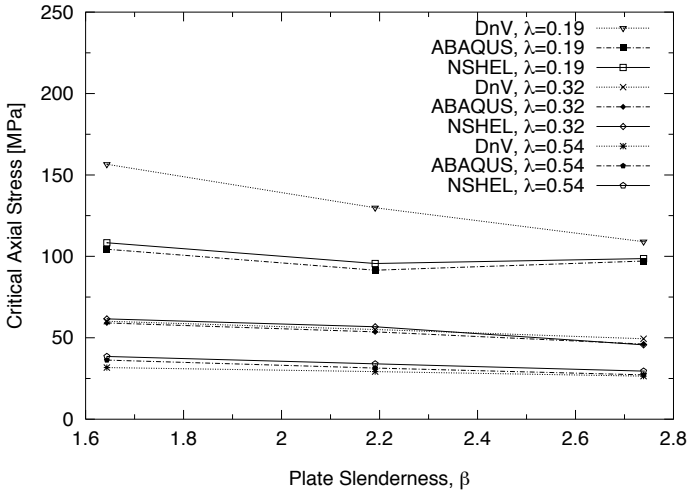

Figure 7.8 Critical stress w.r.t. slenderness.

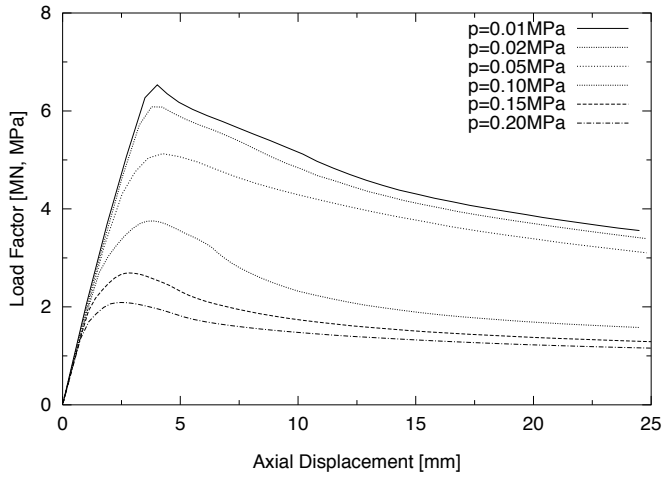

Figure 7.9 Load–shortening curves; Reference axial force = 1MN.

shown in Figure 7.9. As expected, the ultimate capacity increases with decreasing reference lateral pressure.

The plots of critical axial stress versus critical pressure in Figure 7.10 indicates that; while the DNV code is very conservative for lower pressure loads, it becomes non–conservative with higher lateral pressure loading. Similar observation is also made by Wang and Moan (1997) where a combined bi–axial and lateral pressure loads were applied

URN:NBN:no-1282

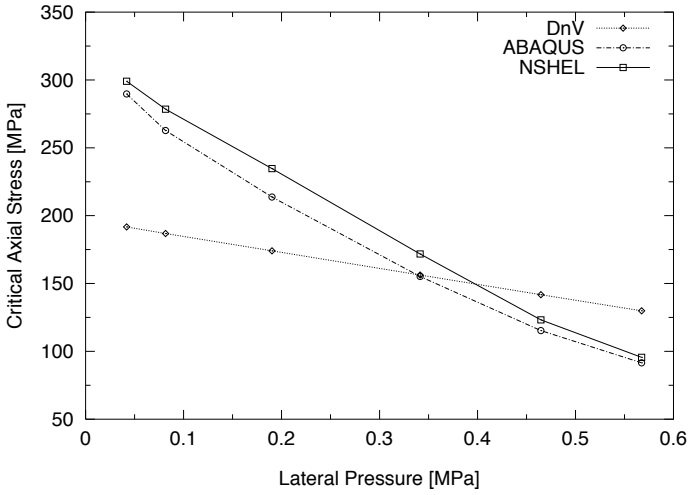

Figure 7.10 The influence of lateral pressure.

to stiffened plates with L–type stiffeners. In the latter, the lateral pressure was applied only to a fixed level, while the axial compression was incremented until collapse.

7.3 Shear Collapse of Aluminum Plate Girder

Generally, design criteria for plate girders without longitudinal stiffeners involve checking of bending and shear stresses as well as the local and overall instabilities. For plates in shear, an important component of post collapse strength may result from the diagonal tension that develops. This effect is commonly known as the tension field action, and it depends on the relative flexibility between the girder web and flanges.

For girders with thin webs and strong flanges, very high capacity in shear is obtained with the web plate resisting much of the applied load in tension. This effect has been studied for many decades. The basic theoretical background and references can be found in ECCS (1986). In the work of Höglund (1997), the design method and review of experimental results reported in the literature (on aluminum alloy and steel plate girders) are presented. For shear buckling resistance according to Eurocode-9 (1998), this method is the basis.

The analyses in this section are based on the work of Langhelle and Eberg (1999) who carried out a series of tests on aluminum plate girder under different temperatures. Here, only the test results at room temperature are focused. The scantlings of the tested girder, which is an end panel, are shown in Figure 7.11. In end panels, the dominating force is the shear including horizontal forces from the inner panels. In thin webs, this

URN:NBN:no-1282

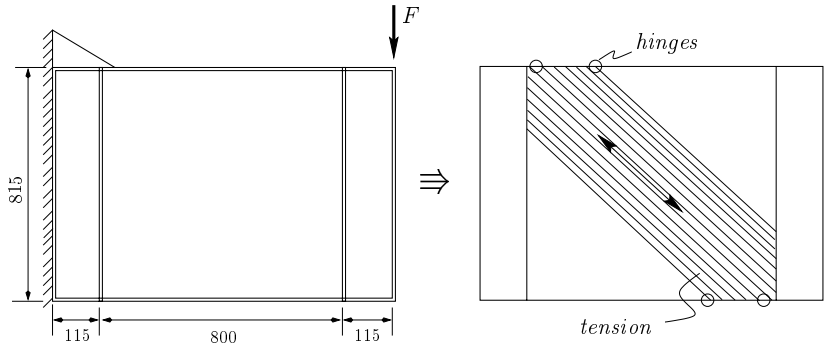

Figure 7.11 Aluminum panel; Scantlings.

shear capacity depends on whether the end post is stiff or weak in the longitudinal girder direction. According to Eurocode-9 (1998), the relative dimensions of this girder satisfy the condition of having a rigid end post.

7.3.1 Finite Element Analysis

The finite element modelling considers a clamped boundary condition on one end. At the remaining end, out–of–plane web displacements are restricted. A concentrated shear force equal to 1000KN is applied at the free end. A similar modelling is applied in ABAQUS (1998) analyses.

The load–displacement curves from the analyses and tests are shown in Figure 7.12. In general, the finite element and test results correspond well. The slight deviations observed can be attributed to the uncertainties of nominal material properties. The results of the two finite element formulations are very close to each other. It should be noted that ABAQUS uses five integration points through thickness and plane, while in the present analysis we have considered a single integration point per element.

From Figure 7.12, it is seen that the strength prediction according to Eurocode-9 (1998) design code is very conservative. Figure 7.13 shows the deformed shape of the girder after collapse. It can be observed that the finite element analysis has captured very well the displacement pattern according to the test results.

7.4 Crushing Strength of a Cruciform

In the field of crashworthiness of ship structures during grounding and collision, the crushing response of ship panels is of primary importance. Usually, the response involves large

URN:NBN:no-1282

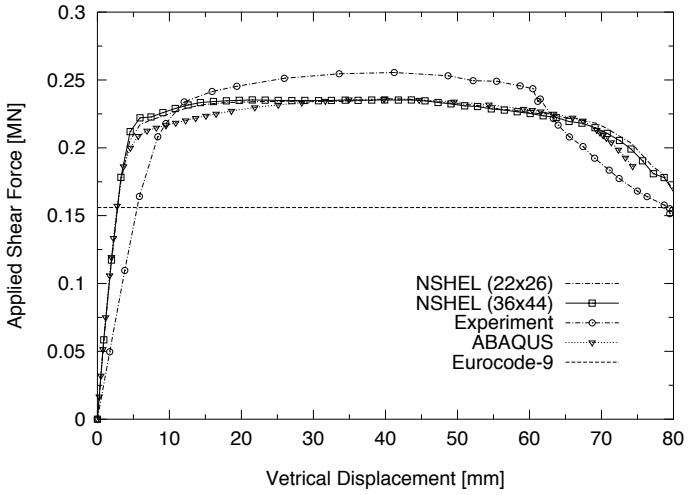

Figure 7.12 Load–displacement curves for aluminum plate girder.

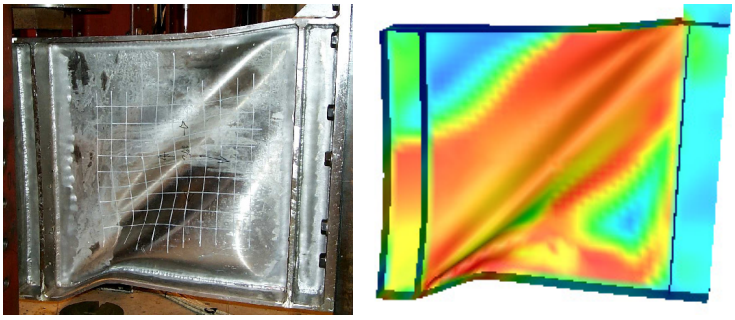

(a) Experiment (b) NSHEL Simulation

Figure 7.13 Deformed aluminum plate girder.

deformations of shells and local instabilities followed by localization of plastic deformations. Detailed analysis may often be prohibitive in terms of computer time and storage, and therefore simplified methods based on plastic analysis become an alternative.

Simplified models are given e.g. by Amdahl (1983). The procedure is based on dividing the structure into basic elements such as X, Y, and T–elements instead of plane plate or shell elements. The idea is that the material in the immediate vicinity of a plate intersection absorbs most of the energy. The energy dissipation is calculated for each basic element, and the total energy dissipation is obtained by summing up the contributions from all basic elements.

URN:NBN:no-1282

7.4.1 Analytical Method

The analytical prediction of energy absorption in a structure during crushing is based on a simplified energy method. In this approach the external work must balance the internal energy stored or dissipated in the structure. The analytical models such as Amdahl (1983) and Kierkegaard (1993) assume complete ductility with no material fracture.

Based on experimental work on X and T–elements made from steel material, it is suggested that the structure is crushed with an intersection line between the flanges remaining straight. This failure mode is commonly referred to as the straight edge mechanism and it is illustrated in Figure 7.14. The basic folding mechanism has been presented by Amdahl (1983).

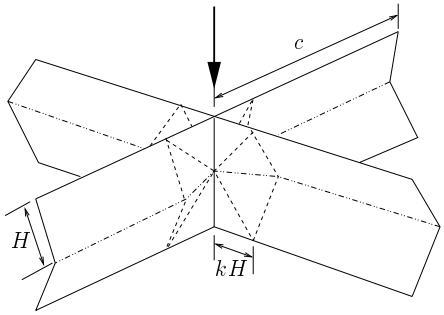

Figure 7.14 Cruciform; Straight edge mechanism.

The X–element is considered more representative in the sense that the average crushing force for the remaining basic elements can be deducted from it. Its average crushing force can be calculated as,

$$F_{av} = \left(22.8\sqrt{\frac{c}{t}} + 5.7\right)\frac{\sigma_f t^2}{4\eta} \tag{7.6}$$

where c is the flange length, and t is the thickness. The factor η ranges between 0.6–0.8 and was introduced by Abramowicz (1983). It represents the effective crushing distance because the structure can not be crushed to a zero length in practice. The characteristic flow stress σ_f is typically taken as the average between the yield and ultimate stress of the material curve.

7.4.2 Experimental and Finite Element Methods

For the basic elements mentioned in the foregoing, a number of representative test results exist including those by Urban *et al.* (1999) and Simonsen (2000). These results can be used as a benchmark in testing the performance of finite element formulations. For that purpose, an X–element resembling the one presented by Simonsen (2000) has been selected

URN:NBN:no-1282

for the analysis. The basic idea is to compare the failure mode predicted for a typical basic element.

The reference element has a height of 800mm, a flange width of 270mm, and a 15mm thickness. This yields c/t ratio equal to 18. The material is considered to be elastic–perfectly–plastic with $E = 2.1 \times 10^5$ MPa, $\sigma_\circ = 300$ MPa, and $\nu = 0.3$. A small initial imperfection with a maximum amplitude of 1mm, based on the eigenproblem analysis, is introduced to trigger the buckling pattern.

Since the present finite element implementation does not include material fracture and contact algorithms, the basic element is compressed up to 100mm only. Thereafter, the deformations can not be simulated without fracture and contact models. Within the range of the analysis, however, the deformations show a very good agreement with the experimental observation as shown in Figure 7.15. The deformed shape based on LS-DYNA3D simulations (as obtained by Simonsen (2000)) is also shown.

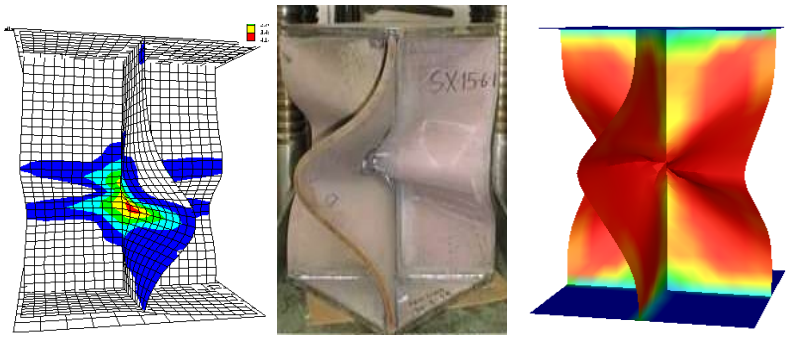

(a) DYNA Simulation (b) Experiment (c) NSHEL Simulation

Figure 7.15 Axial crushing of X–element.

In comparison with analytical models, the straight edge mechanism is clearly observed. The results of the finite element simulation are presented in Figure 7.16. The analytical value of the average crushing force as calculated by Equation (7.6) using $\eta = 0.8$ is also plotted in the figure.

URN:NBN:no-1282

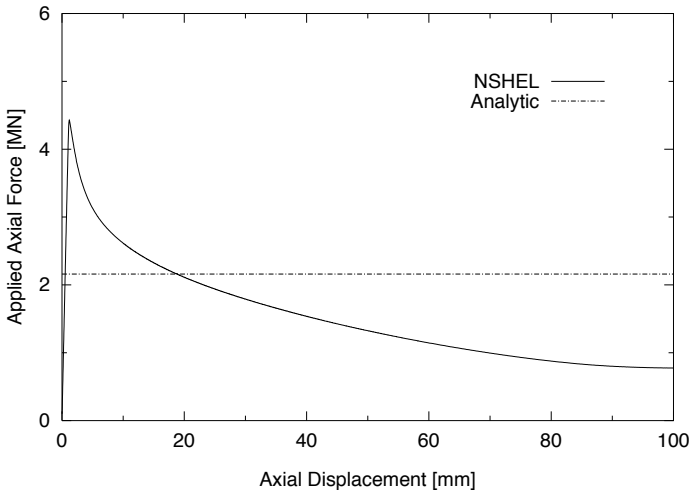

Figure 7.16 Load–shortening curve for X–element.

URN:NBN:no-1282

URN:NBN:no-1282

Chapter 8

Multi–span Stiffened Panels

8.1 Introduction

The longitudinal ship–hull strength is generally assessed by calculating the strength of individual stiffened panels illustrated in Figure 1.1. It has been mentioned in Chapter 1 that most of the Classification rules use a beam–column approach for design of stiffened plate panels. The procedure considers one (single span) isolated stiffener, with associated width of the main plating, as representative of the whole panel behaviour. In finite element analysis, a single span stiffened panel can be considered in two ways. These are shown in Figure 8.1 as model types A and B. The beam–column model is similar to model type B. Although both models are frequently used in finite element analysis, model type A is the most common.

The single span approach has been in practice for many years and it is the basis of most of the previous studies. In terms of boundary conditions used, however, it appears that there is much to be verified against larger models and practical boundary conditions. By larger models, we mean multi–span panels in the directions of longitudinal stiffeners and transverse frames. With the current progress in computer technology, this type of analysis can be carried out with similar or less computational time than what a single span panel took a couple of years ago.

While computer simulations of single span stiffened panels can easily be performed, such models are very difficult to test in the laboratory. In fact, even if this model is tested in the laboratory, the uncertainties of the test setup in terms of boundary conditions may undermine the accuracy of the results. This complexity, and the problem of appropriate boundary conditions, can be relaxed by using a model involving multi–span stiffened panels. It provides not only a better and practical model for finite element analysis but also a better model for laboratory test. With this possibility, the results can be easily verified against experimental values.

URN:NBN:no-1282

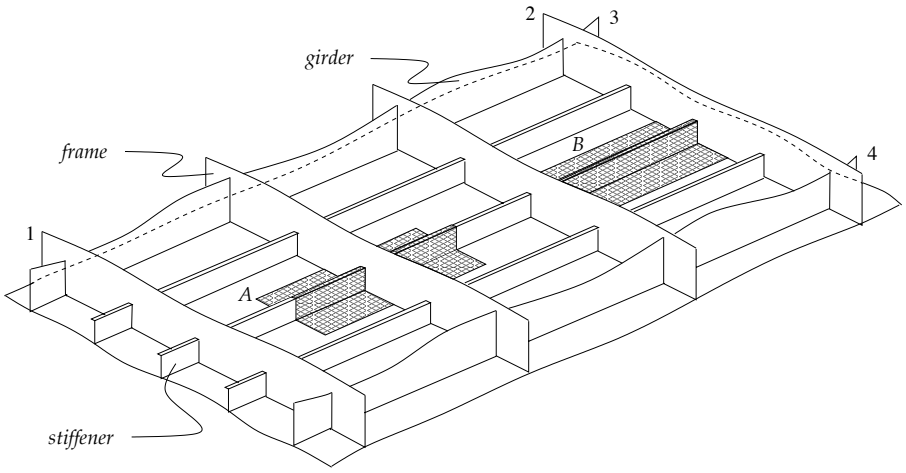

Figure 8.1 Oblique view of a stiffened panel; Model types.

With reference to Figure 8.1, model type A considers four neighboring quarters of the plates around the frame–stiffener intersection. It is denoted as the *two half span–two half bay* model. The resulting portion of the panel has magnitude equal to that of a single span stiffened plate. In model type B, two half plates along the stiffener are considered and it can be called *one span–two half bay* model. Both models have the same dimensions but different boundary conditions.

When the panel is subjected to in–plane forces only, the boundary conditions for models A and B can easily be specified. In the presence of lateral pressure, however, model A is better than model B. This is mainly because both, symmetric and asymmetric, buckling modes (Figure 7.1) can be analyzed using model A with the same boundary conditions at the mid–span. In other words, one does not need to have a pre–knowledge on the type of buckling mode. On the other hand, when model B is used, it is necessary to run two analysis with clamped and simple support boundary conditions, respectively.

At the mid–span of model A, symmetric boundary conditions are applied with the stiffener web allowed to move transversely. Concerning the boundary conditions of the plate short edges, two possibilities exist. These are clamped and simple support conditions, in which the actual condition depends on the plate aspect ratio. Rigorously, plates with an even number aspect ratio should be free with respect to rotation, while plates with an odd number aspect ratio are clamped. For intermediate values of aspect ratios, it is not straight forward to determine the appropriate boundary conditions. The same applies when the partial rigidity against rotation at the transverse frames is to be considered. This case may be handled by performing two analysis with clamped and simple support condition, and select the conservative estimates.

What appears to be significant is that neither model A nor B include the transverse

URN:NBN:no-1282

frame physically. Normally, the effect of transverse frames is modelled by restraining lateral displacements of the plates at frame–plate intersection. In addition, the stiffener web is fixed in the transverse direction. The plate continuity is represented by straight boundary condition along all edges. Though these boundary conditions appear to be quite natural for the models which are used, there are physical effects that need to be considered and investigated. For instance, analysis of a larger system may indicate failure of single stiffened plate. In that case, the symmetric boundary conditions might not be able to predict the true behaviour. In addition, considering that the frames are strong enough, there can be a mechanism of load redistribution especially when transverse axial forces are involved.

Regarding the stiffness of the transverse frames in relation to restriction of lateral displacements, it may be easier to compress the plate alone than a combination of plate and frame altogether. This can be of much significance when straight edge boundary conditions are used. In addition, the degree of plate stiffness at this plane may have much contribution from the built–in frames. This effect may well be missed with the conventional boundary conditions. All in all, the proper and practical boundary conditions along the plate–frame intersection may not be correctly simulated without involving the transverse frames in the model.

Though symmetric boundary conditions are common in structural analysis, they are indeed a kind of idealization to which the behaviour is forced to follow. The nature of this condition for *compressed* stiffened panels may have impact on the results. For example, imperfections or even small perturbations may influence the displacements at the loaded edge leading to a different failure mode.

Regarding the size of the model, it is reported in a review by ISSC (2000) that the study of finite element modelling principles for stiffened plate panels has been performed by Yao *et al.* (1998). In this investigation, it was concluded that a triple half–span model is somewhat better than the two half–span (model type A) for studying the collapse behaviour under combined compression and lateral pressure. The main feature of this approach is that the symmetry conditions on the shorter edge are moved by one span further.

The aim of the analysis in this chapter is to employ a large model involving multi–span panels. In doing so, the physical boundary conditions will be introduced somehow away from the stiffened plate considered, and the symmetric boundary conditions will be avoided. It is believed that this will minimize the influence of the imposed boundary conditions in areas where they are usually introduced. With this model, the influence of the transverse frames will also be investigated. The results will be compared with those based on the conventional model of single span stiffened plate.

Contrary to the analyses in the previous chapters, the analysis in this chapter will make use of the four–node element in the commercial computer program ABAQUS (1998). It should, however, be pointed out that results could be efficiently obtained by using the three–node element in NSHEL (2000). The reason for using ABAQUS is that the straight edge boundary condition, which is much needed in this study, was not fully implemented in NSHEL (2000) by the time of this analysis. However, similar numerical examples from NSHEL by using the available boundary conditions will be presented to demonstrate the performance of the foregoing formulations.

URN:NBN:no-1282

8.2 The Reference Panels

Two reference panels of different aspect ratio and slenderness are considered. They both represent the bottom plating, between two longitudinal girders, of a ship double–hull as illustrated by Figure 8.2. The first panel is a part of a real oil carrier and it is denoted as STP1. The scantlings of this panel make a very stiff panel. The second panel, that is referred to as STP2, is an artificial panel. Its scantlings are selected such that a slender panel with different aspect ratio is obtained.

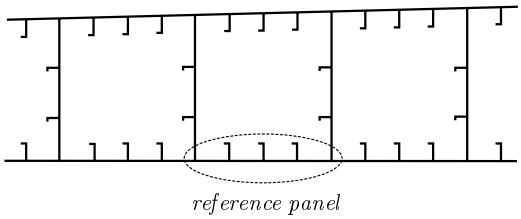

Figure 8.2 Part of ship double bottom; Construction detail.

A sketch of the bottom plate for both panels is as shown in Figure 8.1. In panel STP1, the distance between the transverse frames is 3200mm while the longitudinal stiffener spacing is 800mm. The corresponding dimensions for panel STP2 are 3000mm and 1000mm. The thickness of the main plating is 18mm for both panels. The stiffeners are L–shaped with their dimensions given in Table 8.1. The material is assumed to be elastic–perfectly plastic with $E = 2.1 \times 10^5$MPa, $\nu = 0.3$, and $\sigma_\circ = 250$MPa.

Table 8.1 Panel properties.

Panel	l	s	t_p	h_w	t_w	b_f	t_f	β	$\bar{\lambda}_{0.6}$	$\bar{\lambda}_{1.0}$
STP1	3200	800	18	370	13	53.5	34	1.5335	0.1487	0.2478
STP2	3000	1000	18	200	13	53.5	24	1.9168	0.2809	0.4680

The considered multi–span stiffened panel is enclosed within three spans between transverse frames number 1 and 2, and four spans between longitudinal girders number 3 and 4 (see Figure 8.1). For each panel, two types of models are studied. The first model includes all transverse frames and longitudinal stiffeners, and it is denoted as model type C. In the second model, which is referred to as model type D, the interior transverse frames are removed. The aim of this model is to evaluate the influence of transverse frames. The transverse frames are represented by large T–shaped stiffener–like components. The height is set equal to twice the web height of the stiffeners, and the web thickness is 20mm.

URN:NBN:no-1282

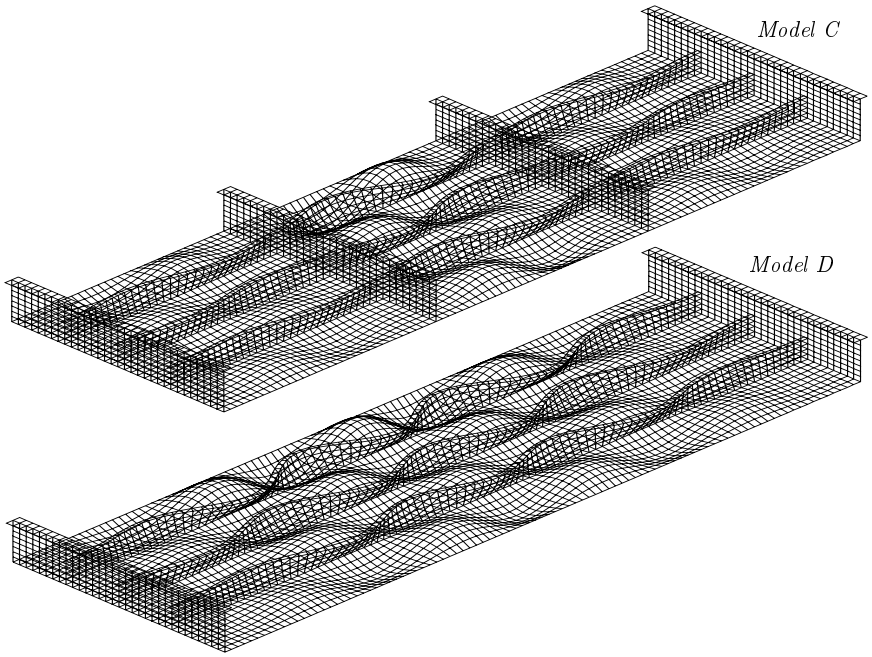

Figure 8.3 Model types and Initial imperfections; Panel STP1.

8.3 Finite Element Modelling

The finite element mesh for both panels involves 5792 rectangular elements for model type C. The corresponding number of elements is 5152 for model type D. In the single span panel analysis, relative mesh size is used. For NSHEL (2000) analysis, the number of elements is doubled as triangular elements are used. The finite element models are shown in Figures 8.3–8.4 in the form of first buckling modes.

Along all four edges of the panels, simply supported and straight edge boundary conditions are imposed. At the frame–stiffener intersection, the stiffener flanges are free to rotate, and are not connected to the frame web. Assuming that the bending stiffness of the transverse frames is large enough, lateral displacements are fixed at frame–plate intersection. In model type D, the stiffeners are transversely supported at the frames. For bi–axially loaded panels closer to the ship sides, the effect of the longitudinal boundary condition is studied. A comparison is made between the straight edge and transversely free edge.

As discussed in Chapter 7, it is necessary to introduce initial imperfections in the buckling analysis. These artificial imperfections accounts for the effects of true initial distortions, residual stresses due to fabrications, imperfect geometry, etc. In the present analyses, however, the initial imperfections do not *fully* follow these requirements.

URN:NBN:no-1282

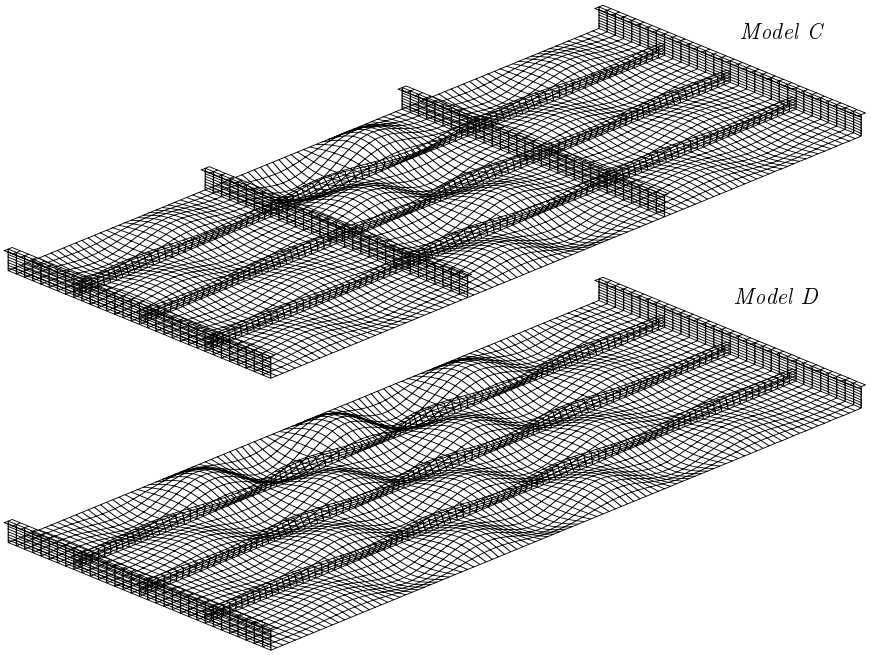

Figure 8.4 Model types and initial imperfections; Panel STP2.

To trigger initial buckling, buckling modes based on eigenvalue analysis are considered. These are introduced such that the plate out–of–straightness follows the DNV (1992) tolerance requirements. As it can be seen in Figures 8.3–8.4, these eigenmodes introduce a degree of stiffener–tripping imperfection as well. This imperfection is also considered and it is calibrated such that it does not exceed the tolerance requirements. For simplicity, the so–called beam imperfection is not considered. What is important to point out is that all the results which are compared are based on the same procedure.

8.4 Ultimate Strength Analysis

The analysis considers four loading conditions. These include uni–axial and bi–axial compression, both with and without lateral pressure. The reference axial compression normalized by the uni–axial critical buckling stress (σ_x/σ_{crx}) is 1.0 for both panels STP1 and STP2. The corresponding values for the transverse compression (σ_y/σ_{cry}) are 0.20 and 0.37, respectively. These values are based on 3MN axial compression and 0.9MN transverse compression. Both, compression and lateral pressure are simultaneously and proportionally incremented up to collapse of the panel. The values of applied lateral pressure at collapse are given in Table 8.2.

URN:NBN:no-1282

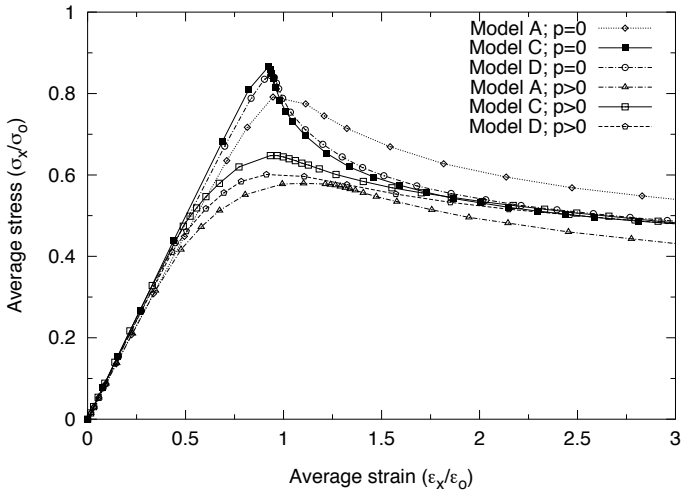

Figure 8.5 Panel STP1; response under uni–axial compression.

8.4.1 Uni–axial Compression

The response curves for this case are shown in Figures 8.5–8.6. They represent the cases of pure axial compression as well as the combined compression and lateral pressure. The normalized ultimate strength values are given in Table 8.3. It is observed that the single span model A provides conservative estimates of ultimate strength values. Model type C shows an increase in ultimate strength by approximately 6 to 12 percent.

Removing the transverse frames from the finite element model, as indicated by model type D, gives results somewhere between those of model types A and C. The increase as compared to the single span model is approximately between 3 to 7 percent. These values indicate not only the significance of the transverse frame rigidity but also the consequence of smaller model with symmetric boundary condition.

For panel STP2, which is somehow slender than STP1, the response curves for multi–span models show a moderate unloading in the post collapse range. The single span model, however, predicts a rather steep unload. This effect is important when the energy absorption capacity is to be considered.

Table 8.2 Lateral pressure at collapse [MPa].

Panel→	STP1			STP2		
Model→	A	C	D	A	C	D
Uni-axial	0.3740	0.4180	0.3880	0.2260	0.2400	0.2350
Bi-axial	0.3690	0.4170	0.3860	0.2270	0.2390	0.2320

URN:NBN:no-1282

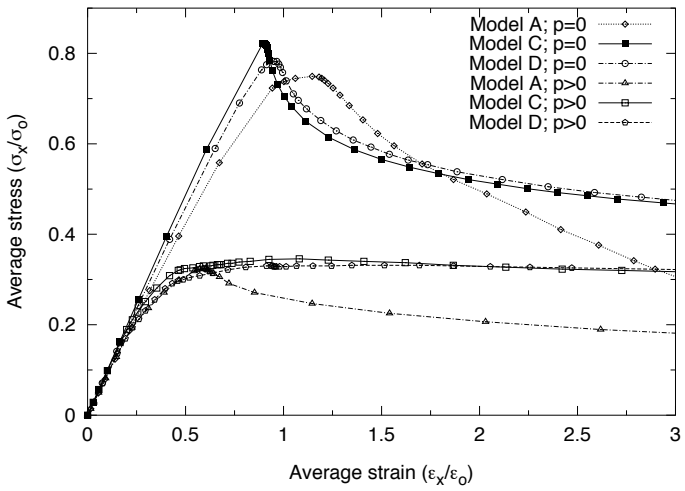

Figure 8.6 Panel STP2; response under uni–axial compression.

Table 8.3 Ultimate strength comparisons.

	Panel→	STP1			STP2		
Pressure↓	Model→	A	C	D	A	C	D
$p = 0$	Uni-axial	1.0000	1.0939	1.0665	1.0000	1.0958	1.0287
	Bi-axial	1.0000	1.0875	1.0525	1.0000	1.1164	1.0434
$p > 0$	Uni-axial	1.0000	1.1176	1.0374	1.0000	1.0619	1.0398
	Bi-axial	1.0000	1.1301	1.0461	1.0000	1.0529	1.0220

8.4.2 Bi–axial Compression

Figures 8.7–8.8 show the response curves for bi–axial compression analysis. Again, the cases of pure compression and combined compression and lateral pressure are considered. The normalized ultimate strength values are given in Table 8.3. The curves provide similar observations as for uni–axial compression case in Section 8.4.1. The trend of steep unloading for the single span model is also observed here. The increase in ultimate strength is approximately 5 to 13 percent for model C and about 2 to 5 percent for model D.

The observed failure modes are generally similar for both uni–axial and bi–axial analyses. Due to the size of the image files, only selected examples of deformed shapes are presented. These are given in Figures 8.9–8.10 for pure bi–axial compression, and combined bi–axial compression and lateral pressure. Under pure bi-axial compression, it is seen that both panels show a localized failure mode around the middle of the panel. In addition, panel STP2 shows little lateral displacements due to interframe buckling. The stiffener tripping is very much pronounced for panel STP1.

URN:NBN:no-1282

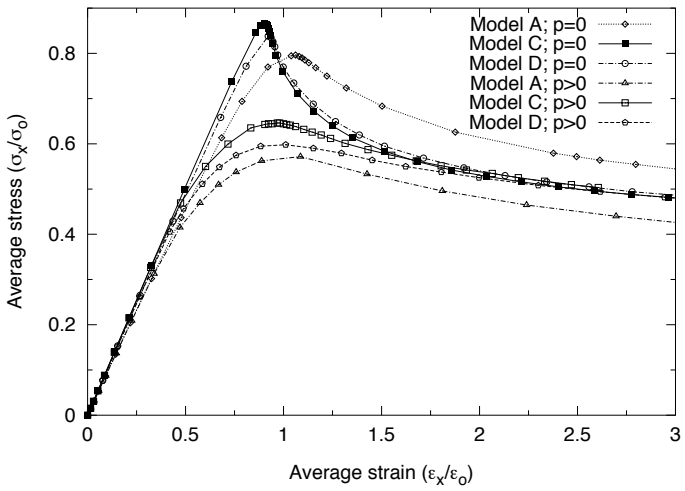

Figure 8.7 Panel STP1; response under bi–axial compression.

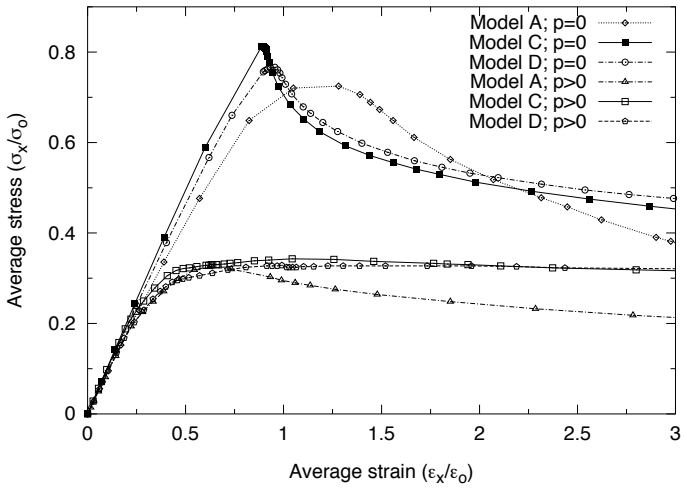

Figure 8.8 Panel STP2; response under bi–axial compression.

Under combined bi–axial compression and lateral pressure, the failure mode for panel STP2 is governed by interframe buckling in the middle span. With the exception of panel STP1 model C, the plastic utilization under this loading is generally spread over the whole panel. For panel STP1, the failure in model C is almost localized in the middle span with low plastic utilization in the outer spans. On the other hand, there is considerable localization around the position of interior frames for panel STP1 model D as opposed to model C.

URN:NBN:no-1282

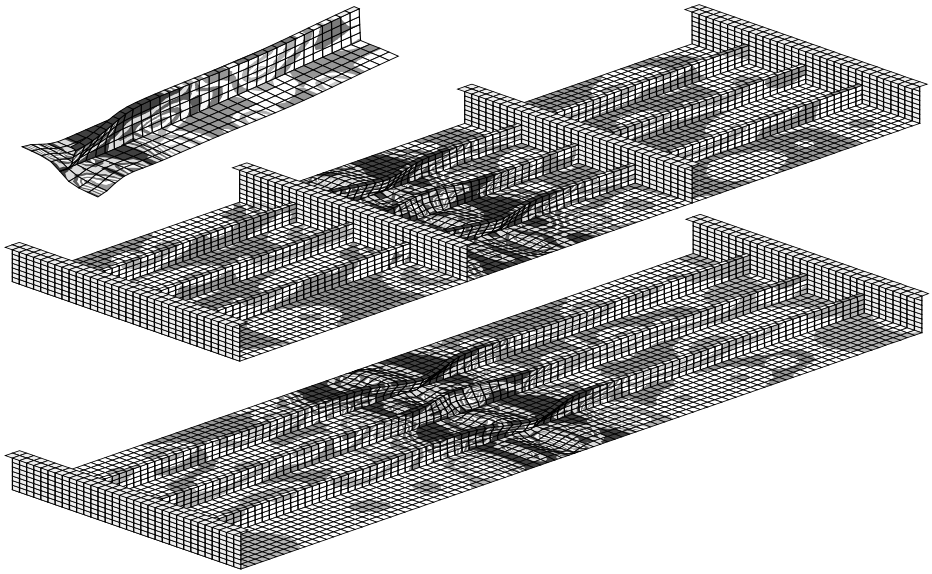

(a) Pure bi–axial compression

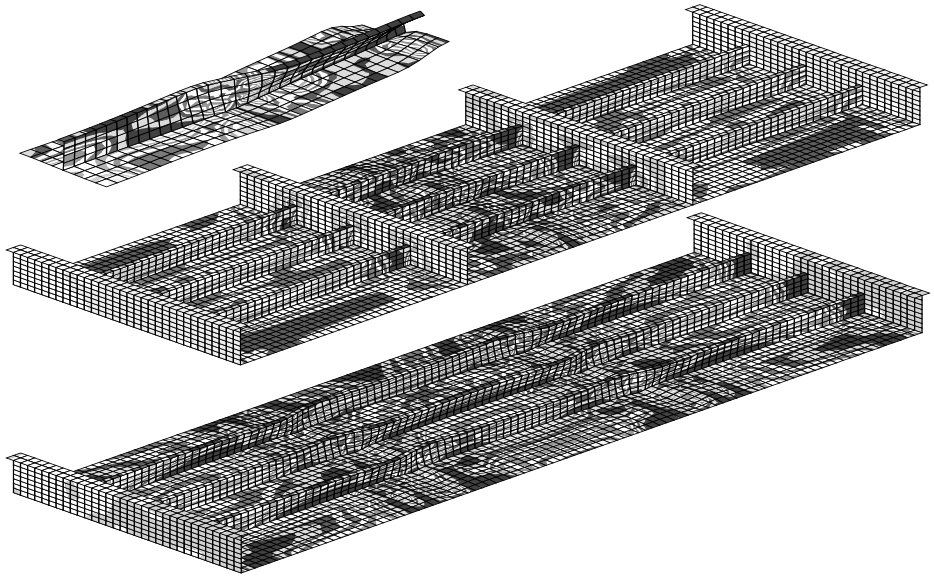

(b) Bi–axial compression and pressure

Figure 8.9 Panel STP1; Model deformations.

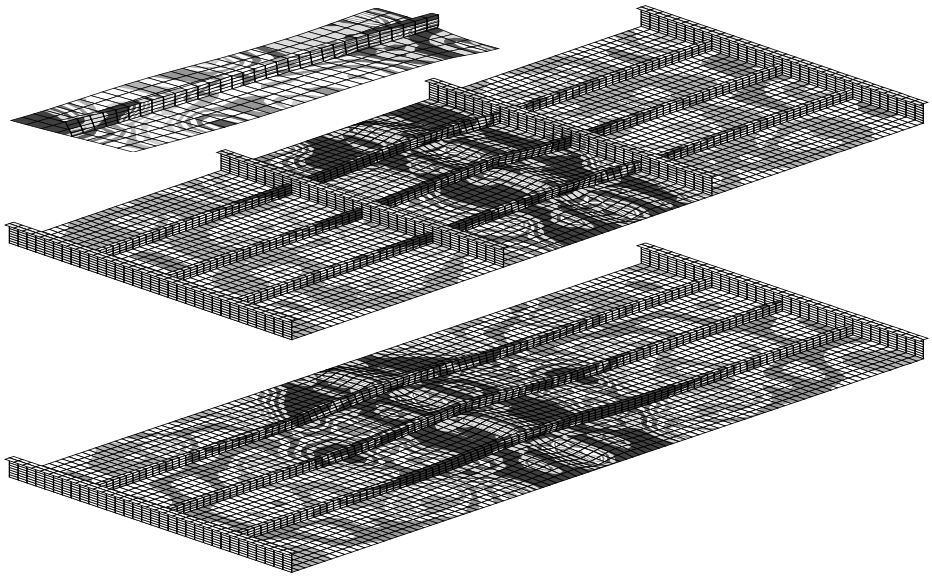

(a) Pure bi–axial compression

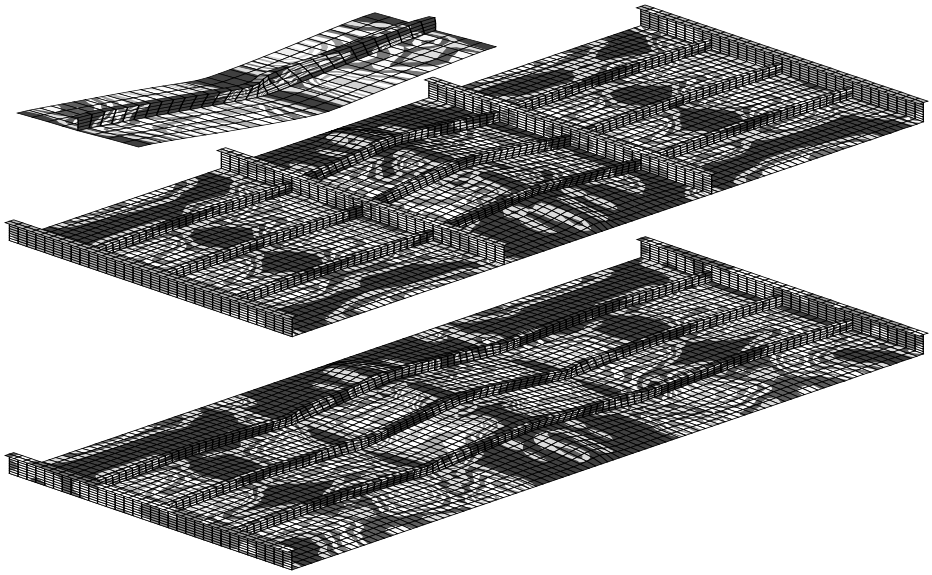

(b) Bi–axial compression and pressure

Figure 8.10 Panel STP2; Model deformations.

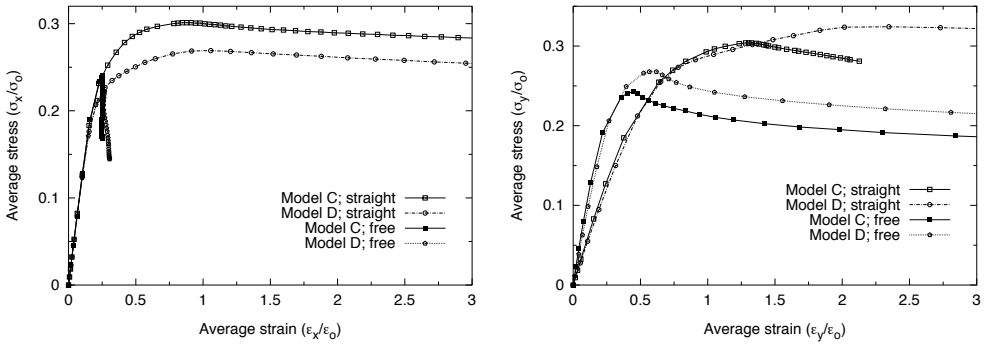

Figure 8.11 Panel STP1; Effect of longitudinal edge boundary condition.

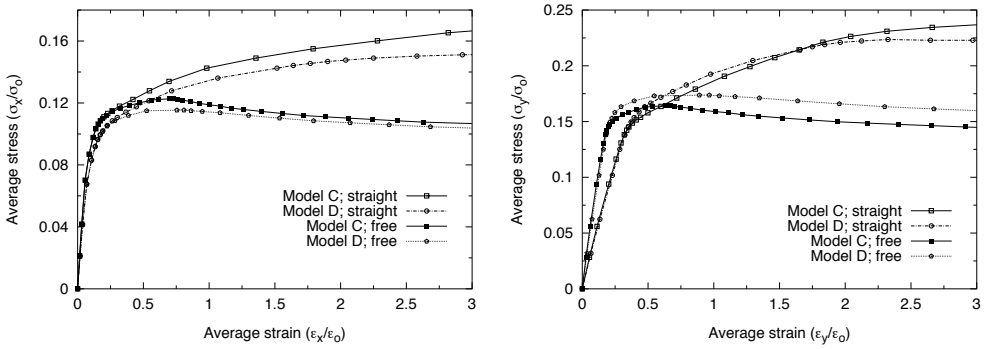

Figure 8.12 Panel STP2; Effect of longitudinal edge boundary condition.

The effect of straight edge condition

For plate panels closer to ship sides, it is likely that the straight edge boundary condition is non–conservative. The plate continuity which is the main reason for straight edge condition does not exist for ship sides. Under very high transverse compression, deformations which do not represent straight edge may happen. To study this concept, analyses with two different boundary conditions are performed.

While the first analysis considers the conventional straight edge condition, the second analysis allows the edge to move freely in the transverse direction. Model types C and D are studied. The reference transverse compression normalized by the uni–axial critical buckling stress (σ_y/σ_{cry}) is 1.0 for both panels STP1 and STP2. The corresponding values for the axial compression (σ_x/σ_{crx}) are 0.46 and 0.25, respectively. These values are based on 3MN transverse compression and 0.9MN axial compression.

The response curves for both panels are shown in Figures 8.11–8.12. It can be seen

URN:NBN:no-1282

that there is a very significant effect of straight edge boundary condition for both panels. The trend is the same whether or not transverse frames are included in the model. In the post collapse range, the effect is even more severe for panel STP1 which is stiffer than STP2. It has been observed from the analysis that the main cause of this effect is a localization of the transverse displacements.

If we consider *straight edge* as the most strict boundary condition and the *free edge* as the less strict condition, we can say that the true ultimate strength and the post collapse response lies somewhere between the two curves. Therefore, it is more conservative to apply the free condition in this case.

8.4.3 Uni–axial Compression Analysis by NSHEL

To demonstrate the performance of the formulations presented in Chapters 3–6, panel STP1 has been analyzed using NSHEL (2000). Since the straight edge condition is not fully implemented in this program, the transversely restrained condition is used instead. Because NSHEL offers triangular elements only, the number of elements is double of that used in the previous sections. The finite element mesh and the magnified initial imperfection are shown in Figure 8.13.

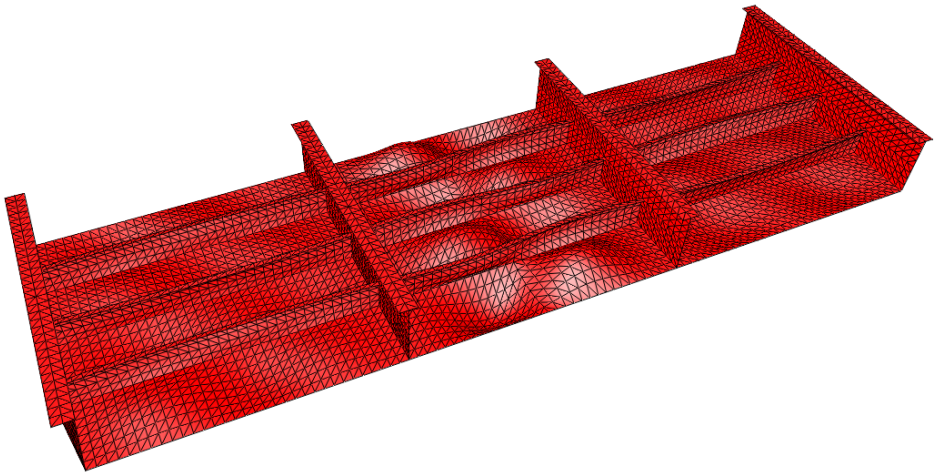

Figure 8.13 NSHEL mesh and initial imperfection.

The loading and analysis conditions are similar to the ones used in Section 8.4.1. In other words, the combined uni–axial compression and pressure are applied proportionally up to collapse. The same reference axial compression is applied, but the lateral pressure is applied as 0.4, 0.7 and 1.0 of the reference value in three different analyses. The response curves are given in Figure 8.14. The results are based on through–the thickness integration algorithm (Section 5.4) with five Gaussian points in integration. It can be seen that the

URN:NBN:no-1282

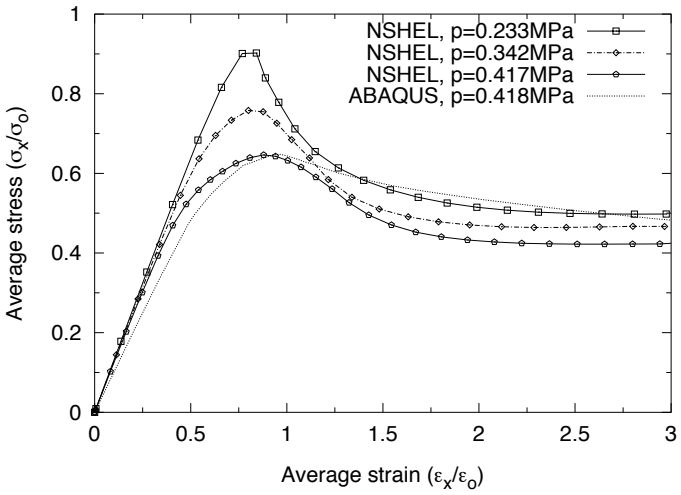

Figure 8.14 Response of panel STP1 based on NSHEL analysis.

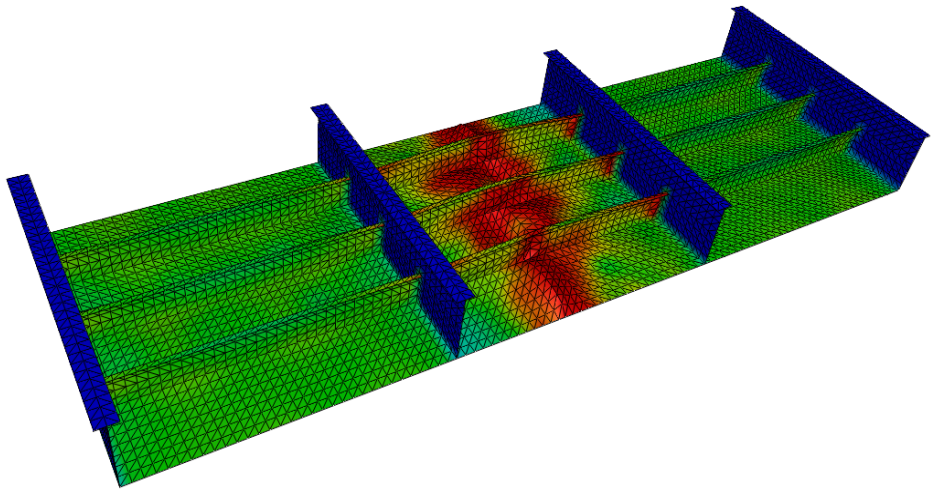

Figure 8.15 Deformed shape from NSHEL.

ultimate strength predictions for the two finite element formulations are very close to each other.

The corresponding deformed shape from NSHEL (2000) analysis is shown in Figure 8.15. Just like Figure 8.9a, a localized failure mode is also observed in this analysis.

URN:NBN:no-1282

Chapter 9

Concluding Remarks

9.1 Conclusions

Several shell finite elements in the family of constant stress elements have been investigated. Out of these, two elements have been selected for presentation. The first element is valid for moderate rotations and have been shown to be very efficient. It has been shown to be computationally faster than the rest of the elements. Considering that there exist many practical applications which undergo plastic deformations with the rotations remaining essentially moderate, the present thesis has extended this element to include material nonlinearity. The elasto–plastic formulation has been shown to perform very well within the element range of validity.

For problems which undergo large rotations, an earlier proposed shell has been re–visited and new equilibrium equations have been derived. The main advantage with these equations is that they provide variable tangent stiffness within an increment as opposed to constant tangent stiffness in the earlier formulation. This provides faster convergence of the global Newton–Raphson iterations. The element is displacement–based and includes the initial curvature of the shell surface. It is, therefore, considered as curved element. The resulting equations appear to be very similar to those of an earlier proposed element in a mixed–formulation.

Material plasticity formulation involving Huber–von Mises type of yield surface has been presented. Both, through–the thickness integration and resultants plasticity have been considered. The resultants plasticity discussed is a modified one in which the Ilyushin yield surface has been rendered a hyperellipse to avoid corner discontinuities. The modification introduces a non–conservatism ranging from zero to twelve percent, depending on the degree of combination between membrane and bending forces. Means of controlling this error have been suggested. The modified surface has an advantage that instead of multi–surface plasticity, there is only one yield surface for stress update.

URN:NBN:no-1282

In the plasticity equations, the most involving matrix operations have been performed analytically. As a result, expressions which are simple and more efficient for computations have been derived for both resultants plasticity and through–the thickness integration. The yield surfaces are expressed by simple scalar equations of the plasticity multiplier. The plasticity computations involve a solution of a single scalar equation.

The nonlinear finite elements and plasticity formulations have been implemented in a stand–alone computer program. Numerical examples have been presented and compared with the results from other publications. It has been shown that the proposed formulations provide very good results.

With the present simplified resultants plasticity, the low cost advantage of resultants plasticity over the integration through–the thickness has been found to be about 30 to 50 percent. This observation has assumed that a typical integration would need about 3 to 5 integration points. It can, therefore, be said that a complete *double surface resultant plasticity* may not provide significant computational advantage due to its complex matrix operations. For the case of computational efficiency, however, resultants plasticity appear to be more stable in reaching convergence. In that case, the present *modified yield surface* in stress resultants provides both computational efficiency and advantage.

Numerical examples which are more practical and significant in ultimate strength and collapse analysis of ship structures have been presented. Results which compare very well with experimental observations have been obtained. For stiffened plate panels, it has been found that the beam–column approach used by DNV design code provides non–conservative estimates of ultimate strength in some loading conditions.

The significance of multi–span modelling of stiffened panels over the conventional single span model has been studied. The goal was to simulate results based on more realistic boundary conditions. In addition, the influence of transverse frame rigidity to the interframe panel collapse has also been evaluated. It has been found that the single span model produces conservative estimates of ultimate strength. The rigidity of transverse frames is found to be very significant since it reduces the effective buckling length. The straight edge boundary condition in the longitudinal edges has been studied. This effect has been found to give an upper bound solution. The lower bound is associated with transversely free boundary condition.

9.2 Recommendations

For triangular elements which undergo arbitrary large displacements and rotations, it has appeared in Section 6.5 that element type 7 is among those providing fastest computation. It is unfortunate that the time frame did not allow a complete derivation. It is, therefore, recommended to develop this element towards successful implementation. Concurrently, it would be more convenient if this development will consider using a common presentation of the modular matrix with the coefficient c equal to $1/2$. If symmetry of tangent stiffness matrix would appear to be a problem, artificial symmetrization can be applied.

URN:NBN:no-1282

If a four node element based on the concepts presented in this thesis is developed, it may provide more efficiency. Towards that direction, one may suggest an element with about 16 degrees of freedom with possible condensation technique. The element would still assume constant stresses with the initial curvature included. Although this element might not be very efficient for double curved surfaces, it is likely to provide more efficiency and better model for stiffened panels and cylindrical shells.

In Chapter 7, it has appeared that the DNV design code (beam–column) give non–conservative estimates for plate induced failure of stiffer panels. Normally these types of panels are typical for ship deck and bottom plates. It is, therefore, recommended to perform a thorough investigation on this area and the possible improvements for the design code be suggested.

On multi–span panels, the effect of transverse frames appears to be significant. Therefore, more nonlinear finite element analyses with some experimental work for validation is required. Emphasis need to be put on the frame modelling and the significance of various types of initial buckling modes as far as the conservative estimates are concerned.

URN:NBN:no-1282

URN:NBN:no-1282

References

ABAQUS (1998). *General purpose finite element analysis program* (Version 5.8 ed.). USA: Hibbitt, Karlsson & Sorensen, Inc. User's Manual; Theoretical Manual.

Abramowicz, W. (1983). The effective crushing distance in axially compressed thin–walled metal columns. *Int. J. Impact Eng. 1* (3), 309–317.

ABS (1995). *Guide for dynamic based design and evaluation of bulk carrier structures*. American Bureau of Shipping.

Amdahl, J. (1983). *Energy Absorption in Ship–Platform Impacts*. Ph. D. thesis, NTH, University of Trondhem, Norway.

Argyris, J. H. (1960). *Energy Theorems and Structural Analysis*. London: Butterworths Scientific Publications. (Originally published in a series of articles in Aircraft engineering; From 1954 to 1955).

Argyris, J. H., H. Balmer, J. S. Doltsinis, P. C. Dunne, M. Haase, M. Klieber, G. A. Malejannakis, J. P. Mlejenek, M.Muller, and D. W. Scharpt (1979). Finite element method—the natural approach. *Comput. Methods Appl. Mech. Engrg. 17/18*, 1–106.

Bäcklund, J. (1973). *Finite element analysis of nonlinear structures*. Ph. D. thesis, Chalmers University, Göteburg, Sweden.

Başar, Y. and M. Itskov (1999). Constitutive model and finite element formulation for large strain elasto–plastic analysis of shells. *Computational Mechanics 23*, 466–481.

Batoz, J. L. (1982). An explicit formulation for an efficient triangular plate–bending element. *Int. J. Numer. Meth. Engng. 18*, 1077–1089.

Batoz, J. L., K. J. Bathe, and L. W. Ho (1980). A study of three–node triangular plate bending elements. *Int. J. Numer. Meth. Engng. 15*, 1771–1812.

Bell, K. (1997). *SAM Library*. Trondheim, Norway: NTNU–SINTEF.

Belytschko, T. and J. Hseih (1973). Nonlinear transient analysis with convected coordinates. *Int. J. Numer. Meth. Engng. 7*, 255–271.

Belytschko, T. and L. Schwer (1977). Large displacement, transient analysis of space frames. *Int. J. Numer. Meth. Engng. 11*, 65–84.

URN:NBN:no-1282

Bergan, P. G., M. K. Nygård, and R. O. Bjærum (1990). Free formulation elements with drilling freedoms for stability analysis of shells. In W. B. Krätzig and E. Oñate (Eds.), *Computational Mechanics of Nonlinear Response of Shells*, Berlin, pp. 164–182. Springer–Verlag.

Besseling, J. F. (1980). Another look at the application of the principle of virtual work with particular reference to finite plate and shell elements. In W. Wunderlich, E. Stein, and K. J. Bathe (Eds.), *Europe–US Workshop*, Ruhr–University Bochum, Germany, pp. 11–27. Springer, Berlin, 1981.

Besseling, J. F. and E. van der Giessen (1994). *Mathematical modelling of inelastic deformation*. London: Chapman & Hall.

Bout, A. (1993). A displacement–based geometrically nonlinear constant stress element. *Int. J. Numer. Meth. Engng. 36*, 1161–1188.

Brank, B., D. Peric, and F. B. Damjanic (1997). On large deformations of thin elasto–plastic shells: Implementation of a finite rotation model for quadrilateral shell element. *Int. J. Numer. Meth. Engng. 40*, 689–726.

Bucciarelli, L. L. and N. Dworsky (1980). *Sophie Germain: An essay in the history of the theory of elasticity*. Dordrecht, New York: D. Reidel Pub.

Burgoyne, C. J. and M. G. Brennan (1993a). Calculation of elasto–plastic rigidities using the exact Ilyushin yield surface. *Int. J. Solids Structures 30*(8), 1133–1145.

Burgoyne, C. J. and M. G. Brennan (1993b). Exact Ilyushin yield surface. *Int. J. Solids Structures 30*(8), 1113–1131.

Chen, K. K. (1979). A triangular plate finite element for large displacement elastic–plastic analysis of automobile structural components. *Comp. Struct. 10*, 203–215.

Clough, R. W. (1960). The finite element in plane stress analysis. In *Proc. 2nd ASCE Conf. on Electronic Computation*. PA: Pittsburgh.

Cook, R. D., D. S. Malkus, and M. E. Plesha (1989). *Concepts and applications of finite element analysis – 3rd Edition*. New York: John Wiley & Sons.

Crisfield, M. A. (1979). Ivanov's yield criterion for thin plates and shells using finite elements. Technical Report Report LR 919, Transport and Road Research Lab., Crowthorne, Berks., England.

Crisfield, M. A. (1982). Solution procedures for nonlinear structural problems. In E. Hinton, D. R. J. Owen, and C. Taylor (Eds.), *Recent advances in nonlinear computational mechanics*. Swansea: Pineridge Press.

Crisfield, M. A. (1991). *Nonlinear Finite element Analysis of Solids and Structures; Volume 1. – Essentials*. New York: John Wiley & Sons.

Crisfield, M. A. (1997). *Nonlinear Finite element Analysis of Solids and Structures; Volume 2. – Advanced Topics*. New York: John Wiley & Sons.

Crisfield, M. A. and X. Peng (1992). Efficient nonlinear shell formulation with large-rotations and plasticity. In *COMPLAS–3*, Barcelona, pp. 1979–1997.

URN:NBN:no-1282

Dawe, D. J. (1972). Shell analysis using a simple facet element. *J. Strain Anal. 7*, 266–270.

DNV (1992). Buckling strength analysis. In *DNV Classification Note No. 30.1*. Høvik, Norway: Det Norske Veritas.

DNV (1995). *Hull structures based on extended calculation procedure*. Det Norske Veritas Classification AS.

Drucker, D. C. (1951). A more fundamental approach to plastic stress strain relations. In *Proc. 1st. U.S. Natl. Congress Appli. Mech.*, pp. 487–91.

ECCS (1986). Behaviour and design of steel plated structures. In P. Dubas and E. Gehri (Eds.), *Applied Statics and Steel Structures*. Zürich, CH–8093 Zürich, Switzerland: Swiss Federal Institute of Technology. Publication No. 44.

Eidsheim, O. M. (1980). *Nonlinear analysis of elastic–plastic shells using hybrid stress finite elements*. Ph. D. thesis, Division of Structural Engineering, NTH, Trondheim, Norway. Report No. 80–1.

Ernst, L. J. (1981). *A geometrically nonlinear finite element shell theory*. Ph. D. thesis, TU Delft, Netherlands.

Eurocode-9 (1998, February). Design of aluminum structures [Part 1.1: General rules]. European Committee for Standardisation, Rue de Stassart 36, B–1050 Brussels. ENV 1999–1–1, CEN/TC 250/SC 9.

Felippa, C. A. (1996). *Lecture Notes in Nonlinear Finite Element Methods*. University of Colorado, Boulder: Center for Aerospace Structures. CU–CAS–96–16.

Flügge, W. (1960). *Stresses in shells*. Berlin: Springer–Verlag. Second Printing, 1962.

Fried, I. (1984). Orthogonal trajectory accession on the nonlinear equilibrium curve. *Comput. Methods Appl. Mech. Engrg. 47*, 283–297.

GLView (1999). *3D visualization and animation software* (6.0 ed.). 7462 Trondheim, Norway: CEETRON ASA.

Golub, G. H. and C. F. V. Loan (1989). *Matrix computations – 2nd Edition*. Baltimore: Johns Hopkins University Press.

Green, A. E. and P. M. Naghdi (1965). A general theory of an elastic–plastic continuum. *Arch. Rat. Mech. Anal. 18*, 251–281.

Haugen, B. (1994). *Buckling and stability problems for thin shell structures using high performance finite elements*. Ph. D. thesis, University of Colorado, USA.

Hellan, K. (1967). Analysis of elastic plates in flexure by a simplified finite element method. In *Acta polytechnica Scandinavica. Civil Engineering and Building Construction Series*, 46. Trondheim, Norway: Norges Tekniske Vitenskapsakademi.

Herrmann, L. R. (1967). Finite element bending analysis of plates. *J. Eng. Mech. Div. ASCE 93*(EM5), 13–25.

Herrmann, L. R. and D. M. Campbell (1968). A finite element analysis of thin shells. *AIAA Journal 6*, 1842–1846.

URN:NBN:no-1282

Höglund, T. (1997). Shear buckling resistance of steel and aluminum plate girders. *Thin–Walled Structures 29*(1–4), 13–30.

Horrigmoe, G. and P. G. Bergan (1978). Nonlinear analysis of free–form shells by flat finite elements. *Comp. Meth. Appl. Mech. Engg. 16*, 11–35.

Huber, M. T. (1904). *Czasopismo tech.* Lwów, Poland. (cited by G. A. Maugin, 1992, page 18): Vol. 15, 1904.

Ibrahimbegović, A. and F. Frey (1992). Stress resultants elasto–plastic analysis of plates and shallow shells. In *COMPLAS–3*, Barcelona, pp. 2047–2059.

Ilyushin, A. A. (1956). *Plasticite*. Paris: Editions Eyrolles.

Irons, B. M. and A. Razzaque (1972). Experience with the patch test for convergence of finite elements. In A. K. Aziz (Ed.), *Proc. Symp. on the Mathematical Foundations of the Finite Element Method with Applications to Partial Differential Equations*, New York, pp. 557–587. Baltimore, Academic Press.

ISSC (2000). Technical Committee III.1 — Ultimate Strength. In *14th International Ship and Offshore Structures Congress*, Nagasaki, Japan, pp. 253–321.

Ivanov, G. V. (1967). Approximating the final relationship between the forces and moments of shells under the mises plasticity condition (in Russian). *Inzhenernyi Zhurnal Mekhanika Tverdogo Tela 2*, 74–75.

Javaherian, H. and P. J. Dowling (1985). Large deflection elasto–plastic analysis of thin shells. *Engng. Structures 7*, 154–163.

Jeyachandrabose, C., J. Kirkhope, and C. R. Babu (1985). An alternative explicit formulation for the DKT plate–bending element. *Int. J. Numer. Meth. Engng. 21*, 1289–1293.

Kierkegaard, H. (1993). *Ship Collision with Icebergs*. Ph. D. thesis, Technical University of Denmark, Denmark.

Kirchhoff, G. (1850). Über das gleichgewicht und die Bewegung einer elastichen Scheibe. *J. Reine und Angewandte Mathematic 40*, 51–88.

Koiter, W. T. (1960). A consistent first approximation in the general theory of thin elastic shells. In W. T. Koiter (Ed.), *Proc. IUTAM Symposium on 'The theory of thin elastic shells'*, Amsterdam, North–Holland, pp. 12–33.

Koiter, W. T. (1966). On the nonlinear theory of elastic shells. In *Proc. Koninklijke Nederlandse Akademie van Wettenschappen*, pp. 1–54. Ser. B. No. 69.

Kröner, E. (1960). Allgemeine kontinuumstheorie der versetzungen und eigenspannungen. *Arch. Rat. Mech. Anal. 4*, 273–334.

Langhelle, N. and E. Eberg (1999). Ultimate strength testing of aluminum stressed skin structures at elevated temperatures. Report No. MT70 F99–398, Norwegian Marine Technology Research Institute, MARINTEK, SINTEF, Norway.

Lee, E. H. (1969). Elastic–plastic deformation at finite strains. *J. Appl. Mech. 36*, 1–6.

URN:NBN:no-1282

Lee, E. H. and D. T. Liu (1967). Finite strain elastic plastic theory particularly for plane waves. *J. Appl. Phys. 38*, 19–27.

Lemaitre, J. and J.-L. Chaboche (1990). *Mechanics of Solid Materials*. Cambridge: Cambridge University Press.

Lenselink, H. and K. G. Thung (1992). Numerical simulations of the Dutch–Japanese full scale ship collision tests. In *The conference on Prediction Methodology of Tanker Structural Failure*. Tokyo.

Levy, S. (1942). *Bending of rectangular plates with large deflections*. No. 846: NASA Technical Note.

Lubliner, J. (1990). *Theory of Plasticity*. New York: MacMillan.

Luenberger, D. G. (1969). *Optimization by vector space methods*. New York: John Wiley & Sons, Inc.

Malvern, L. E. (1969). *Introduction to the Mechanics of a Continuous Medium*, Volume Prentice–Hall series in engineering of the physical sciences. Englewood Cliffs, New Jersey: Prentice–Hall, Inc.

Marguerre, K. (1938). Zur theorie der gekrümmten platte grosser formänderung. In *Proc. Fifth Intern. Congr. Appl. Mech.*, New York, pp. 93. Wiley. (cited by Timoshenko 1959, Page 562).

MARPOL (1992). *Ammendments to MARPOL 73/78 on New Regulations 13F and 13G*. Resolution MEPC 52(32).

Matthies, H. G. (1989). A decomposition method for integration of elastic–plastic rate problem. *Int. J. Numer. Meth. Engng. 28*, 1–11.

Mattiasson, K. (1983). *On the co–rotational finite element formulation for large deformation problems*. Ph. D. thesis, Chalmers Tekniska Högskola, Göteborg.

Maugin, G. A. (1992). *The thermodynamics of plasticity and fracture*. Cambridge, Great Britain: Cambridge University Press.

Meek, J. L. and H. S. Tan (1986). Instability analysis of thin plates and arbitrary shells using a faceted shell element with loof nodes. *Comp. Meth. Appl. Mech. Engg. 57*, 143–170.

Mindlin, R. D. (1951). Influence of rotatory inertia and shear in flexural motions of isotropic elastic plates. *J. Appl. Mech. 18*, 31–38.

Mohammed, A. K., J. Amdahl, and B. Skallerud (2000a). A simple finite element model for geometrically nonlinear analyses of thin shells undergoing large rotations. Technical Report MK/R 145, Marine Structures Dept., Norwegian Univerisity of Science and Technology, NTNU, Norway.

Mohammed, A. K., J. Amdahl, and B. Skallerud (2000b). Stress–resultants plasticity on the morley element using a modified Ilyushin yield surface. In J. Hellesland, H. Osnes, and G. Skeie (Eds.), *Proc. Nordic Seminar on Computaional Mechanics (NSCM–13)*, Oslo, Norway, pp. 117–120.

URN:NBN:no-1282

Mohammed, A. K., J. Amdahl, and B. Skallerud (2001a). Collapse analysis of stiffened panels during accidental conditions. In *Proc. ASME Offshore Mechanics and Arctic Engineering (OMAE–2001)*, Rio de Janeiro, Brazil. CD–ROM.

Mohammed, A. K., J. Amdahl, and B. Skallerud (2001b). Elasto–plastic large displacement analysis of plate and shell structures using stress–resultants plasticity. In *Proc. European Conference on Computational Mechanics (ECCM–2001)*, Cracow, Poland. Datacomp. CD–ROM.

Mohammed, A. K., B. Skallerud, and J. Amdahl (2001). Simplified stress resultants plasticity on a geometrically nonlinear constant moment shell element. *Int. J. Compt. and Struct. 79*(18), 1723–1734.

Morley, L. S. D. (1971). The constant–moment plate–bending element. *J. Strain Anal. 6*(1), 20–24.

Morley, L. S. D. (1987). Practical components of vectors and tensors. *Int. J. Engng. Sci. 25*(1), 37–53.

Morley, L. S. D. (1991). Geometrically nonlinear constant moment triangle which passes the von Kármán patch test. *Int. J. Numer. Meth. Engng 31*, 241–263.

NSHEL (2000). *Nonlinear Analysis of shell structures* (3.01 ed.). Dept. of Marine Structures, Norway: NTNU. Programmed by A. K. Mohammed.

Nygård, M. K. (1986). *The free formulation for nonlinear finite elements with application to shells*. Ph. D. thesis, Division of Structural Mechanics, NTH, Trondheim, Norway.

Ohtsubo, H., T. Yao, and Y. Sumi (1999). Analysis of casualty of MS NAKHODKA. In *Proc. of OMAE–99*, St. Johns, Newfoundland, Canada.

Parlett, B. N. (1997). *The symmetric eigenvalue problem*. Philadelphia: SIAM.

Peng, X. and M. A. Crisfield (1992). A consistent co–rotational formulation for shells using the constant stress/constant moment triangle. *Int. J. Numer. Meth. Engng. 35*, 1829–1847.

Peric, D. and D. R. J. Owen (1991). The Morley thin shell finite element for large deformations problems: Simplicity versus sophistication. In *Proc. 4th Int. Conf. on Nonlin. Engrg. Comput. (NEC–91)*, pp. 121–142.

Providas, E. and M. A. Kattis (1999). A simple finite element model for the geometrically nonlinear analysis of thin shells. *Computaional Mechanics 24*, 127–137.

Providas, E. D. (1990). *On the geometrically nonlinear constant moment triangle (with a note on drilling rotations)*. Ph. D. thesis, Department of Mathematics and statistics, Brunel Univerisity, UK.

Ramm, E. (1982). The Riks/Wempner approach – An extension of the displacement control method in nonlinear analysis. In E. Hinton, D. R. J. Owen, and C. Taylor (Eds.), *Recent advances in nonlinear computational mechanics*. Swansea: Pineridge Press.

URN:NBN:no-1282

Reissner, E. (1945). The effect of transverse shear deformation on the bending of elastic plates. *J. Appl. Mech. 12*, 69–76.

Riks, E. (1972). The application of Newton's method to the problem of elastic stability. *J. Appl. Mech. 39*, 1060–1066.

Riks, E. (1979). An incremental approach to the solution of snapping and buckling problems. *Int. J. Solids Structures 15*, 529–551.

Ristinmaa, M. and N. S. Ottosen (1996). Large strain plasticity and thermodynamics. Technical report, Solid Mechanics, University of Lund, Lund, Sweden.

Roehl, D. and E. Ramm (1996). Large elasto–plastic finite element analysis of solids and shells with the enhanced assumed strain concept. *Int. J. Solids Structures 33* (20–22), 3215–3237.

Sabir, A. B. and A. C. Lock (1972). The application of finite elements to the large deflection geometrically nonlinear behaviour of cylindrical shells. In C. A. Brebbia and H. Tottenham (Eds.), *Variational methods in engineering*. Southampton: Southampton University Press.

Simo, J. C. and J. G. Kennedy (1992). On stress resultant geometrically exact shell model. Part V. Nonlinear plasticity: formulation and integration algorithms. *Comp. Methods Appl. Mech. Eng. 96*, 133–171.

Simo, J. C. and R. L. Taylor (1985). A return mapping algorithm for plane stress elastoplasticity. *Comp. Methods Appl. Mech. Eng. 48*, 101–118.

Simons, J., P. G. Bergan, and M. K. Nygård (1984). Hyperplane displacement control methods in nonlinear analysis. In W. K. Liu, T. Belytschko, and K. C. Park (Eds.), *Inovative Methods for Nonlinear Problems*, Swansea, pp. 345–364. Pineridge Press Ltd.

Simonsen, B. C. (2000). Personal homepage; Bo Cerup Simonsen's Research. Department of Naval Architecture and Offshore Engineering, Technical University of Denmark, DTU, Denmark. http://www.ish.dtu.dk/.

Skallerud, B. and B. Haugen (1999). Collapse of thin shell structures – stress resultant plasticity modelling within a co–rotated ANDES finite element formulation. *Int. J. Numer. Meth. Engng 46*, 1961–1986.

Skallerud, B., L. I. Myklebust, and B. Haugen (2001). Nonlinear response of shell structures: effects of plasticity modelling and large rotations. *Thin–Walled Structures 39*, 463–482.

Soares, C. G. and T. H. Søreide (1981). Behaviour and design of stiffened plates under predominantly compressive loads. In *CONGRESSO 81, Ordem dos Engenheiros*. Lisboa.

Søreide, T. H. (1981). *Ultimate load analysis of marine structures*. Trondheim, Norway: TAPIR.

Strang, G. (1972). Variational crimes in the finite element method. In A. K. Aziz (Ed.), *Proc. Symp. on the Mathematical Foundations of the Finite Element Method*

URN:NBN:no-1282

with Applications to Partial Differential Equations, New York, pp. 689–710. Baltimore, Academic Press.

Strang, G. and G. F. Fix (1973). *An Analysis of the Finite Element Method*. Englewood Cliffs, New Jersey: Prentice–Hall, Inc.

Stricklin, J. A., W. E. Haisler, P. R. Tisdale, and R. Gunderson (1969). A rapidly converging triangular plate element. *AIAA Journal 7*(1), 180–181.

Talbot, M. and G. Dhatt (1986). Three discrete Kirchhoff elements for shell analysis with large geometrical nonlinearities and bifurcations. *Eng. Comput. 4*, 15–22.

Timoshenko, S. P. and S. Woianowsky-Krieger (1959). *Theory of plates and shells* (2 ed.). Tokyo: McGraw–Hill Book Kogakusha Ltd. International Student Edition.

Tresca, H. E. (1872). Mémoire sur l'écoulement des corps solides. In *Mémoires Présentés par Divers Savants*, pp. 75–135. Acad. Sci. Paris, **20**. (cited by G. A. Maugin, 1992, page 17).

Truesdell, C. (1969). *Rational Thermodynamics*. McGraw Hill, Inc.

Turner, M. J., R. W. Clough, H. C. Martin, and L. J. Topp (1956). Stiffness and deflection analysis of complex structures. *J. Aeronaut. Sci. 23*, 805–824.

Urban, J., P. T. Pedersen, and B. C. Simonsen (1999). Collision risk analysis for HSC. In *FAST'99*, pp. 181–194.

USFOS (1998). *A computer program for pregressive collapse analysis of steel offshore structures*. NTNU, Norway: SINTEF. User's Manual.

van Keulen, F. (1993). A geometrically nonlinear curved shell element with constant stress resultants. *Comput. Methods Appl. Mech. Engrg. 106*, 315–352.

van Keulen, F. and J. Booij (1996). Refined consistent formulation of a curved triangular finite rotation shell element. *Int. J. Numer. Meth. Engng. 39*, 2803–2820.

von Kármán, T. (1910). Festigkeitsprobleme im maschinenbau. *Encyklopädie der Mathematischen Wissenschaften IV/4*(C), 311–385.

von Mises, R. (1913). Mechanik der festen körper im plastisch deformablen zustand. In *Gött. Nach. Math. -Phys. Kl.*, pp. 582–592. (cited by G. A. Maugin, 1992, page 18).

Wang, X. and T. Moan (1997, March). Ultimate strength analysis of stiffened panels in ships subjected to biaxial and lateral loading. *International Journal of Offshore and Polar Engineering 7*(1), 22–29.

Washizu, K. (1982). *Variational methods in elasticity and plasticity* (3 ed.). Oxford: Pergamon Press.

Wempner, G. (1969). Finite elements, finite rotations and small strains of flexible shells. *Int. J. Solids Struct. 6*, 117–153.

Wempner, G. A. (1971). Discrete approximations related to nonlinear theories of solids. *Int. J. solids Structures 7*, 1581–1599.

URN:NBN:no-1282

Yao, T. (1999, March). Ultimate longitudinal strength of ship hull girder: Historical review and state of the art. *Int. J. Offsh. Pol. Engrng. (ISOPE) 9*(1), 1–9.

Yao, T., M. Fujikubo, D. Yanagihara, and M. Irisawa (1998). Considerations on FEM modelling for for buckling/plastic collapse analysis of stiffened plates. *Transactions of the West–Japan Society of Naval Architects 95*, 121–128. (in Japanese).

Yao, T., M. Fujikubo, D. Yanagihara, and T. Murase (2001). Post–ultimate strength behaviour of long rectangular plate subjected to uni–axial thrust. In *Proc. Int. Offshore and Polar Engineering Conference*, Stavanger, Norway, pp. 390–397.

Zhong, H. G. and M. A. Crisfield (1998). An energy–conserving co–rotational procedure for the dynamics of shell structures. *Engineering Computations 15*(5), 552–576.

Zienkiewicz, O. C. and R. L. Taylor (2000a). *The Finite Element Method* (5 ed.), Volume 1. Oxford: Butterworth–Heinemann. The Basis.

Zienkiewicz, O. C. and R. L. Taylor (2000b). *The Finite Element Method* (5 ed.), Volume 2. Oxford: Butterworth–Heinemann. Solid Mechanics.

URN:NBN:no-1282

Previous Dr.Ing. Theses at the Department of Marine Structures

Kavlie, Dag	Optimization of Plane Elastic Grillages. (1967)
Hansen, Hans R.	Man–Machine Communication and Data–Storage Methods in Ship Structural Design. (1971)
Gisvold, Kaare M.	A Method for Non–Linear Mixed–Integer Programming and its Application to Design Problems.
Lund, Sverre	Tanker Frame Optimalization by Means of SUMT–Transformation and Behaviour Models. (1971)
Vinje, Tor	On Vibration of Spherical Shells Interacting with Fluid. (1972)
Lorentz, Jan D.	Tank Arrangement for Crude Oil Carriers in Accordance with the New Anti–Pollution Regulations. (1975)
Carlsen, Carl A.	Computer–Aided Design of Tanker Structures. (1975)
Larsen, Carl M.	Static and Dynamic Analysis of Offshore Pipelines during Installation. (1976)
Hatlestad, Brigt	The Finite Element Method Used in a Fatigue Evaluation of Fixed Offshore Platforms. (1979)
Valsgård, Sverre	Finite Difference and Finite Element Method Applied to Non–Linear Analysis of Plated Structures. (1979)
Pettersen, Erik	Analysis and Design of Cellular Structures. (1979)
Nordsve, Nils T.	Finite Element Collapse Analysis of structural Members

URN:NBN:no-1282

	Considering Imperfections and Stresses due to Fabrication. (1980)
Fylling, Ivar J.	Analysis of Towline Forces in Ocean towing Systems. (1980)
Haver, Sverre	Analysis of Uncertainties Related to the Stochastic Modelling of Ocean Waves. (1980)
Odland, Jonas	On the Strength of Welded Ring Stiffened Cylindrical Shells Primarily Subjected to Axial Compression. (1981)
Engesvik, Knut	Analysis of Uncertainties in the Fatigue Capacity of Welded Joints. (1982)
Eide, Oddvar Inge	On Cumulative Fatigue Damage in Steel Welded Joints. (1983)
Mo, Olav	Stochastic Time Domain Analysis of Slender Offshore Structures. (1983)
Amdahl, Jørgen	Energy Absorption in Ship–Platform Impacts. (1983)
Czujko, Jerzy	Collapse Analysis of Plates subjected to Biaxial Compression and Lateral Load. (1983)
Soares, C. Guedes	Probabilistic Models for Load Effects in Ship Structures. (1984)
Mørch, Morten	Motions and Mooring Forces of Semi Submersibles as Determined by Full–Scale Measurements and Theoretical Analysis. (1984)
Engseth, Alf G.	Finite Element Collapse Analysis of Tubular Steel Offshore Structures. (1985)
Baadshaug, Ola	Systems Reliability Analysis of Jacket Platforms. (1985) (Confidential)
Hessen, Gunnar	Fracture Mechanics Analysis of Stiffened Tubular Members. (1986)
Taby, Jon	Ultimate and Post–Ultimate Strength of Dented Tubular Members. (1986)

URN:NBN:no-1282

Wessel, Heinz–J.	Fracture Mechanics Analysis of Crack Growth in Plate Girders. (1986)
Leira, Bernt Johan	Gaussian Vector–Processes for Reliability Analysis Involving Wave–Induced Load Effects. (1987)
Xu Jun	Non–Linear Dynamic Analysis of Space–framed Offshore Structures. (1988)
Guoyang Jiao	Reliability Analysis of Crack Growth under Random Loading Considering Model Updating. (1989)
Olufsen, Arnt	Uncertainty and Reliability Analysis of Fixed Offshore Structures. (1989)
Wu Yu–Lin	System Reliability Analyses of Offshore Structures Using Improved Truss and Beam Models. (1989)
Farnes, Knut–Aril	Long–Term Statistics of Response in Non–Linear Marine Structures. (1990)
Sotberg, Torbjørn	Application of Reliability Methods for Safety Assessment of Submarine Pipelines. (1990)
Hoen, Christopher	System Identification of Structures Excited by Stochastic Load Processes. (1991)
Sødahl, Nils	Methods for Design and Analysis of Flexible Risers. (1991)
Haugen, Stein	Probabilistic Evaluation of Frequency of Collision between Ships and Offshore Platforms. (1991)
Ormberg, Harald	Non–Linear Response Analysis of Floating Fish Farm Systems. (1991)
Marley, Mark J.	Time Variant Reliability under Fatigue Degradation. (1991)
Bessason, Bjarni	Assessment of Earthquake Loading and Response of Seismically Isolated Bridges. (1992)
Sævik, Svein	On Stresses and Fatigue in Flexible Pipes. (1992)

URN:NBN:no-1282

Dalane, Jan Inge	System Reliability in Design and Maintenance of Fixed Offshore Structures. (1993)
Karunakaran, Daniel	Nonlinear Dynamic Response and Reliability Analysis of Drag–Dominated Offshore Platforms. (1993)
Passano, Elizabeth	Efficient Analysis of Nonlinear Slender Marine Structures. (1994)
Bech, Sidsel M.	Experimental and Numerical Determination of Stiffness and Strength of GRP/PVC Sandwich Structures. (1994)
Hovde, Geir Olav	Fatigue and Overload Reliability of Offshore Structural Systems, Considering the Effect of Inspection and Repair. (1995)
Wang, Xiaozhi	Reliability Analysis of Production Ships with Emphasis on Load Combination and Ultimate Strength. (1995)
Hellan, Øyvind	Nonlinear Pushover and Cyclic Analyses in Ultimate Limit State Design and Reassessment of Tubular Steel Offshore Structures. (1995)
Hermundstad, Ole A.	Theoretical and Experimental Hydroelastic Analysis of High Speed Vessels. (1995)
Eknes, Monika Løland	Escalation Scenarios Initiated by Gas Explosions on Offshore Installations. (1996)
Halse, Karl Henning	On Vortex Shedding and Prediction of Vortex–Induced Vibrations of Circular Cylinders. (1997)
Igland, Ragnar Torvanger	Reliability Analysis of Pipelines during Laying, Considering Ultimate Strength under Combined Loads. (1997)
Vikestad, Kyrre	Multi–Frequency Response of a Cylinder Subjected to Vortex Shedding and Support Motions. (1998)
Azadi, Mohammad R.E.	Analysis of Static and Dynamic Pile–Soil–Jacked Behaviour. (1998)
Videiro, Paulo Mauricio	Reliability Based Design of Marine Structures. (1998)
Mainçon, Philippe	Fatigue Reliability of Long Welds Application to Titanium

URN:NBN:no-1282

	Risers. (1999)
Langhelle, Nina Kristin	Experimental Validation and Calibration of Nonlinear Finite Element Models for Use in Design of Aluminium Structures Exposed to Fire. (1999)
Berstad, Are Johan	Calculation of Fatigue Damage in Ship Structures. (1999)
Tveiten, Bård Wathne	Fatigue Assessment of Welded Aluminium Ship Details. (1999)
Sagli, Gro	Model Uncertainty and Simplified Estimates of Long Term Extremes of Hull Girder Loads in Ships. (2000)
Tronstad, Harald	Nonlinear hydroelastic analysis and design of cable net structures like fishing gear based on the finite element method. (2000)
Wang, Lihua	Probabilistic Analysis of Nonlinear Wave–induced Loads on Ships. (2001)
Kristensen, Odd H.H.	Ultimate Capacity of Aluminium Plates under Multiple Loads, Considering HAZ Properties. (2001)
Heggelund, Svein E.	Calculation of Global Design Loads and Load Effects in Large High Speed Catamarans. (2001)
Babalola, Olusegun T.	Fatigue Strength of Titanium Risers – Defect Sensitivity. (2001)

URN:NBN:no-1282